

# UC Berkeley

## UC Berkeley Electronic Theses and Dissertations

### Title

Solid-state NMR Investigations of Proton Conducting Membranes

### Permalink

<https://escholarship.org/uc/item/5gs9v9bf>

### Author

Dodd, Matthew Ryan

### Publication Date

2014

Peer reviewed|Thesis/dissertation

**Solid-state NMR Investigations of Proton Conducting Membranes**

by

Matthew Ryan Dodd

A dissertation submitted in partial satisfaction of the  
requirements for the degree of

Doctor of Philosophy

in

Chemical Engineering

in the

Graduate Division

of the

University of California, Berkeley

Committee in charge:

Professor Jeffrey A. Reimer, Chair

Professor David E. Wemmer

Professor Rachel A. Segalman

Fall 2014

# Solid-state NMR Investigations of Proton Conducting Membranes

Copyright 2014  
by  
Matthew Ryan Dodd

## Abstract

Solid-state NMR Investigations of Proton Conducting Membranes

by

Matthew Ryan Dodd

Doctor of Philosophy in Chemical Engineering

University of California, Berkeley

Professor Jeffrey A. Reimer, Chair

This thesis applies magnetic resonance techniques to novel and traditional proton conducting materials in order to gain a better understanding of the molecular aspects of their performance. An array of experiments and techniques are used. One material is a morphologically designed block copolymer/ionic liquid system. Simple 1-D variable temperature (VT)  $^1\text{H}$  magic angle spinning (MAS) NMR is used to catalogue the dynamic chemical shifts, which relates to the prevalence of hydrogen bonding. Relaxation data are used to measure the relative mobilities of conduction protons, and these data are related to polymer physics phenomena. The effect of morphology is investigated by comparing block copolymer results to a series of homopolymer analogues without defined morphological structures. The role of entropy in these systems is discussed as well as the effect of a non-symmetric ionic liquids.

NMR techniques were also applied to more traditional materials, namely perfluoro-sulfonic acid membranes modified with amphoteric imidazole compounds. The chemical environments of the imidazole as well as the dynamics of proton transfer are measured with Solid-state  $^1\text{H}$  NMR. The effect of imidazole concentration is also considered.  $^1\text{H}$  -  $^{13}\text{C}$  cross polarization (CP) MAS NMR is used to reveal the presence of both fast and slow moving imidazole in the membranes. Pulsed field gradient (PFG) NMR is used to quantify the diffusion of protons and methanol through the material.

The goal of replacing gaseous hydrogen with organic virtual carrier molecules as a proton source for proton exchange membranes (PEM) fuel cells is investigate by testing the effect of model organic liquids in contact with typical membrane materials. A suite of data, including  $^{19}\text{F}$  NMR relaxation data of the polymer backbone and sidechains, are used to explain bulk phenomena and membrane performance.

To my family, friends, labmates, classmates and Ashley. Thank you all.

# Contents

|   |           |
|---|-----------|
| <b>List of Figures</b>  | <b>v</b>  |
| <b>List of Tables</b>   | <b>ix</b> |
| <b>1 Introduction</b>   | <b>1</b>  |
| 1.1 Motivation . . . . .  | 1         |
| 1.2 Methodology: Nuclear Magnetic Resonance . . . . .   | 2         |
| 1.3 Objectives . . . . .  | 3         |
| <b>2 Solid-state <math>^1\text{H}</math> NMR Study of Block Copolymer/Ionic Liquid System</b> | <b>5</b>  |
| 2.1 Acknowledgment . . . . .  | 5         |
| 2.2 Introduction . . . . .  | 5         |
| 2.3 Theory . . . . .  | 7         |
| 2.4 Methods . . . . .   | 8         |
| 2.5 Results and Discussion . . . . .  | 8         |
| 2.5.1 Poly(styrene- <i>block</i> -2-vinyl-pyridine) . . . . .                                 | 9         |
| 2.5.2 S2VP/[Im][TFSI] . . . . .   | 9         |
| 2.5.3 [Im]/[TFSI] . . . . .   | 10        |
| 2.5.4 P2VP at low pH . . . . .  | 12        |
| 2.5.5 Variable Temperature NMR . . . . .  | 14        |
| 2.5.6 Effect of Confinement . . . . .   | 16        |
| 2.5.7 Non-symmetric [Im][TFSI] . . . . .  | 21        |
| 2.6 Conclusions . . . . .   | 21        |
| <b>3 Proton Mobility and Activation</b>   | <b>25</b> |
| 3.1 Acknowledgment . . . . .  | 25        |
| 3.2 Introduction . . . . .  | 25        |
| 3.3 Methods . . . . .   | 26        |
| 3.4 Results and Discussion . . . . .  | 26        |
| 3.4.1 Activation Energy and Local Proton Mobility . . . . .                                   | 26        |
| 3.4.2 Entropic Contributions . . . . .  | 30        |
| 3.4.3 Non-symmetric Ionic Liquids . . . . .   | 32        |

|          |   |           |
|----------|---|-----------|
| 3.4.4    | Spin-Lattice Relaxation . . . . .   | 36        |
| 3.5      | Conclusions . . . . .   | 40        |
| <b>4</b> | <b>Exchange and Diffusion in PFSA Membranes</b>                                       | <b>41</b> |
| 4.1      | Acknowledgement . . . . .   | 41        |
| 4.2      | Introduction . . . . .  | 41        |
| 4.3      | Methods . . . . .   | 42        |
| 4.4      | Results and Discussion . . . . .  | 42        |
| 4.4.1    | 3M EW825 . . . . .  | 43        |
| 4.4.1.1  | Full ImOH Incorporation . . . . .   | 44        |
| 4.4.1.2  | Half ImOH Incorporation . . . . .   | 50        |
| 4.4.1.3  | $^1\text{H}$ - $^{13}\text{C}$ CPMAS NMR . . . . .                                    | 52        |
| 4.5      | $^{19}\text{F}$ NMR . . . . .   | 57        |
| 4.6      | Self-Diffusion . . . . .  | 57        |
| 4.6.1    | Pulse Sequence . . . . .  | 58        |
| 4.6.2    | Experimental . . . . .  | 59        |
| 4.6.3    | Results . . . . .   | 61        |
| 4.7      | Conclusions . . . . .   | 63        |
| 4.8      | Supporting Information: Results of Spectrum Deconvolution . . . . .                   | 63        |
| <b>5</b> | <b>Interactions of PFSA Membranes and Organic Liquids</b>                             | <b>66</b> |
| 5.1      | Acknowledgement . . . . .   | 66        |
| 5.2      | Introduction . . . . .  | 66        |
| 5.3      | Methods . . . . .   | 67        |
| 5.4      | Results and Discussion . . . . .  | 67        |
| 5.4.1    | Bulk Membrane Measurements . . . . .  | 67        |
| 5.4.2    | SAXS . . . . .  | 70        |
| 5.4.3    | Solid-State NMR . . . . .   | 70        |
| 5.5      | Conclusions . . . . .   | 73        |
|          | <b>Bibliography</b>   | <b>76</b> |
| <b>A</b> | <b>Carbon Dioxide Capture in Amine Functionalized Metal Organic Frameworks (MOFs)</b> | <b>80</b> |
| A.1      | Methods . . . . .   | 80        |
| A.2      | Results and NMR Details . . . . .   | 81        |
| <b>B</b> | <b><math>^{15}\text{N}</math> NMR Studies of Imidazole-based Ionic Liquids</b>        | <b>84</b> |
| B.1      | Methods . . . . .   | 84        |
| B.2      | Results and Discussion . . . . .  | 85        |
| B.2.1    | $^{15}\text{N}$ Powder Spectra . . . . .  | 85        |
| B.2.2    | $^{15}\text{N}$ MAS NMR . . . . .   | 89        |

|   |   |     |
|---|---|-----|
| C | Single $T_2$ Spin Echo Fit: Example Mathematica Code          | 91  |
| D | Single $T_1$ Inversion Recovery Fit: Example Mathematica Code | 95  |
| E | PFGSE Single Self Diffusion Coefficient Fitting: MATLAB code  | 99  |
| F | $T_{1\rho}$ Relaxation Data Fitting: Mathematica Code         | 106 |



# List of Figures

|      |   |    |
|------|---|----|
| 2.1  | Chemical structures of poly(styrene- <i>block</i> -2-vinylpyridine) copolymer and imidazolium and TFSI ions. . . . .  | 6  |
| 2.2  | $^1\text{H}$ NMR spectrum of poly(styrene- <i>block</i> -2-vinylpyridine) at 20 kHz MAS and 150 °C . . . . .  | 9  |
| 2.3  | $^1\text{H}$ NMR spectrum of S2PV/[Im][TFSI] 61%wt polymer at 20 kHz MAS and 150 °C . . . . .   | 10 |
| 2.4  | $^1\text{H}$ NMR Spectra of [Im][TFSI] at 8 kHz MAS and 90 °C . . . . .   | 11 |
| 2.5  | Variable temperature $^1\text{H}$ NMR spectrum of 5:5 [Im][TFSI] at 8 kHz MAS. The temperatures are (bottom to top) 45 °C, 55 °C, 65 °C, 75 °C, 85 °C and 90 °C. . . . .  | 13 |
| 2.6  | S2VP with HCl at 20 kHz MAS and 150 °C . . . . .  | 14 |
| 2.7  | Variable Temperature $^1\text{H}$ NMR of S2PV/[Im][TFSI] 61%wt polymer at 20 kHz MAS. The temperatures are (bottom to top) 45 °C, 60 °C, 75 °C, 90 °C, 105 °C, 120 °C, 135 °C and 150 °C. . . . .   | 15 |
| 2.8  | Mobile proton chemical shifts as a function of temperature for S2VP/[Im][TFSI] . . . . .  | 17 |
| 2.9  | $^1\text{H}$ NMR spectrum of P2VP/[Im][TFSI] at 20 kHz MAS and 150 °C . . . .   | 18 |
| 2.10 | Mobile $^1\text{H}$ chemical shift as a function of temperature for P2VP/[Im][TFSI]   | 19 |
| 2.11 | Comparison of P2VP/[Im][TFSI] and S2VP/[Im][TFSI] mixtures. The homopolymers appear as circles, and the block copolymers are squares. . . .   | 20 |
| 2.12 | $^1\text{H}$ NMR of S2PV/[Im][TFSI] 70%wt polymer at 20 kHz MAS and 150 °C with 8:2 ionic liquid . . . . .  | 22 |
| 2.13 | Comparison of mobile proton chemical shifts for S2VP/[Im][TFSI] with different ionic liquids symmetries . . . . .   | 23 |
| 3.1  | Temperature-dependent transverse relaxation of mobile $^1\text{H}$ resonance for S2VP/[Im][TFSI] 61%wt. polymer . . . . .   | 27 |
| 3.2  | Temperature-dependent transverse relaxation of mobile $^1\text{H}$ resonance for S2VP/[Im][TFSI] samples. The red sphere is located at the $T_g$ of the respective P2VP phase and placed along the line of best fit of the Arrhenius fit. . . . . | 28 |

|      |   |    |
|------|---|----|
| 3.3  | Arrhenius activation energies of S2VP/[Im][TSFI]. Error generated from multiple experiments. . . . .  | 28 |
| 3.4  | Temperature-dependent transverse relaxation of mobile $^1\text{H}$ resonance for P2VP/[Im][TFSI] samples. The red sphere is the $T_g$ of the respective P2VP phase placed along the line of best fit of the Arrhenius fit. . . . .  | 29 |
| 3.5  | Arrhenius activation energies of P2VP/[Im][TSFI]. Error generated from multiple experiments. . . . .  | 30 |
| 3.6  | Eyring plot for mobile $^1\text{H}$ resonance for S2VP/[Im][TSFI] 61%wt. polymer  | 31 |
| 3.7  | Eyring plots for S2VP/[Im][TSFI]. The data used are from Figure 3.2. . . .  | 33 |
| 3.8  | Eyring plots for P2VP/[Im][TSFI]. The data used are from Figure 3.4 . . .   | 34 |
| 3.9  | Temperature-dependent transverse relaxation of mobile $^1\text{H}$ resonance for P2VP/[Im][TFSI] with 8:2 ionic liquid . . . . .  | 35 |
| 3.10 | Extrapolated activation energy fit to $1/T = 0$ for S2VP/[Im][TSFI] with asymmetric ionic liquid included . . . . .   | 35 |
| 3.11 | Average $^1\text{H}$ $T_1$ times of S2VP/[Im][TSFI] vs. temperature . . . . .   | 37 |
| 3.12 | Average $^1\text{H}$ $T_1$ times of P2VP/[Im][TSFI] vs. temperature . . . . .   | 37 |
| 3.13 | Site specific $^1\text{H}$ $T_1$ times comparing 5:5 and 8:2 systems with similar ionic liquid loadings . . . . .   | 38 |
| 3.14 | Activation energies derived from spin-lattice relaxation times for two proton types . . . . .   | 39 |
| 4.1  | $^1\text{H}$ MAS NMR spectrum of Nafion equilibrated at 50 °C and 25% RH. The MAS rate is 1.7 kHz which produces small spinning sidebands around 0 and 12 ppm. . . . .  | 43 |
| 4.2  | Chemical structure of 3M material . . . . .   | 43 |
| 4.3  | Chemical structure of 4(5)-(hydroxymethyl)imidazole . . . . .   | 44 |
| 4.4  | Variable temperature $^1\text{H}$ MAS NMR of 3M 825 with 100% 4(5)-(hydroxymethyl)imidazole saturation. MAS rate is 15 kHz. . . . .   | 45 |
| 4.5  | Peak deconvolution of $^1\text{H}$ MAS NMR of 3M 825 with 100% 4(5)-(hydroxymethyl)imidazole saturation at each temperature. MAS rate is 15 kHz. The red line is the sum of the exchanging protons. The blue peak is the sum of the the covalently bound C-H proton on imidazole. The dotted black line is the sum of the blue and red line. Note the expanded ppm scale for the -45 °C spectrum. . . . . | 46 |
| 4.6  | $^1\text{H}$ chemical shift of downfield, exchangeable proton vs. temperature . . . .   | 48 |
| 4.7  | Temperature-dependent transverse relaxation time of exchanging proton . .   | 48 |
| 4.8  | Dynamic vapor sorption of 3M 825 EW membranes with ImOH at 50 °C. <i>Data courtesy of Kyle Clark.</i> . . . . .   | 49 |
| 4.9  | Conductivity vs. relative humidity of 3M 825 EW membranes with ImOH at 80 °C. <i>Data courtesy of Kyle Clark.</i> . . . . .   | 50 |

|      |  |    |
|------|--|----|
| 4.10 | Variable temperature $^1\text{H}$ MAS NMR of 3M 825 with 50% 4(5)-(hydroxymethyl)imidazole saturation. MAS rate is 15 kHz. The membrane was stored in laboratory conditions (i.e. ambient humidity).       | 51 |
| 4.11 | Temperature-dependent transverse relaxation time of fast exchanging protons  | 52 |
| 4.12 | $^{13}\text{C}$ CP/MAS spectrum of 4(5)-(hydroxymethyl)imidazole   | 53 |
| 4.13 | $^{13}\text{C}$ CP/MAS spectrum of 3M EW825 with 100% ImOH addition. The contact time is 1 millisecond.  | 54 |
| 4.14 | $^{13}\text{C}$ CP/MAS spectrum of 3M EW825 with 50% ImOH addition. The contact time was 1 millisecond.  | 54 |
| 4.15 | $^{13}\text{C}$ direct detection spectrum of 3M EW825 with 100% ImOH addition  | 55 |
| 4.16 | Spectrally edited $^{13}\text{C}$ direct detection spectrum of 3M EW825 with 100% ImOH addition. The broad polymer peak has been eliminated.   | 56 |
| 4.17 | $^{19}\text{F}$ NMR of dispersions of 3M EW850 in MeOH   | 58 |
| 4.18 | The Stejskal and Tanner pulsed-field gradient NMR sequence   | 59 |
| 4.19 | Field gradient strength calibration of water at 30°C. The intensities are normalized to the first echo and then fit to the Stejskal and Tanner equation. The gradient at full strength is 2.4 Tesla/meter. | 60 |
| 4.20 | Comparison of proton diffusion in standard Nafion and modified Nafion. The majority of the signal is from water protons in the solution.   | 61 |
| 4.21 | Comparison of MeOH diffusion in standard Nafion and modified Nafion  | 62 |
| 4.22 | Ratio of proton to methanol diffusion vs. temperature  | 63 |
| 5.1  | Model organic fuels tested for membrane interactions   | 67 |
| 5.2  | Vapor sorption isotherms for untreated and fuel treated N212 membranes at 50 °C vs. relative humidity. <i>Data courtesy Kyle Clark and Lakshmi Krishnan.</i>   | 68 |
| 5.3  | Proton conductivity vs. RH at 75 50 °C for untreated and treated membranes. <i>Data courtesy Kyle Clark and Lakshmi Krishnan.</i>  | 69 |
| 5.4  | SAXS profiles of untreated and decalin treated membranes at 50 °C with increasing RH. The humidities are 25%, 35%, 50%, 75%, 85%, and 95%.   | 71 |
| 5.5  | Pulse sequence for $T_{1\rho}$ measurement   | 72 |
| 5.6  | $T_{1\rho}$ for main-chain and side-chain fluorine in untreated and decalin treated N212 membranes as a function of spinlock frequency   | 72 |
| 5.7  | $T_{1\rho}$ for terminal fluorine group in untreated and decalin treated N212 membranes as a function of spinlock frequency  | 73 |
| 5.8  | $^1\text{H}$ MAS spectrum of decalin treated Nafion at 76 MHz. This spectrum is taken from an inversion recovery sequence taken with 30 ms delay after the $\pi$ pulse.                                    | 74 |
| 5.9  | Interpretation of morphological changes to Nafion when treated with decalin. <i>Illustration courtesy of Gary Yeager</i>   | 75 |

|     |  |    |
|-----|--|----|
| A.1 | $^{13}\text{C}$ CP/MAS spectra of a) IRMOF-74-III- $\text{NH}_2$ , b) $-\text{CH}_2\text{NHMe}$ , c) $-\text{CH}_2\text{NH}_2$ and d) $-\text{CH}_2\text{NHBoc}$ treated with $^{13}\text{C}$ -labeled carbon dioxide and recorded at 25 °C. The vertical lines are at 160 and 164 ppm. The general broadness of the spectrum derives from an offset in the magic angle. . . . . | 82 |
| A.2 | $^{13}\text{C}$ CP/MAS spectra after initial $\text{CO}_2$ loading (blue) and after heating over flowing $\text{N}_2$ (red) . . . . .  | 83 |
| B.1 | $^{15}\text{N}$ powder spectrum of crystallized imidazole at room temperature. 2084 scans were acquired using an 80 second recycle delay. . . . .  | 85 |
| B.2 | $^{15}\text{N}$ CP/MAS spectrum of imidazole crystals at room temperature at 12 kHz MAS. 16 scans were used with an 80 second recycle delay. . . . .   | 86 |
| B.3 | Simulated powder patterns and $^{15}\text{N}$ NMR data . . . . .   | 87 |
| B.4 | $^{15}\text{N}$ powder patterns for 5:5 ionic liquid in P2VP vs. temperature. The weight fraction of polymer is 38%. . . . .   | 88 |
| B.5 | $^{15}\text{N}$ powder patterns for 5:5 ionic liquid in P2VP vs. concentration . . . .   | 89 |
| B.6 | $^{15}\text{N}$ and $^1\text{H}$ chemical shifts for imidazole nitrogens and mobile protons for [Im][TSFI] in P2VP. These data are take at different temperatures over the range 150 °C to 90 °C. The increasing proton shifts correspond to higher temperatures. . . . .  | 90 |

# List of Tables

|     |   |    |
|-----|---|----|
| 2.1 | Summary of proton chemical shifts for imidazolium in neat ionic liquid and 61%wt polymer . . . . .                    | 12 |
| 2.2 | List of S2VP/[Im][TSFI] samples . . . . .   | 16 |
| 2.3 | Summary of proton chemical shifts for imidazole in similar polymer mixtures and neat ionic liquid at 150 °C . . . . . | 21 |
| 4.1 | List of carbon chemical shifts (ppm) for ImOH . . . . .   | 55 |
| 4.2 | Summary of fitting parameters for peaks in 3M 825 EW with 100% ImOH substitution at 15 kHz MAS and -45 °C. . . . .    | 64 |
| 4.3 | Summary of fitting parameters for peaks in 3M 825 EW with 100% ImOH substitution at 15 kHz MAS and 35 °C. . . . .     | 64 |
| 4.4 | Summary of fitting parameters for peaks in 3M 825 EW with 100% ImOH substitution at 15 kHz MAS and 45 °C. . . . .     | 64 |
| 4.5 | Summary of fitting parameters for peaks in 3M 825 EW with 100% ImOH substitution at 15 kHz MAS and 60 °C. . . . .     | 64 |
| 4.6 | Summary of fitting parameters for peaks in 3M 825 EW with 100% ImOH substitution at 15 kHz MAS and 75 °C. . . . .     | 65 |
| 4.7 | Summary of fitting parameters for peaks in 3M 825 EW with 100% ImOH substitution at 15 kHz MAS and 90 °C. . . . .     | 65 |

## Acknowledgments

This material is based upon work supported as part of the Center for Electrocatalysis, Transport Phenomena, and Materials (CETM) for Innovative Energy Storage, an Energy Frontier Research Center funded by the U.S. Department of Energy, Office of Science, Office of Basic Energy Sciences under Award Number DE-SC0001055.

The author would also like to thank the following:

Jeff Reimer, for his support and guidance

UC Berkeley, for an such an education

John Kerr and the Kerr group, especially Kyle Clark, for their help and knowledge

Dr. Sean Kong and Dr. Jian Feng, for their expertise

Undergraduate Jay Yostanto, for all his help

Dr. Megan Hoarfrost, for providing samples and teaching synthetic techniques

The entire Reimer lab past and present, especially Eric Scott, Joe Chen, Velencia Witherspoon, Melanie Drake, Carly Anderson, Joel Stettler, Jonathan King, and Brian Mayer  
ChemE Class 2008, for great friendships

My softball teammates, for such great fun

The college of chemistry staff, for all their help

Dr. Ashely Fritz, for everything

# Chapter 1

## Introduction

### 1.1 Motivation

The ever growing push towards a sustainable energy future naturally leads to interest in fuel cell technologies. Polymer electrolyte membrane fuel cells (PEMFC) are particularly attractive in the realm of clean portable energy and are thus potentially viable to automobile applications[1]. However, currently available materials are not suitable in maintaining desired operating conditions. For example, a traditional membrane is a hydrated perfluorosulfonic acid (PFSA) polymer which forms a two phase matrix through which water and protons shuttle to the cathode in the ionic phase. To maintain a reasonable proton flux, the membrane must remain hydrated. The hydration level is naturally diminished when running the cell above the boiling point of water. However, reducing the temperature instigates the problem of parasitic carbon monoxide poisoning the expensive platinum or platinum alloy catalysts[2].

The key point of this work is to study new materials that can push the boundaries of traditional membrane materials. Greater flexibility is needed to open the door to different fuel sources such as gaseous hydrogen or even proton-rich organics such as methanol. Previous studies have already started looking at ways to increase the operating temperature while maintaining proton conductivity. Increasingly popular ideas include inorganic fillers[3], doping with acids[4], or even replacing water with different proton carriers[5]. This lattermost method often makes use of amphoteric nitrogen based heterocycles to act as both proton accepters and donors. In a similar manner, room temperature ionic liquids (RTILs) are drawing increasing attention as proton conductors due to their unique physicochemical properties such as high thermal stability, negligible vapor pressure, and high ionic conductivity[6].

A final approach attempts to build an ideal proton-conducting membrane from the ground up using self-assembled block copolymers which can be carefully tuned to control morphology and domain sizes[7]. This level of control allows ionic domains which facilitate charge transport to be regularly patterned with nonionic domains which provide mechanical support. These membranes have a distinct advantage in the control of the

geometric layout of the desired domains on many length scales, whereas typical perfluorosulfonic polymers are more random in their assembly. It is believed that careful design can lead to a whole family of materials with each member specifically optimized for the exact performance required.

## 1.2 Methodology: Nuclear Magnetic Resonance

Traditional fuel cell measurements often use bulk measurements to assess the performance of the cell. However, understanding the myriad factors whose interactions sum to the overall performance is impossible. Nuclear magnetic resonance shrinks the scope of the view to the microscopic level while still providing a bulk average perspective on molecular events.

NMR provides both structural and dynamic information. The relative frequencies that nuclei experience are fingerprints of their chemical environment while the stochastic phenomena that relax coherent signals can discern motion. When molecules move between different chemical environments, NMR catches a snapshot of this motion with quantitative results. Whereas electrons are constantly crashing and zipping about, the nucleus sits in the eye of the storm, less affected and interested by that going on around it, but with much to tell.

### 1.2.1 Structural Studies

The ubiquitous nature of  $^1\text{H}$  atoms in many soft materials makes  $^1\text{H}$  NMR a viable technique. Even in perfluorosulfonic polymer membranes, which contain a backbone and sidechain completely substituted with fluorine, the absorbed ambient water provides strong NMR signals. The reason for this is an inherently high magnetogyric ratio and large natural abundance. Sensitivity is often an issue in NMR experiments, many of which can take weeks or even months to acquire enough signal. Protons manage to sidestep this concern rather easily.  $^1\text{H}$  NMR is also advantageous because it directly probes the conducting species of interest.

Protons lack the chemical shift sensitivity of other common nuclei such as  $^{13}\text{C}$  and  $^{15}\text{N}$ ; the simpler bonding nature and lack of electrons generate less range in electronic environments. The chemical shift information is very powerful nonetheless. How proton carriers donate and accept protons is very important to the energetics of proton transport. Protons which find themselves straddled between two carriers experience hydrogen bonding that reduces their electron density. These protons will shift downfield because the counteracting electron shielding is reduced. In general, protons forming new hydrogen bonds will see their  $^1\text{H}$  resonances shift downfield because some electron density is being distributed towards a new, more electronegative atom or molecule. When this bond breaks, the shift will move back upfield. The relative shifts offer conclusive evidence of how the mobile protons are distributed.



The large magnetogyric ratio of  $^1\text{H}$  has devastating effects on the resolution of  $^1\text{H}$  solid state NMR spectra. This is due to anisotropic dipolar couplings which cause homogeneous broadening. A common way to reduce this effect is macroscopic sample rotation. Magic angle spinning (MAS) NMR is a powerful tool to help average out anisotropic interactions. In most polymer systems, however, the spinning speeds available in the Reimer lab are insufficient to fully average dipolar couplings, but chemical shift anisotropies are removed.

### 1.2.2 Dynamics

The manner in which NMR signals relax back to equilibrium provides insight into relative motions. For polymers, the kHz timescale dominates the motional modes[8]. Therefore, relaxation differences sensitive to these times scales are indicative of even small changes in polymer dynamics. In the case of perfluorosulfonic polymer membranes, the polymer motion dictates the mechanical properties. While ions provide conductivity, the polymer must be mobile enough to facilitate ionic channel formation. On a molecular level, self-diffusion, the translational movement of molecules via Brownian motion, is a fundamental measure of the mobility of a chemical moiety. Field gradient NMR is an established technique which measures self-diffusion on different length and time scales.

## 1.3 Objectives

The work herein focuses on providing molecular-level understanding to broader research programs which seek to design, synthesize, and characterize new membranes and proton conducting fuel cells. This work benefits from the synthetic capabilities of other researchers as well as bulk measurements not related to NMR. These results are combined in a multidisciplinary manner to reach conclusions. In general, the NMR insights concern several topics:

- How do protons move?
  - Proton conduction is usually governed by two mechanisms. The vehicle mechanism relies on the diffusion of whole molecules carrying protons. This might include cations of various forms such as hydronium ions and protonated ionic liquids. The second mechanism is known as structural diffusion or the Grotthus mechanism. This method does not require the diffusion of whole proton carriers, but rather involves protons passing between separate carriers and then solvent molecules reorienting as protons are passed down the line. Such mechanisms have been predicted in imidazole systems[9].  $^1\text{H}$  NMR can be used to quantify the chemical environments and also show exchange between them.
- How mobile are the protons?

- Conductivity is a measure of the ease with which protons move through the materials. Obviously, some covalently bound protons, which show up in the NMR spectra are unrelated to the flux. The protons of interest are mobile in the sense that they are free to diffuse through the material or form new bonds and are released from old ones in a structural diffusion scheme. Spectroscopic resolution of the mobile protons is highly desirable to assess their mobility (lineshape) and chemical environments. However, if the various protons are not resolvable in spectrum, differentiating protons based on their relaxation rates is a common technique. Additionally, variable temperature NMR is a popular tool to increase resolution by reducing anisotropic couplings and also measure proton activation energies. However, this mobility is local in nature, meaning line narrowing processes relate to proton motions relative to nearby protons. This usually offers information on the short range order, but long range order is often dependent on other factors such as phase morphologies and grain boundaries. Long range conductivity is accessible with bulk measurements such as AC impedance techniques. The comparison of bulk measurements and NMR data highlights the difference between long range and local conduction. Lastly, field gradient NMR provides a non-invasive means to compare the relative mobilities of the various moieties. This method will prove valuable when measuring the relative diffusivity of protons and methanol in membranes.
- What about the polymer?
  - The move towards new fuels introduces issues concerning the behavior of the membrane in contact with liquids other than water. Generally, water imbibes itself into an ionomer due to its polar nature. However, switching to an organic proton source will change the mechanical properties of the membrane due to solvent interaction with the hydrophobic moieties in the polymer membrane. While the chemical structure of the polymer might remain intact, the dynamic nature will surely be altered after solvent penetration. Relaxometry will be used to understand the nature of organic/polymer interactions and how they affect performance.

This work seeks to apply nuclear magnetic resonance techniques to traditional and new systems in efforts to answer these questions in molecular detail.

## Chapter 2

# Solid-state $^1\text{H}$ NMR Study of Block Copolymer/Ionic Liquid System

### 2.1 Acknowledgment

The author gratefully acknowledges the contribution of Dr. Megan Hoarfrost, a former graduate student in the group of Rachel Segalman in the Department of Chemical and Biomolecular Engineering at UC Berkeley.

### 2.2 Introduction

Polymer scientists have already demonstrated the self-assembled phase behavior of block copolymers comprising poly(styrene-*block*-2-vinyl pyridine) (S2VP) when the ionic liquid solvent imidazolium bis(trifluoromethane)sulfonimide ([Im][TFSI]) is introduced in certain concentration ranges[10]. Figure 2.1 shows the chemical structures of the ionic liquid and polymer. When the ionic liquid is mixed with the diblock copolymer, the ionic liquid partitions itself almost completely into the vinyl pyridine (P2VP) phase. At very low ionic liquid concentrations, this combination has the effect of raising the glass transition temperature ( $T_g$ ) slightly due to a physical salt-like cross-linking effect[11]. However, at higher concentrations, the ionic liquid behaves more like a plasticizer and significantly lowers  $T_g$ . Because the styrene phase is resistant to solvent uptake, its  $T_g$  remains unchanged with [Im][TFSI] addition, thus providing an anchor of mechanical strength as the P2VP phase becomes less rigid. The native  $T_g$  of both the pure PS and P2VP block is around 100 °C.

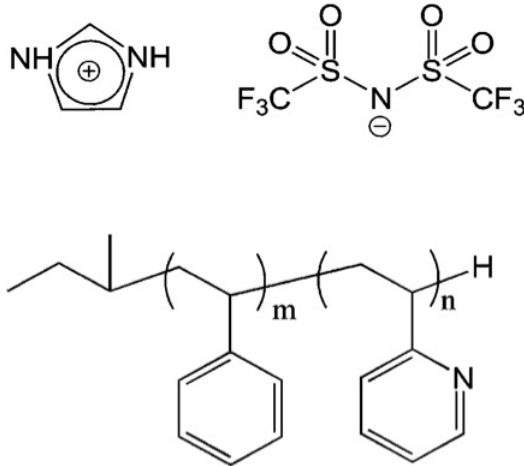


Figure 2.1: Chemical structures of poly(styrene-*block*-2-vinylpyridine) copolymer and imidazolium and TFSI ions.

The pervasive tendency of [Im][TFSI] to partition into the P2VP phase is not unexpected. Pyridine is a weak base that can complex with H<sup>+</sup>, providing a means to create proton defects and promote Grotthuss type proton conduction. Styrene is much less polar and has little thermodynamic incentive to mix with ions. The plasticization of the P2VP phase is also an advantage in ion conduction as shown by the famous empirical Vogel-Tamman-Fulcher (VTF) equation which expresses ionic conduction,  $\sigma$ , as

$$\sigma = A * \exp\left(\frac{-B}{R(T - T_o)}\right)$$

where A is a fitting parameter that scales with concentration, B is similar to an activation energy and is related to the segmental motion of the polymer and T<sub>o</sub> is related to the T<sub>g</sub> of the polymer. Generally, T<sub>o</sub> is found to be -50 K below the glass transition temperature. Therefore, lowering T<sub>g</sub> will increase conduction. Along similar lines, conduction is proportional to the number of ion carriers and increasing ion concentration further plasticizes the polymer. This double effect encourages adding a large amount of ionic liquid to achieve higher conductivities. In addition, it has been shown that ionic phase conductivity can be simply scaled directly to the overall volume fraction of ionic liquid of which T<sub>g</sub> is a function[12].

Traditional polymer studies focus on the overall conductivity of membranes either through-plane or in-plane using AC impedance spectroscopy. Solid-state NMR measurements provide local dynamics and activation energies. Often bulk conductivity measurements and those predicted by NMR are incongruent with NMR conductivity being higher. Often the reason for this is that NMR deals with local proton dynamics while ignoring tortuosity effects and grain boundaries. When the data are compared directly, one can answer the questions of whether conduction is hampered on a local scale or in a long

range manner. This study uses  $^1\text{H}$  NMR to look directly at the conduction protons and measure their local mobility.

NMR provides pictures of the chemical environments present. The timescales of these pictures vary greatly depending on the magnitude of the magnetic field and chemical shift range in question. As will be seen, the chemical shift of the mobile imidazolium proton is shifted downfield in the presence of the proton accepting pyridine moieties in the polymer. What chemical structure corresponds to that shift? The answer is no permanent physical state. Imidazole, especially in solids, has the ability to form hydrogen bonds readily[13]. Its neutral pKa range leads to amphoteric behavior that can accept or donate protons. The rate of making and breaking these proton hydrogen bonds between molecules will depend very heavily on temperature, as do most equilibrium processes. In certain regimes, the bonds will fluctuate so fast that NMR can record only the average NMR observable, such as chemical shift. Lowering the temperature or raising the field could possibly help ameliorate this problem, yet for this system, decreasing the temperature robs the spectrum of resolution required to separate all the information. Nevertheless, the average proton environment measured above room temperature remains useful in assessing cooperative hydrogen bonding and dynamics. The question remains which factors under our control play a major role in creating a Grotthuss mechanism based proton conductor. By using variable temperature NMR, the chemical shift acts as a thermometer, not for the thermal energy, but for the nature of the hydrogen-bonding interactions.

## 2.3 Theory

The fluctuation of the chemical environments in the fast exchange limit will lead to a single resonance that represents a population weighted linear combination of the contributing states. The apparent frequency can be calculated with

$$v_{avg} = \sum n_i v_i$$

where  $n_i$  is the mole fraction of a specific chemical environment and  $v_i$  is the frequency of that chemical environment. Of course

$$\sum n_i = 1$$

must be true to account for all exchanging protons. Near the fast exchange limit, line narrowing as a function of temperature is correlated with the exchange rate. In this regime

$$\Omega^2 \gg \Delta^2$$

where  $\Omega$  is the the exchange rate and  $\Delta$  is the frequency difference between the sites. This limit occurs when the correlation time of the motion  $\tau_c$  is less than  $10^{-7}$ seconds. When the fast exchange limit is reached, the observed linewidth is proportional to  $\frac{2}{T_2^*} + \frac{\Delta^2}{\Omega}$ [14],

where

$$\frac{1}{T_2^*} = \frac{1}{T_2} + \frac{1}{T_{inhomogeneous}}.$$

Here  $T_2$  is the natural, homogeneous characteristic relaxation time and  $T_{inhomogeneous}$  is that due to the instrument specific inhomogeneous magnetic field over the sample. As the rate increases, the linewidth eventually is no longer a function of the exchange rate.

## 2.4 Methods

Samples of S2VP were synthesized in the Segalman lab as described in Yokoyama et al. [15]. The block copolymer comprised a fixed polystyrene volume fraction  $f_{ps}=0.62$ . The molecular weight of the of the PS block was 18.3 kg/mol with a total copolymer molecular weight of 29.8 kg/mol. The total volume fraction of ionic liquid in the mixtures  $\psi_{[IM][TSFI]}$  varied from 0.29 down to 0. The volume fraction is estimated by assuming ideal mixing and using the densities of neat ionic liquid and polymer. The polymer morphology under these volume fractions of [Im][TSFI] corresponds to lamellae[10].

Samples were prepared in an argon glove box. Ionic liquid was added to the polymer by mixing proper amounts of the two in a vial and then dissolving them together in tetrahydrofuran overnight. The solution was cast one drop at a time onto a sample holder and then heated overnight above the boiling point of the solvent.  $^1\text{H}$  NMR and DSC were used to confirm the complete removal of the solvent. Samples were then weighed and loaded into MAS rotors in the glove box. The packed rotors were put in a vacuum oven over night at about 140 °C to anneal the sample. Nitrogen from a liquid nitrogen dewar was used to run the MAS to minimize oxygen exposure to the sample.

Solid-state  $^1\text{H}$  NMR spectra were collected on an Apollo console (Tecmag) operating at 299.79 MHz with a Doty magic angle spinning (MAS) probe DSI-1231. Spectra were recorded using a spinning speed between 15 and 20 kHz. Variable temperature experiments were done with a Doty temperature controller. A spectrum was taken every few minutes until there were no differences between spectra. Further proton relaxation experiments were run at each temperature (Hahn Echoes, Inversion Recovery, etc.) for all the samples with varying delay time. All chemical shifts are reported with adamantane as a secondary reference at 1.62 ppm.

Relaxation data were analyzed by fitting integrated peak intensities using Mathematica.

## 2.5 Results and Discussion

Fast spinning MAS and elevated temperatures are necessary to achieve decent proton spectrum resolution due to the homogeneous broadening of this dense proton system. This presents complications with experimental set-up but has an advantage in that the relative mobilities of the moieties can be compared by analyzing their linewidths. The

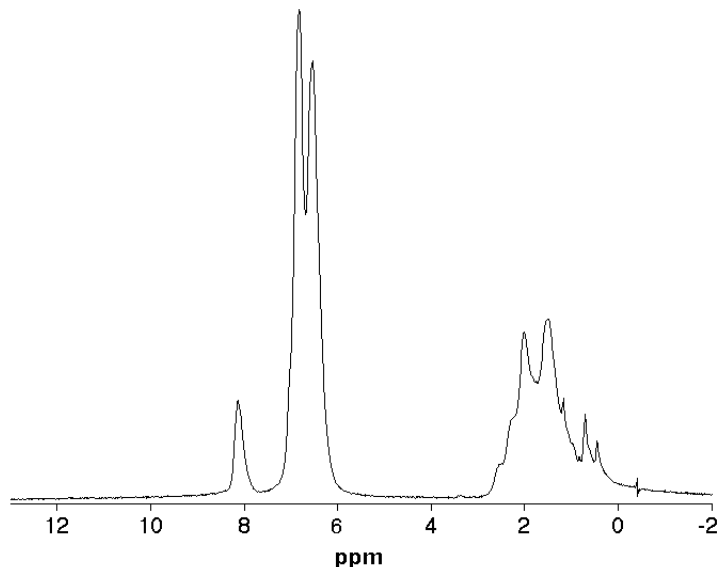


Figure 2.2:  $^1\text{H}$  NMR spectrum of poly(styrene-*block*-2-vinyl-pyridine) at 20 kHz MAS and 150 °C

objective is to see how the mobility and chemical environments change with the addition of ionic liquid.

### 2.5.1 Poly(styrene-*block*-2-vinyl-pyridine)

Figure 2.2 shows the  $^1\text{H}$  NMR MAS of S2VP. This spectrum features peaks in the aliphatic region (0-4 ppm) which comprise the polymer backbone linkers. These are generally broad, implying restricted motion. The aromatic region (6-8 ppm) presents as three peaks including two that overlap. Other non-equivalent aromatic peaks are not resolved. The peak around 8.0 ppm is the proton bound to the carbon adjacent to the nitrogen in the pyridine ring. Note this spectrum is taken at 150 °C, about 50 °C above the  $T_g$  of both the PS and P2VP blocks. Lowering the temperature to near the  $T_g$  diminishes resolution greatly.

### 2.5.2 S2VP/[Im][TFSI]

Figure 2.3 shows the spectrum under the same conditions as Figure 2.2 but with a volume fraction  $\psi_{[IM][TFSI]}$  of 29%. This corresponds to an overall polymer weight fraction of 61%. From a stoichiometric perspective, this equates to one imidazole for every two pyridines. The features of the spectrum are much more complex than just the simple addition of sharp peaks to the previous spectrum. The sharp peaks at 7 ppm and 8 ppm

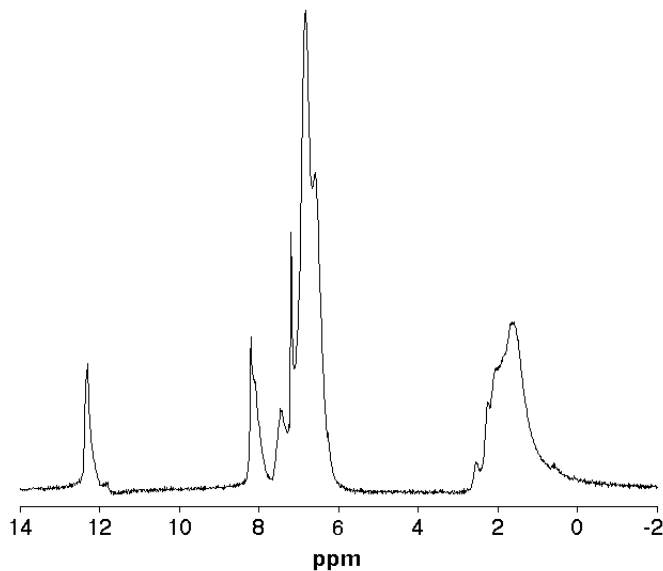


Figure 2.3:  $^1\text{H}$  NMR spectrum of S2PV/[Im][TFSI] 61%wt polymer at 20 kHz MAS and 150 °C

correspond to the covalently bound basal and apical protons of imidazole, respectively. The large peak downfield ( $> 11$  ppm) comprises the mobile imidazole protons bound to nitrogen. A new peak has emerged near 7.4 ppm, and the two large aromatic peaks show more overlapping. Quantitative analysis of proton populations shows that all of the mobile protons from imidazolium are accounted for in the spectral region around 12 ppm.

Previous studies have shown that the  $T_g$  of the P2VP phase at this concentration is about 30 °C. However, the linewidths of the aromatic resonances are not significantly reduced compared to those in Figure 2.2. Instead, only a slight shift downfield causes the two main peaks to overlap. This is evidence of the PS phase maintaining structural rigidity even though the P2VP phase is plasticized. More surprisingly, the aliphatic peaks are even less resolved than before. The general downfield shift of pyridine resonances is clear evidence of protonation of the pyridine ring. One possible explanation is that imidazolium coordination hinders some geometric mode of the motion of pyridine despite an overall drop in  $T_g$ .

### 2.5.3 [Im]/[TFSI]

To further elucidate the protonation state of imidazole in the mixture, Figure 2.4 shows a  $^1\text{H}$  NMR MAS spectrum of neat ionic liquid. The sample was packed inside a teflon plug which was put in the rotor to protect the sample more thoroughly from air and



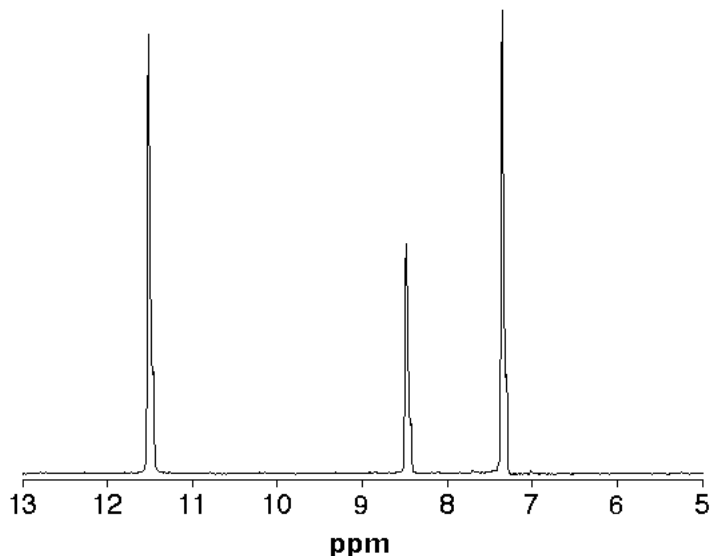


Figure 2.4:  $^1\text{H}$  NMR Spectra of  $[\text{Im}][\text{TFSI}]$  at 8 kHz MAS and 90  $^\circ\text{C}$

also prevent crashing when the melting point was reached. It should be noted that for these studies a 5:5 ionic liquid was used. This nomenclature means that equimolar parts of imidazole and bis-(trifluoromethanesulfonyl)amide (HTSFI) are mixed. The HTSFI, being a very strong acid, donates a proton to imidazole in such a fashion that no excess imidazole is left unprotonated as well as no excess acid protons exist. We see in Figure 2.4 three peaks, which are from the five protons on the imidazolium. The symmetric 5:5 mixture of imidazole and HTSFI produces a higher melting point than non-symmetric combinations, some of which are liquids at room temperature. A melting point of 73  $^\circ\text{C}$  has been reported for the 5:5 mixture[6]. It can be seen that above the melting point, the peaks become very sharp. Most importantly, the linewidths of all the peaks are roughly equal which implies liquid like motion and no exchange broadening of the mobile proton.

In general, imidazoles show a downfield shift of  $^1\text{H}$  resonances upon protonation to the cationic form. This occurs because of diminished electron density overall upon the addition of a positive charge. With the extra proton, the chemical shift difference between its apex proton and base protons increases. Table 2.1 displays the imidazolium chemical shifts of neat and polymer-imbibed ionic liquid. The 5:5 neat ionic liquid represents imidazole in its fully protonated state. When added to the polymer, the apical and basal shifts decrease (upfield shift) as does the difference between them. This implies a less cationic imidazole wherein some imidazoles shed protons to some degree. Therefore, the polymer provides a proton sink, the most obvious location being the pyridine ring in the P2VP phase. The pKa value of P2VP's conjugate acid is approximately 4.5 while that of

Table 2.1: Summary of proton chemical shifts for imidazolium in neat ionic liquid and 61%wt polymer

| Sample          | Mobile    | Apical   | Basal    |
|-----------------|-----------|----------|----------|
| Neat [Im][TSFI] | 11.50 ppm | 8.48 ppm | 7.35 ppm |
| 61%wt polymer   | 12.30 ppm | 8.19 ppm | 7.19 ppm |

imidazole is around 7 [16]. Of course, these metrics are derived from acid-base equilibrium experiments in aqueous environments with solvent dependent effects. Translating acid-base interactions to the solid state is less predictable, especially when mixing a polymer with a solvent with a clear solid-liquid transition.

The mobile proton has an opposing behavior in that the chemical shift moves even farther downfield upon polymer addition. The plausible explanation is that creating neutral imidazoles provides hydrogen bonding opportunities between the imidazoles. In addition, hydrogen bonding between imidazole and pyridine is also possible.

One major aspect not mentioned yet has been the unusual linewidth of the mobile proton in the polymer ionic liquid mixture. Figure 2.5 displays the typical linewidth of pure IL as a function of temperature. Through the phase transition, there is a marked change in the chemical shift owing to the effects of motion on the average bonding environments. Does imidazolium in the polymer mixture act like a solid or liquid then? At high temperatures, well above the P2VP glass transition (such as in Figure 2.3), the answer seems to be liquid as indicated by the sharp imidazole peaks. However, as the temperature is lowered and approaches the glass transition, it is less clear when the liquid-like behavior will cease.

#### 2.5.4 P2VP at low pH

Another fluctuating environment not mentioned is the complete transfer of a proton to pyridine. To assess this transfer, a polymer sample was washed with hydrochloric acid to guarantee complete protonation of the weak pyridine base before being dried. Figure 2.6 details the consequences fully protonating the pyridine. Firstly, there is significantly more broadening of the aliphatic region compared to the standard polymer in Figure 2.2. The aromatic region resembles that of the Figure 2.3 with a styrene peak unaltered and pyridine peaks shifted downfield. The most interesting feature is that a new peak has appeared around 8.5 ppm and has the same intensity as the peak at 8.0 ppm. This is most probably the transferred acid proton bound to the nitrogen on the pyridine. This experiment provides the non-exchanging chemical shift of a proton that is completely donated to the polymer, which is a plausible species to obtain when species with different pKa's are mixed. However the one chemical environment that has not been accounted for is the free neutral imidazole. This state is possible if a cation donates its proton and then did not engage in another hydrogen bond. The chemical shift of this "free" state has

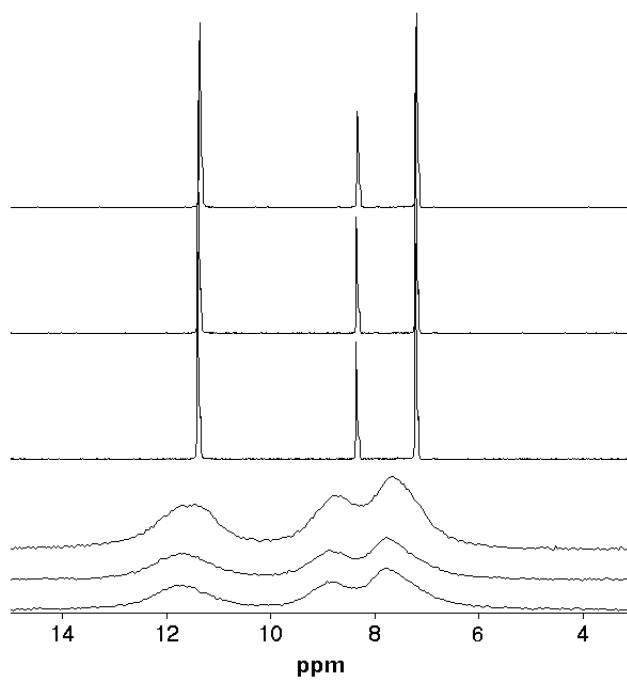


Figure 2.5: Variable temperature  $^1\text{H}$  NMR spectrum of 5:5 [Im][TSFI] at 8 kHz MAS. The temperatures are (bottom to top) 45 °C, 55 °C, 65 °C, 75 °C, 85 °C and 90 °C.

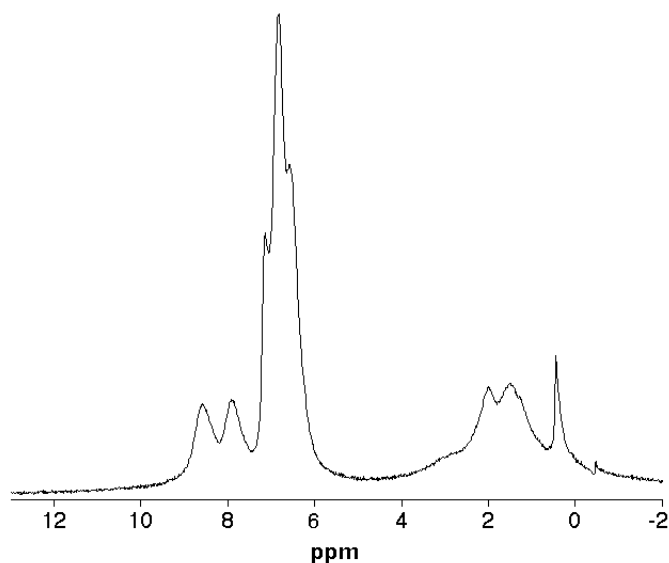


Figure 2.6: S2VP with HCl at 20 kHz MAS and 150 °C

been calculated to be 9.0 ppm[17].

### 2.5.5 Variable Temperature NMR

Figure 2.7 shows the variable temperature proton spectra of S2PV/[Im][TSFI] 61%wt polymer as a function of temperature. These are in fact spectra resulting from signals after Hahn Echoes with the same relatively short echo time. Hahn echo experiments act as a spectral filter for protons that have substantial homonuclear dipolar interactions, such as the styrene moieties in the polymer. A significant feature of this graphic is the general line narrowing as temperature increases. This is especially true in the aromatic region where the polymer linewidth is so large that it disappears in the Hahn echo experiment, and only the three ionic liquid resonances remain. Above 100 °C, near  $T_g$  of the styrene block, the polymer signal is more prevalent and can survive the echo experiment. The aliphatic peaks also respond above 100 °C, when segmental motion in the PS block begins.

A striking feature of the data set is the upfield shift of the mobile peak as temperature increases. It also narrows and seems to reach a limiting linewidth. This is interpreted as a coalescence process between hydrogen-bonded protons, free protons (neutral and cationic imidazole), and protons transferred to the polymer. The chemical shift trend implies a weak hydrogen bonding network in a disordered and mobile phase.

The same experiments were performed for other concentrations of [Im][TSFI] in the same polymer. The samples in this study are summarized in Table 2.2.  $w_{IL}$  refers to the

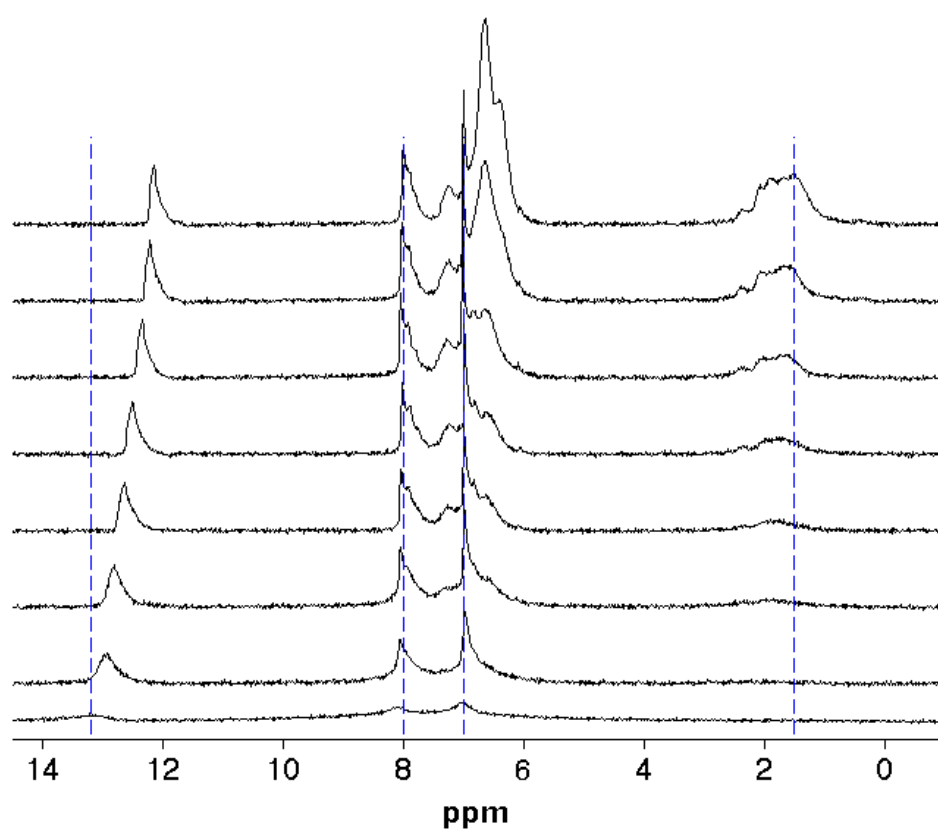


Figure 2.7: Variable Temperature  $^1\text{H}$  NMR of S2PV/[Im][TSFI] 61%wt polymer at 20 kHz MAS. The temperatures are (bottom to top) 45 °C, 60 °C, 75 °C, 90 °C, 105 °C, 120 °C, 135 °C and 150 °C.

| Sample | wt% polymer | $\psi_{[IM][TSFI]}$ | T <sub>g</sub> P2VP phase (°C) | $w_{IL}$ |
|--------|-------------|---------------------|--------------------------------|----------|
| 1      | 61          | 0.29                | 30                             | 0.62     |
| 2      | 74          | 0.18                | 50                             | 0.48     |
| 3      | 82          | 0.12                | 72                             | 0.36     |
| 4      | 91          | .06                 | 88                             | 0.20     |

Table 2.2: List of S2VP/[Im][TSFI] samples

weight fraction of ionic liquid in the P2VP phase only. Figure 2.8 shows the temperature trend for all samples. Immediately it is clear that larger concentrations of [Im][TSFI] lead to larger chemical shifts. This indicates that more hydrogen-bonding character exists. The least hydrogen-bonding occurs in the sample with the least amount of ionic liquid. This is most easily explained from the point of view of concentration; there are simply less bonding candidates in the sample. Only the most concentrated sample has larger chemical shifts than the neat 5:5 ionic liquid (which is basically in its cation form at all times and shows a shift around 11.5 ppm). Another subtle feature is that the relative dependence on temperature is slightly stronger with lower concentrations. Obviously, the nature of the hydrogen bond network is quite different throughout the series of samples. The 91%wt. sample has a pyridine to imidazole ratio of about 14, so the basic nature of pyridine will be more dominant, leading to more protonated pyridine character and smaller chemical shifts.

The data set for lesser concentrations are not as complete as those for higher concentrations. The reason for this is the increasing T<sub>g</sub>, which reduced resolution at lower temperatures such that the chemical shift could no longer be measured with other peaks overlapping it. At times echoes were used to eliminate less mobile peaks first, but this technique had its limits as well.

### 2.5.6 Effect of Confinement

Thus far, only nanostructured block copolymers with lamellar morphologies have been investigated. The hope is that the ion conducting phase will form precise channels to facilitate conduction. Not unexpectedly, it's possible that hydrogen bonding and proton conduction mechanisms are fundamentally different near phase boundaries. Studies have already shown that these effects are present in Nafion[18]. To study possible confinement effects in this system, variable temperature MAS experiments were conducted on homopolymer analogues in which the ionic liquid concentration is identical to those of the P2VP phase of the diblock copolymer. Figure 2.9 shows the <sup>1</sup>H MAS NMR spectrum of [Im][TSFI] imbided in poly(2-vinyl pyridine). The ionic liquid concentration corresponds to exactly the as that found in Sample 1 from Table 2.2. The spectrum is very similar to that of the block copolymer, with a few differences. Because the stiff polystyrene phase is no longer present, the resolution of both the aliphatic and aromatic phase is improved. In

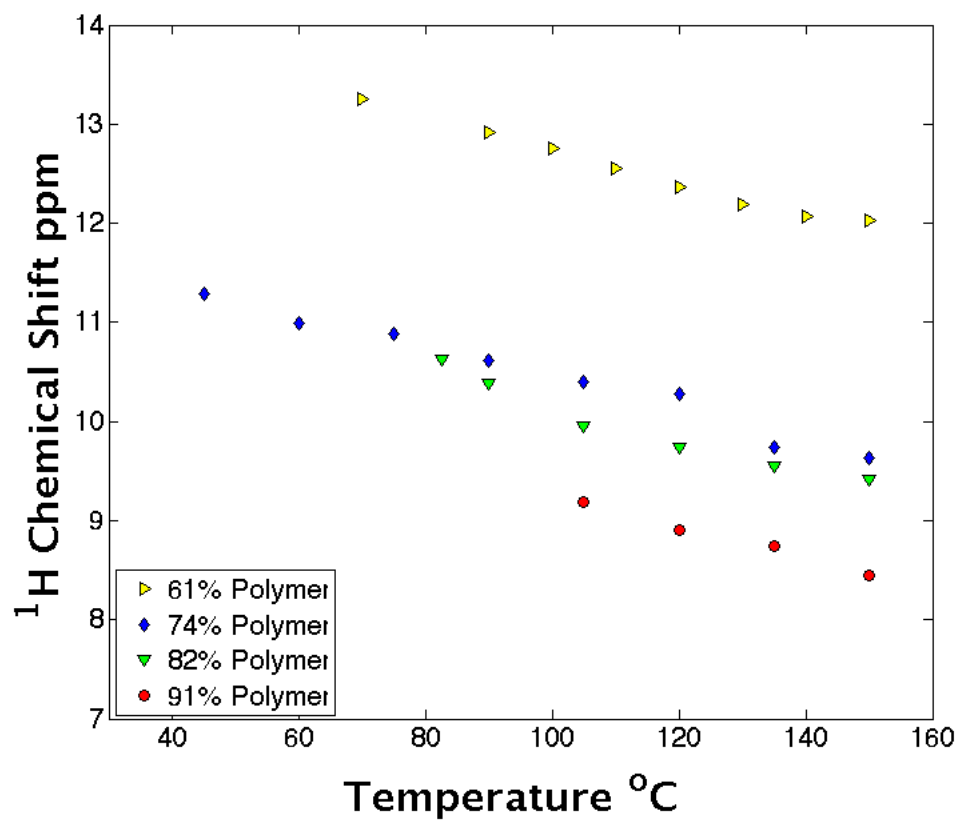


Figure 2.8: Mobile proton chemical shifts as a function of temperature for S2VP/[Im][TSFI]

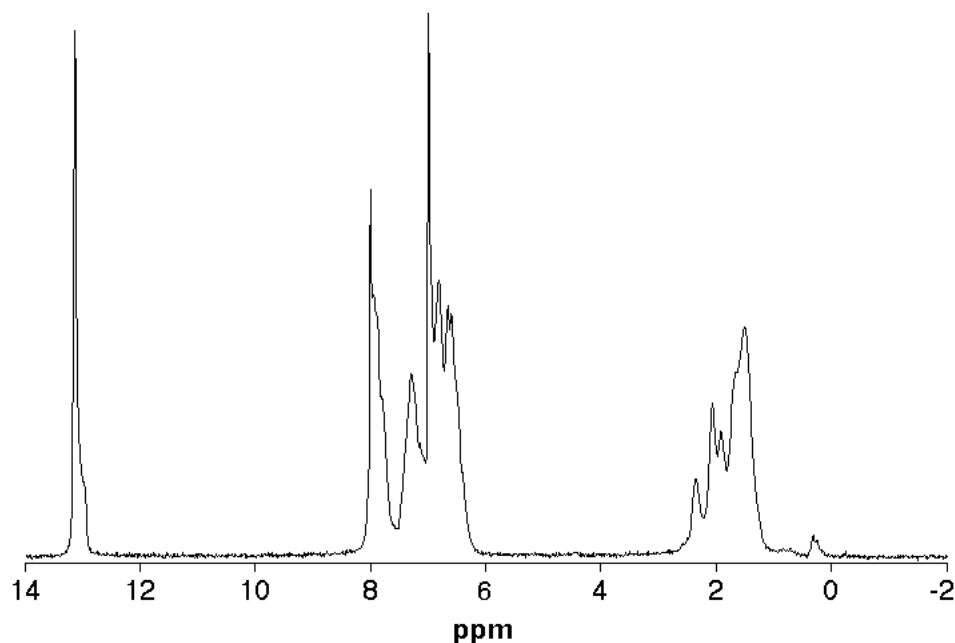


Figure 2.9:  $^1\text{H}$  NMR spectrum of P2VP/[Im][TSFI] at 20 kHz MAS and 150  $^\circ\text{C}$

fact, all four pyridine ring protons are decipherable. The apical and basal proton chemical shifts of the imidazolium appear the same as the S2VP system, but the mobile proton is further downfield. For a direct comparison, a library of homopolymer/ionic liquid samples corresponding to the same P2VP phase concentrations in Table 2.2 were measured using VT  $^1\text{H}$  MAS NMR. Figure 2.10 shows an almost identical trend as Figure 2.8. High concentrations of IL produce lots of hydrogen-bonding character whereas lower concentrations display much less. Once again, increasing temperature breaks up the hydrogen bonding characteristics, implying a more mobile, dynamic network.

To demonstrate the effect of confinement, Figure 2.11 shows the whole suite of data concerning the mobile proton shift. It is clear that the homopolymer results show an overall increase in chemical shift especially at higher concentrations. An important but subtle trend is the slope of the line. The block copolymers show a steeper response to increasing temperature. This is further evidence that the nature of the hydrogen bonding network is different. Similar results were found in other studies using a 8:2 [Im][TSFI] ionic liquid[19]. Also reported was an enhanced proton hopping mechanism in the confined system. Putting this all together, a steeper slope in the chemical shift vs. temperature plot could mean simply that the hydrogen bonds in the block copolymer have shorter lifetimes because they are less stable (temperature sensitivity) so they pass protons at a faster rate.



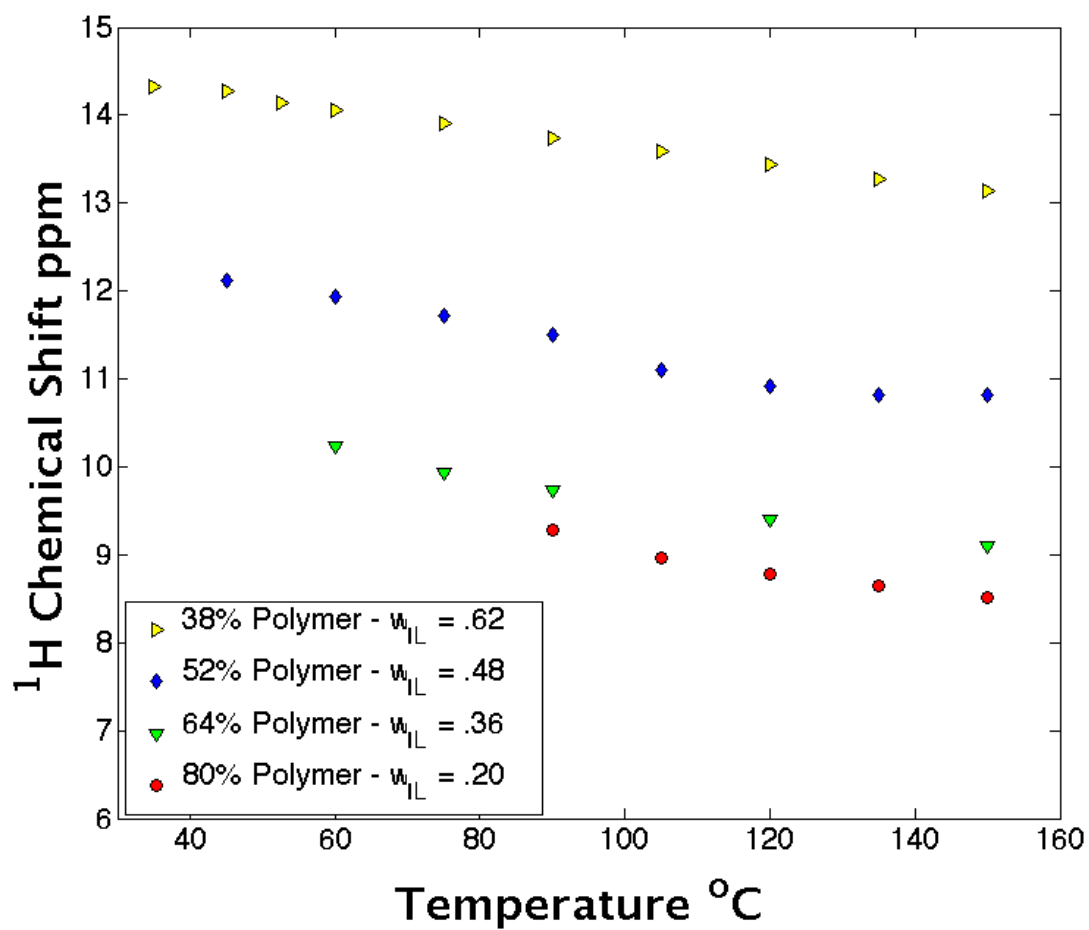


Figure 2.10: Mobile  $^1\text{H}$  chemical shift as a function of temperature for P2VP/[Im][TSFI]

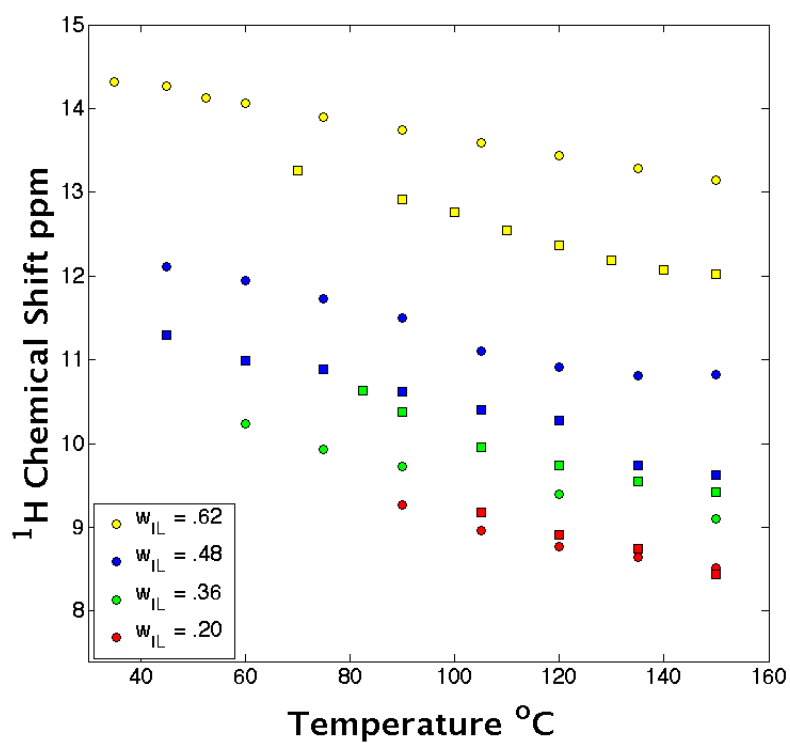


Figure 2.11: Comparison of P2VP/[Im][TSFI] and S2VP/[Im][TSFI] mixtures. The homopolymers appear as circles, and the block copolymers are squares.

| Sample                            | Mobile    | Apical   | Basal    | $w_{IL}$ |
|-----------------------------------|-----------|----------|----------|----------|
| Neat [Im][TSFI]                   | 11.50 ppm | 8.48 ppm | 7.35 ppm | 1.00     |
| 74%wt S2PV/[Im][TSFI] with 5:5 IL | 9.63 ppm  | 7.92 ppm | 6.98 ppm | 0.50     |
| 70%wt S2PV/[Im][TSFI] with 8:2 IL | 13.00 ppm | 7.66 ppm | 6.86 ppm | 0.48     |

Table 2.3: Summary of proton chemical shifts for imidazole in similar polymer mixtures and neat ionic liquid at 150 °C

### 2.5.7 Non-symmetric [Im][TSFI]

Only 5:5 symmetric [Im][TSFI] has been discussed so far. However, when making this ionic liquid, many ratios of the two components can be combined. Mixtures that are not evenly balanced will have species which are neutrally charged. In the case of mixtures that have excess imidazole, this enhances hydrogen-bonding greatly and increases Grotthus behavior[6]. Figure 2.12 shows an MAS spectrum of a block copolymer sample with a non-symmetric ionic liquid that is four parts imidazole and one part HTSFI. The key difference that arises is the more neutral nature of the imidazole C-H protons as seen by their smaller chemical shifts. The basal and apical peaks are both shifted upfield toward the typical shifts of neutral imidazole. Table 2.3 shows this by comparing the imidazole C-H proton shifts to the fully cationic form of the neat IL and that of a very similar symmetric IL/polymer sample. Importantly, there is still only one peak for each type of proton. Even though there is more neutral imidazole, fast exchange between neutral and cationic states presents only one peak at the average frequency.

The mobile shift, like that in pure ionic liquid, show a trend of more hydrogen bonding character as also seen in Table 2.3. Figure 2.13 shows a comparison between the mixtures with very similar weight fractions of ionic liquid in the PV2P phase. The polymer molecular weights and ratios of PS to P2VP are similar as well. There is a marked increase in the hydrogen bonding character as expected due to the presence of neutral imidazole. More interestingly, the slopes of the lines are nearly identical. As seen before, confinement leads to larger slopes for the 5:5 ionic liquids. Thus, it seems that confinement is the major factor in determining the temperature dependence of the chemical shifts, as opposed to the relative amount of hydrogen-bonding character.

## 2.6 Conclusions

In this work,  $^1\text{H}$  NMR at variable temperatures was used to investigate the proton environments of a suite of mixtures containing protic ionic liquid combined both diblock copolymers and a homopolymer that comprised one of the diblock constituents. The concentration of the ionic liquid in the miscible phase was varied. The transferable proton of the ionic liquid showed high sensitivity to temperature for all the samples, demonstrating a chemical exchange network of hydrogen bonds. The trend was a monotonic decrease

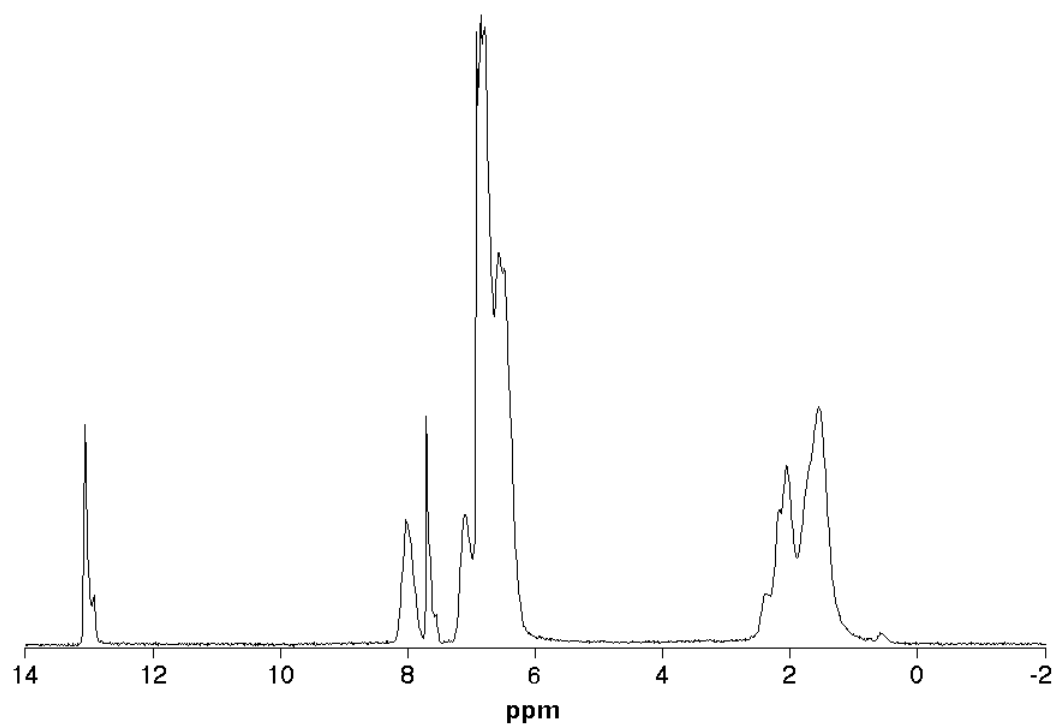


Figure 2.12:  $^1\text{H}$  NMR of S2PV/[Im][TSFI] 70%wt polymer at 20 kHz MAS and 150 °C with 8:2 ionic liquid

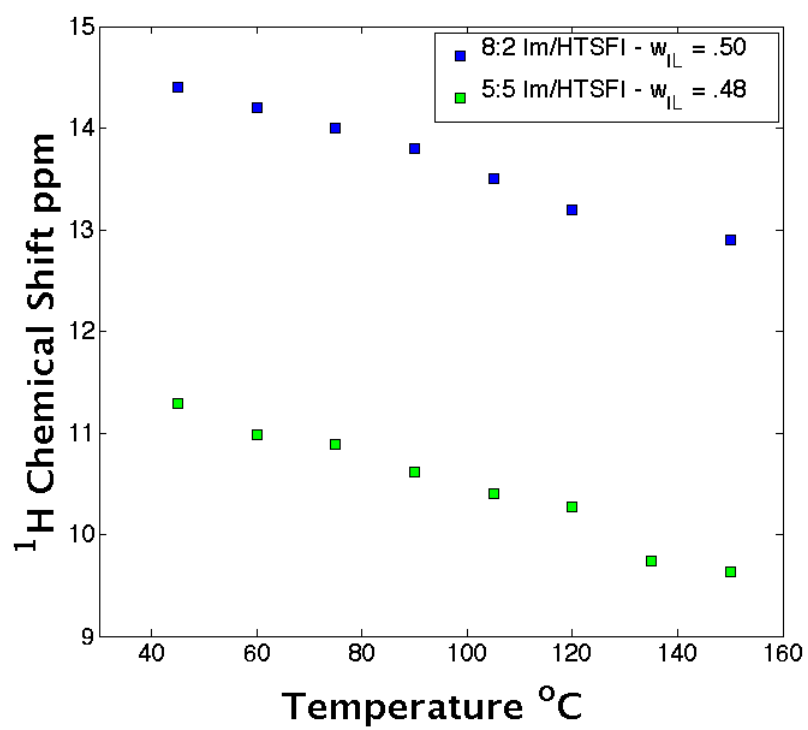


Figure 2.13: Comparison of mobile proton chemical shifts for S2VP/[Im][TFSI] with different ionic liquids symmetries

in the chemical shift with increasing temperature, which is congruous with destabilizing hydrogen bonding events and reducing their lifetimes. No bookend chemical environments could be seen in any spectrum, indicating that this study was conducted well into the fast exchange limit.

A block copolymer was compared to its homopolymer analogue where the ionic liquid concentration in the miscible phase was kept constant. Homopolymer samples showed significant increases in chemical shifts, especially at large concentrations. More subtly, the sensitivity to temperature was larger in the block copolymer samples. This implies that the nature of hydrogen bonding is different in confined channels vs. bulk polymer. Finally, the effect of imbibing a non-symmetric ionic liquid with neutral imidazoles which boost hydrogen bonding behavior was discerned. However, the sensitivity of proton chemical shifts to temperature was quite similar to the copolymers imbibed with symmetric ionic liquid, indicating that confinement was most influential in proton transfer mechanics.

## Chapter 3

# Proton Mobility and Activation

### 3.1 Acknowledgment

The author gratefully acknowledges the contribution of Dr. Megan Hoarfrost, a former graduate student in the group of Rachel Segalman in the Department of Chemical and Biomolecular Engineering at UC Berkeley for providing samples for this study and teaching synthetic techniques.

### 3.2 Introduction

The overall degree of proton coordination has been studied in the previous chapters, but the real metric of merit of a possible proton-conducting material is the ease with which protons move throughout the system. The difficult part is to assess the various length scales in the system. For instance, the ease with which a proton or proton-carrier moves back and forth in a nanoscale cavity is probably not the full story as to how easily it moves from one side of a macroscopic material to the other. The connectivity of the channels and tortuosity play a major role. For example, recently it was shown that extruding Nafion can align the ionic channels to such a degree that diffusion becomes anisotropic with respect to through-plane or in-plane diffusion[20]. Such geometric constraints could be possible in nanostructured block copolymers. The motion of the polymer is also of interest. Like surfers riding a wave, the ion transport will depend on the motion of the medium to which they are coupled. In such cases, segmental motion is an important factor, and simple Arrhenius rate behavior is not appropriate, leading to more empirical models such as the Vogel-Tamman-Fulcher model.

Traditional measurements of conduction sample macroscopic length scales. Nuclear magnetic resonance has the advantage of living in the microscopic. In this study, proton linewidths in the fast exchange limit are used to delve into the general mobility of transferable protons. This NMR method yields a local proton mobility that is likely devoid of grain boundary, connectivity, and tortuosity concerns. While it may seem ill-conceived to

focus on a measurement that doesn't reflect the actual real-world conductivity, the local mobility governs the maximum flux for a system. Additionally, comparison of bulk and local mobility helps in modeling and calculating the magnitude of the other long-range factors that hamper and boost conduction.

### 3.3 Methods

The samples and preparation are the same as the previous chapters. Solid state  $^1\text{H}$  NMR spectra were collected on an Apollo console (Tecmag) operating at 299.79 MHz with a Doty magic angle spinning (MAS) probe DSI-1231. Spectra were recorded using a spinning speed between 15 and 20 kHz. Nitrogen from a liquid nitrogen dewar was used to run the MAS to minimize oxygen exposure to the sample. Variable temperature experiments were done with a Doty temperature controller. After a temperature change, spectra were collected until no differences were detectable. This usually took 30-45 minutes. The spinning rate was monitored, and the air flow was altered after temperature changes to rectify any changes in spinning speed. Standard Hahn echoes were used with increasingly longer delay times,  $\tau$ , to determine the spin-spin relaxation time  $T_2$ . The data were analyzed with Mathematica using a non-linear regression models of a single exponential decay process. There was no evidence for more than one characteristic decay time. An example of the script is located in the Appendix.

## 3.4 Results and Discussion

### 3.4.1 Activation Energy and Local Proton Mobility

In many polymer/ion mixtures, the ionic conductivity is only significant above a temperature known as the Vogel temperature, which is a simple function of the glass transition temperature. This reason is that the ions are dependent on the segmental motion of the polymer in order to move. Materials that are conductive below the Vogel temperature must rely on ion hopping between sites or more limited motions of the polymer chain[21], leading to Grotthus-like proton hopping rate. Therefore an Arrhenius like temperature dependence is possible.

Such a process would be characterized by a short  $T_2$  at low temperatures. As the temperature increases, the  $T_2$  increases due to increased proton hopping and thus averaging of anisotropic interactions with respect to the magnetic field. Eventually a minimum linewidth will be reached, representing the inherent linewidth of the  $^1\text{H}$  resonance. At this point, the molecular averaging of anisotropies by motion no longer dominate the line-shape. A typical analysis is shown for our standard S2VP/[Im][TSFI] polymer in Figure 3.1. The ordinate here is a fit of the NMR intensity to an exponential decay model. When plotted as an Arrhenius plot, the data demonstrate a curvature at higher temperatures. As the sample is cooled, the curvature lessens, and a linear regime occurs. Analogous



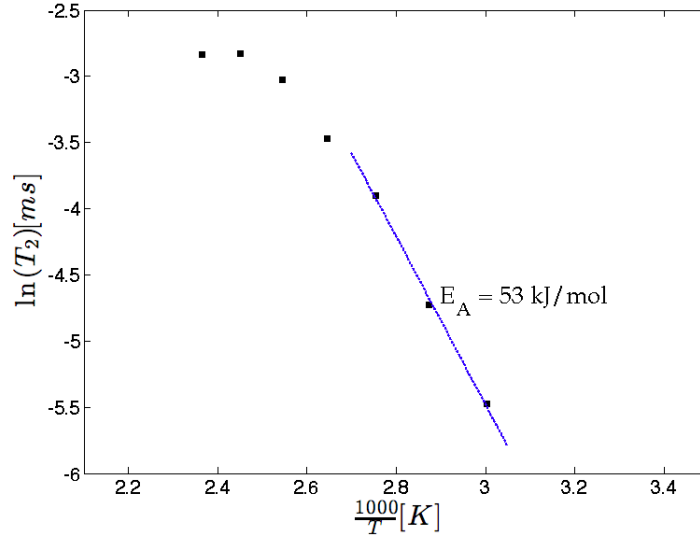


Figure 3.1: Temperature-dependent transverse relaxation of mobile  $^1\text{H}$  resonance for S2VP/[Im][TSFI] 61%wt. polymer

to conductivity vs. temperature analysis from AC impedance, Figure 3.1 displays both VTF like behavior and Arrhenius behavior. The interpretation is that, in the low temperatures regime, proton hopping is the main mechanism of proton mobility. At high temperatures, segmental motion becomes the dominate factor. There is evidence of the  $T_2$  reaching its inherent limit at the highest temperature as the slope is practically zero. The activation energy in the Arrhenius region is 56 kJ/mol. This is within about 15% of similarly measured activation energies for other imidazole-based polymer and glassy systems[17][22][23].

The unusual aspect of this behavior is that the  $T_g$  of the P2VP phase is about 30 °C. The Arrhenius regime of Figure 3.1 is valid until 85 °C. Segmental motion should be occurring well within this temperature range. One possibility is that proton hopping is much faster than segmental motion. Enhancing the plausibility that proton hopping dominates the motional rate is the idea that the styrene block of this lamellae morphology helps reduce the effects of segmental motion. Even though differential scanning calorimetry (DSC) of this sample shows two glass transitions—one for the PS block and one for the P2VP/[Im][TSFI] block—the motion above the P2VP glass transition is being diminished. Figure 3.2 shows the temperature-dependent transverse relaxation rate for all four S2VP samples. Figure 3.3 shows the slopes of the line of best fit. The slope for the highest polymer fraction sample can only be estimated due to the inaccessibility of data points at lower temperatures due to the short  $T_2$  of samples with higher glass transitions. However, the slope between the last two accessible data points serves as a slope minimum as any more curvature would only lead to a larger slope within the linear regime.

There is an obvious trend of increasing activation energy with lower ionic liquid concen-

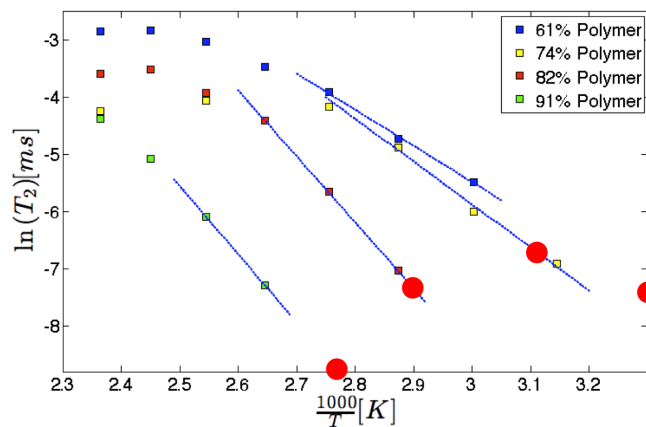


Figure 3.2: Temperature-dependent transverse relaxation of mobile  $^1\text{H}$  resonance for S2VP/[Im][TFSI] samples. The red sphere is located at the  $T_g$  of the respective P2VP phase and placed along the line of best fit of the Arrhenius fit.

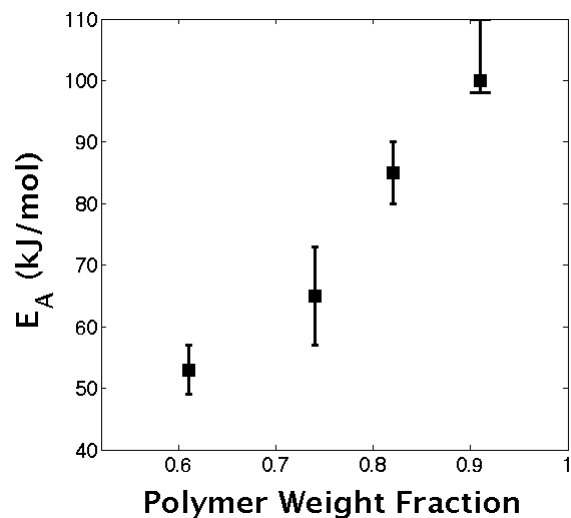


Figure 3.3: Arrhenius activation energies of S2VP/[Im][TFSI]. Error generated from multiple experiments.

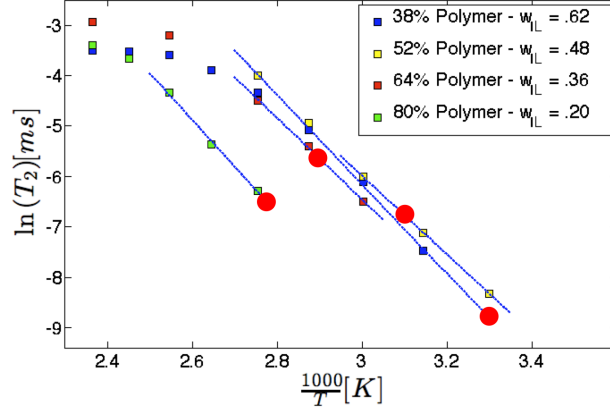


Figure 3.4: Temperature-dependent transverse relaxation of mobile  $^1\text{H}$  resonance for P2VP/[Im][TFSI] samples. The red sphere is the  $T_g$  of the respective P2VP phase placed along the line of best fit of the Arrhenius fit.

trations. Temptation looms to simply state that the higher glass transition temperature of the polymer means that more energy is required to move the proton. This is a valid argument in the non-Arrhenius regime where segmental motion is the dominant motional mode. However, these linearly-fit activation energies reflect hopping rates of protons in distinctive, hydrogen-bonded states. Therefore, the data reflect the idea that higher concentrations of ionic liquid facilitate these hops to occur faster or in a manner that provides more motional amplitude.

Another interesting aspect that must be considered is that the temperature range where the slope is calculated is different for all four samples. In this case, the glass transition trend can be used to suggest that at the temperature when a highly doped polymer shows the transition to segmental motion dominated line narrowing, a sparsely doped polymer would still be resisting motion and in the proton hopping regime.

To investigate the idea that the confinement in a morphologically patterned polymer is influencing this behavior, the same set of experiments were performed in the homopolymer analogues. Figure 3.4 displays the same line narrowing phenomena as the block copolymer linewidths. Once again there is an Arrhenius activation regime in the experimental temperature range. However, we see that the  $T_g$  values, indicated by the large circles, are much closer (temperature wise) to the Arrhenius/segmental motion transition. In other words, the proton hopping motion regime is much less resistant to the thermal energy that causes segmental motion to dominate at higher temperatures. This supports the hypothesis that the PS phase in the diblock copolymer contributes to reducing the motion in the P2VP phase as the temperature increases. Figure 3.5 lists the activation energies once again derived from the line of best fit.

The activation energies have similar magnitudes to the diblock polymer; however, they vary much less. Not only are the slopes more similar, but the lines almost collapse onto each other. From a physical perspective, the only difference between the homopolymers

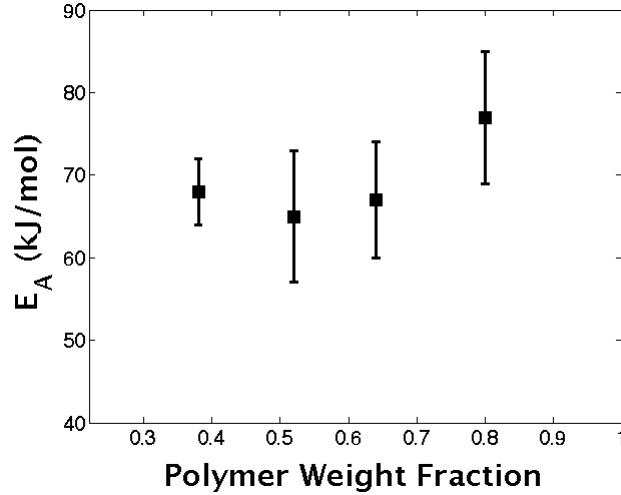


Figure 3.5: Arrhenius activation energies of P2VP/[Im][TSFI]. Error generated from multiple experiments.

and the block copolymers is the morphology. The ionic liquid concentrations in the P2VP blocks are identical. The energies are similar in the homopolymer, even though the degree of hydrogen bonding is quite different (see Figure 2.11). This means that this rate process is not a function of hydrogen bonding and supports the idea that confinement affects the rate greatly. Confinement would reduce the diffusion coefficient of ionic liquid in the polymer. A study has shown this is true for an 8:2 non-symmetric ionic liquid[19].

### 3.4.2 Entropic Contributions

If confinement were a significant factor in proton conduction, one should expect entropy to possibly play a role in the thermodynamics of these rate processes.

The rate dependence on temperature is given by

$$k = A * \exp\left(\frac{-\Delta E}{RT}\right)$$

where A is the pre-exponential factor and  $\Delta E$  is the activation energy. The Eyring form of this equation is

$$\frac{k}{T} = \frac{k_B}{h} * \exp\left(\frac{\Delta S}{R} - \frac{\Delta H}{RT}\right)$$

where  $k_B$  is Boltzmann's constant and  $h$  is Planck's constant. If we plot the natural logarithm of  $\frac{k}{T}$  vs  $\frac{1}{T}$ , we have an Eyring plot, with slope  $\frac{\Delta H}{R}$  and intercept  $\frac{\Delta S}{R} + \log\left(\frac{k_B}{h}\right)$ [24]. The rate of interest is related to the effective transverse relaxation rate of the exchanging proton by the relation

$$k = \Omega = \frac{1}{\pi T_2^*}$$

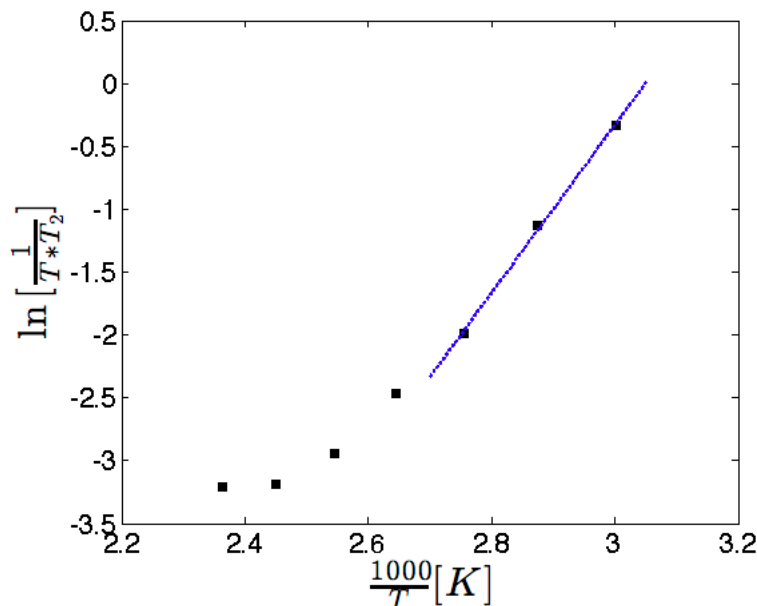


Figure 3.6: Eyring plot for mobile  $^1\text{H}$  resonance for S2VP/[Im][TSFI] 61%wt. polymer

Figure 3.6 shows the exact same data from Figure 3.1 but rearranged in an Eyring form. The ordinate is no longer composed of just  $T_2$ , effectively  $\frac{1}{rate}$ . The reciprocal is used and then normalized to temperature. Plotting the effective rate instead of the inverse rate explains why the plot looks flipped and slope is now positive.

Thus far, only the slope has been quantified, but there is possibly subtle information in the intercept about entropy. Figure 3.7a shows the same data from Figure 3.2 but in the Eyring form. If the lines of best fit are extrapolated to  $1/T = 0$ , Figure 3.7b is generated after the constant term  $\log\left(\frac{k_B}{h}\right)$  has been subtracted out. One must be careful when extrapolating data to a temperature range well out of the scope of the experiments. While the value of the intercept is dubious, comparing one sample's intercept to another is more reliable. The line for the 91% wt. copolymer sample has been omitted because the linearity of the Arrhenius fit could not be assured. However, all indications are that it would indeed have the smallest intercept. We see that the magnitude of the activation entropy increases with less ionic liquid.

Entropy of activation is interpreted the as the change in entropy between a ground state and the top of the transition state. Intramolecular exchange and simple conformational changes in small molecules often display very small entropy of activation [24]. For these types of reactions, it seems unlikely that the transition state would be any more ordered or disordered than the ground state. Also, many polymer relaxation modes of local mobility involving simple, noncooperative reactions show zero entropy activations[25]. Conversely, a hydrogen-bound state would have lower entropy than a transition state due to a decrease in the number of conformation. This has been shown with dynamical simulations[26]. Another factor that limits conformational space is the domain spacing

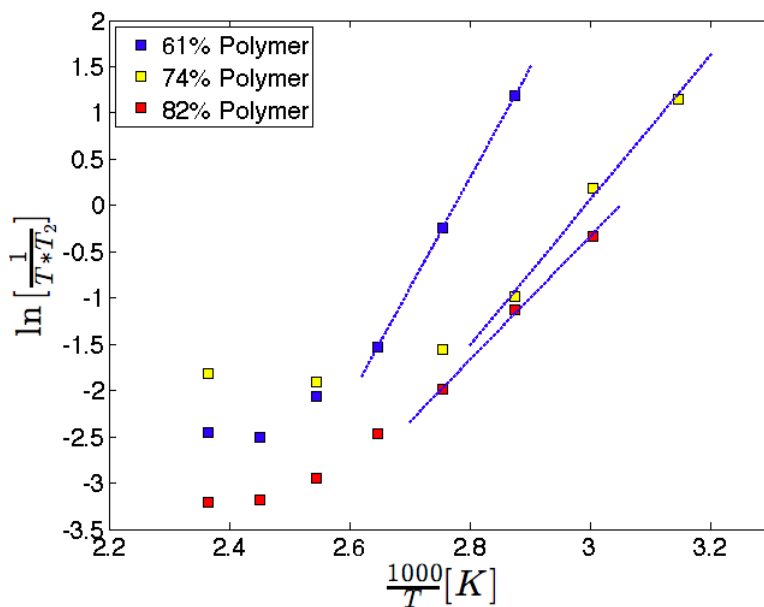
between the lamellae. As ionic liquid concentration decreases, the spacing between the lamellae also decreases as with the relation  $d \sim \Phi p^{-1.1}$ , where  $\Phi p$  is the polymer volume fraction[11]. It seems likely that the shrinking domain size increases the activation entropy of the proton hopping events. This could be achieved by decreasing the configurations available to the hydrogen-bonded species.

The homopolymers were assessed in the same manner and shown in Figure 3.8. The scale in Figure 3.8b is exactly the same as Figure 3.7b. Of course the slopes are very similar as previously mentioned, but now it is apparent that the intercepts are remarkably similar as well, the implication being that the entropy of activation is roughly the same for every homopolymer sample. A numerical comparison between the two figures is a stretch, but comparing the group of lines within each is reasonable. The results seem to imply that there's no difference in entropic activation in the homopolymer samples. This seems to imply that the same proton transfer reactions are occurring in each but with different populations of the various moieties (i.e. equilibrium), hence the chemical shift differences among the samples. Furthering that notion, the changing domain spacing in the copolymer samples alters the entropy differences ( $\Delta\Delta S$ ) between the various reaction pathways.

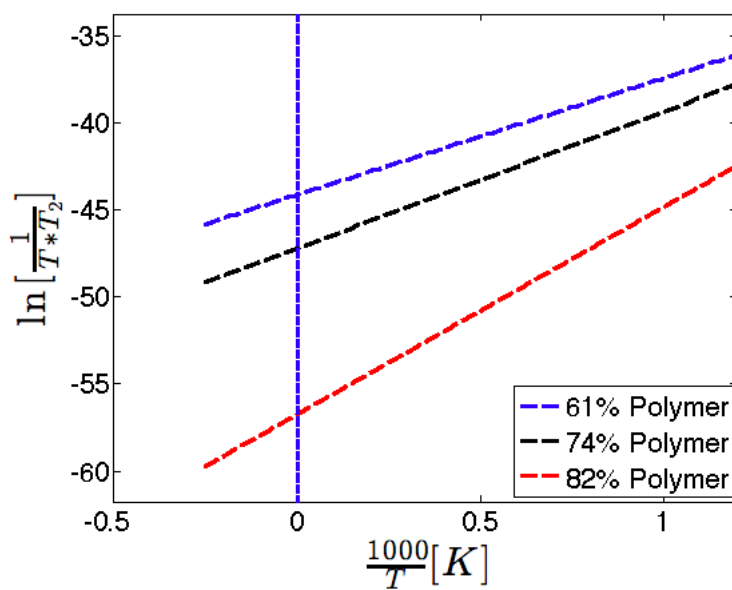
### 3.4.3 Non-symmetric Ionic Liquids

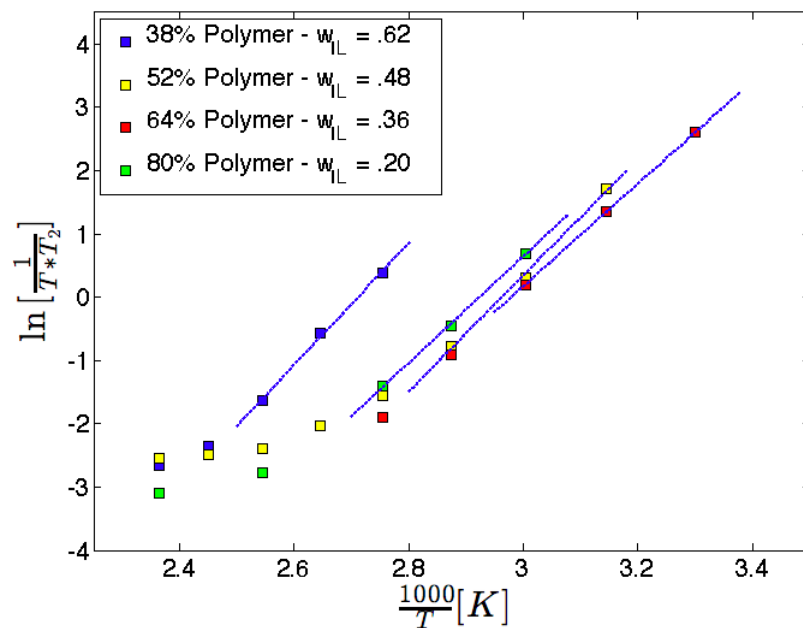
The last interesting variable to consider is non-symmetric ionic liquids. The same analysis was applied to a S2VP/[Im][TFSI] sample with an 8:2 ionic liquid. This sample had a weight fraction of ionic liquid in the P2VP phase of 50%. The MW was also very similar the previous S2VP polymers. Its activation energy is shown in Figure 3.9. This sample has a similar ionic liquid concentration as the 74%wt. polymer S2VP sample. Therefore, its P2VP phase glass transition temperature should also be similar. The only major difference is the asymmetry of the ionic liquid composition. We see that the activation energy is significantly higher in the Arrhenius regime.

It has been shown that this 8:2 mixture shows much more hydrogen bonding character than the 5:5 mixture. Thus, the increased activation energy is attributed to a greater population of protons in hydrogen bonds or longer hydrogen bond lifetimes. Therefore, a greater entropy of activation would also be expected. As a proof of concept, Figure 3.10 shows the Eyring extrapolation to  $1/T = 0$ . The asymmetric ionic liquid shows a markedly increased intercept magnitude, especially compared to the S2VP sample with 48% ionic liquid in the P2VP phase. A comparison of those two alone seems to suggest that more hydrogen bonding character (the 8:2 mixture has already been shown to have this), leads to a higher entropy of activation. Now the argument can be made that higher Arrhenius activation energies will naturally lead to larger intercepts using this method from a simple geometric argument. This is true, but there is probably a physical reason the slope and intercept have such a relation. The slope represents the enthalpy contribution, and the intercept is the entropic. Hydrogen bonds that are very strong take more energy to break. Bonds of this nature would generate larger slopes as functions of temperature



(a) Eyring plots with line of best fit in linear regime

(b) Line of best fit extrapolated to  $1/T = 0$ Figure 3.7: Eyring plots for  $S2VP/[Im][TSFI]$ . The data used are from Figure 3.2.



(a) Eyring plots with line of best fit in linear regime.

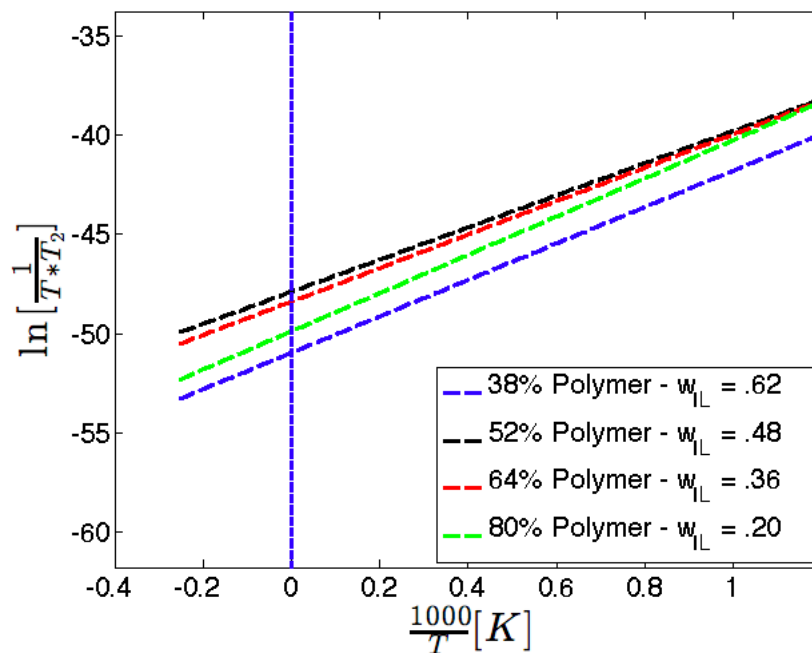
(b) Line of best fit extrapolated to  $1/T = 0$ .

Figure 3.8: Eyring plots for P2VP/[Im][TSFI]. The data used are from Figure 3.4



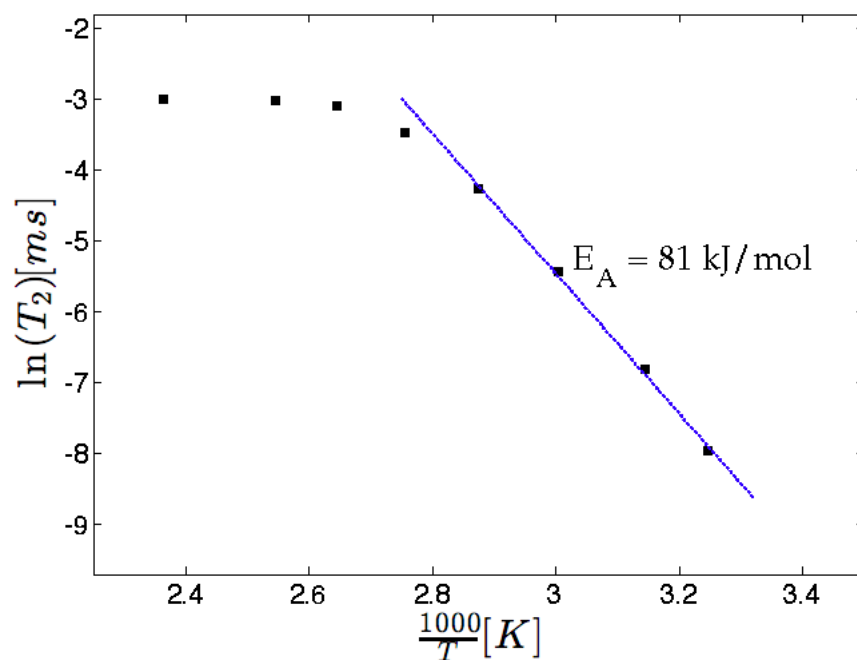


Figure 3.9: Temperature-dependent transverse relaxation of mobile  $^1\text{H}$  resonance for P2VP/[Im][TFSI] with 8:2 ionic liquid

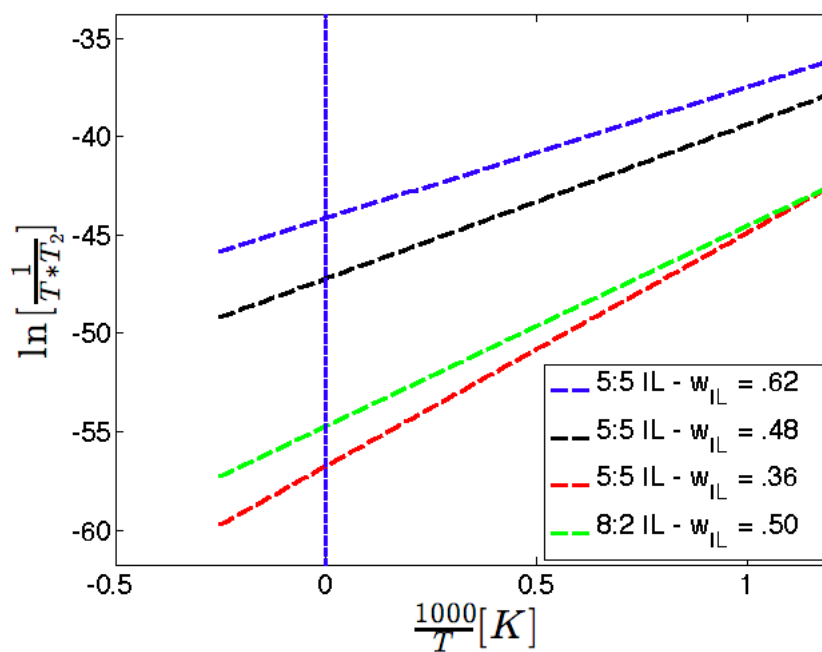


Figure 3.10: Extrapolated activation energy fit to  $1/T = 0$  for S2VP/[Im][TFSI] with asymmetric ionic liquid included

because of the thermal activation barrier required to break them. These strong hydrogen bonds are also more ordered, thus in a low entropy state. Therefore, two extremes are clearly possible. One involves large concentrations of ionic liquid, and motion is easier and hydrogen bonds have many conformational possibilities related to their weak nature. This system has a low activation energy of motion and high entropy in the ground state. The other extreme involves low ionic liquid concentrations, and motion is difficult and hydrogen bonds have a low entropy ground state.

### 3.4.4 Spin-Lattice Relaxation

One relaxation mode not yet considered is spin-lattice relaxation. Thus far only spin-spin relaxation, summarized by the characteristic time  $T_2$ , has been discussed. Spin-spin relaxation is often dominated by local fluctuating fields dephasing individual spins on the millisecond timescale, making it a powerful handle for assessing molecular motion in relation to mobility and transport. Spin-lattice relaxation, summarized by the characteristic time  $T_1$ , involves a transfer of energy between spins and an energy reservoir or lattice. The transfer changes the spin state in the magnetic field. Thus, in high field NMR, fluctuating fields on shorter times scales, near the Larmour frequency, dominate relaxation. In solids,  $T_2$  is generally much shorter than  $T_1$  because motion is slower so anisotropic couplings dephase neighboring spins quickly. In liquids, these anisotropic couplings are averaged by molecular tumbling and  $T_2$  and  $T_1$  can be very similar.

Figure 3.11 shows the suite of  $T_1$ 's for the block copolymer/ionic liquid mixtures. The apparent trend is that the times decrease and are converging at high temperatures while becoming more disparate at lower temperatures. This seems most likely a consequence of the glass transition. At high thermal energy, motion is liberated for all the samples while lower temperatures display motional variance as some samples have more motional freedoms, which corresponds to different correlation times that govern relaxation. This thermal response Less mobile samples yield longer  $T_1$ 's and monotonically decrease with temperature, indicating that the minimum  $T_1$  at this field strength is somewhere above the experimental temperature range. Interestingly, the polymer washed with hydrochloric acid shows almost no temperature dependence, which demonstrates that the ionic nature of the pyridine ring and residual chloride ions strongly affects the freedom of motion and fundamentally alters the soft matter behavior of the organic polymer. One notable point to mention is that the  $T_1$  times for all of the protons were relatively equal with no particular moieties having much shorter or longer  $T_1$ 's. This is common for systems with abundant protons as spin-diffusion works quickly to distribute uneven magnetization.

Figure 3.12 displays the  $T_1$ 's for the homopolymer analogues of the block copolymer mixtures. The data look very similar to the diblock polymer data with a general trend of shorter  $T_1$ 's as temperature increases. It seemed plausible the presence of a sandwiching styrene phase could also affect  $T_1$  related motions as proposed for  $T_2$  motions, namely segmental motion. However, it seems that the  $T_1$  motions are perhaps less affected by the styrene phase. This is plausible because fluctuating fields on the Larmour

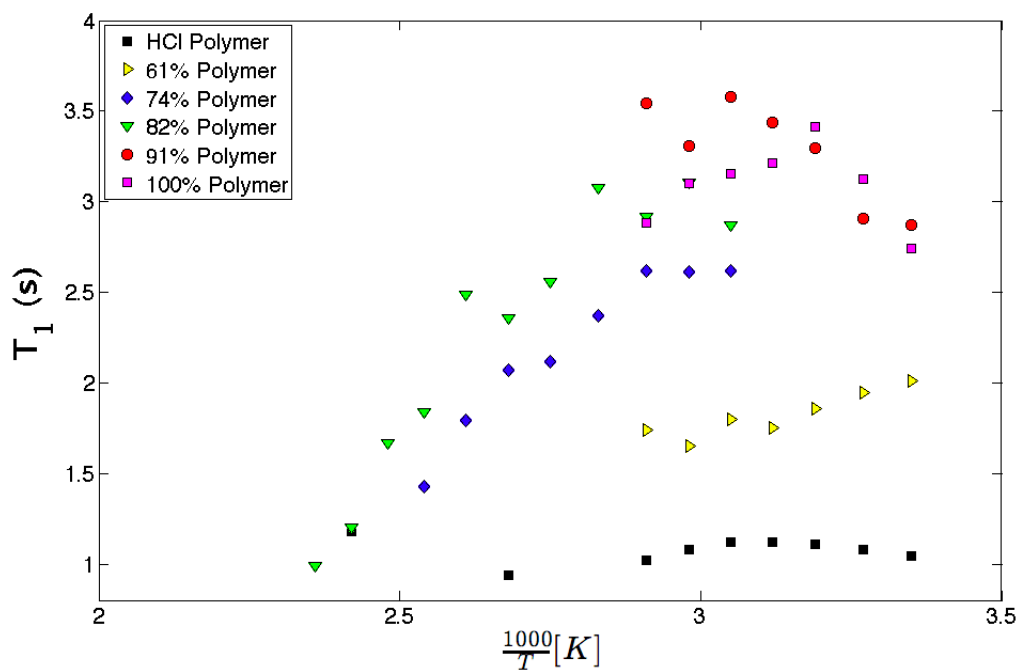


Figure 3.11: Average  $^1\text{H}$   $T_1$  times of S2VP/[Im][TSFI] vs. temperature

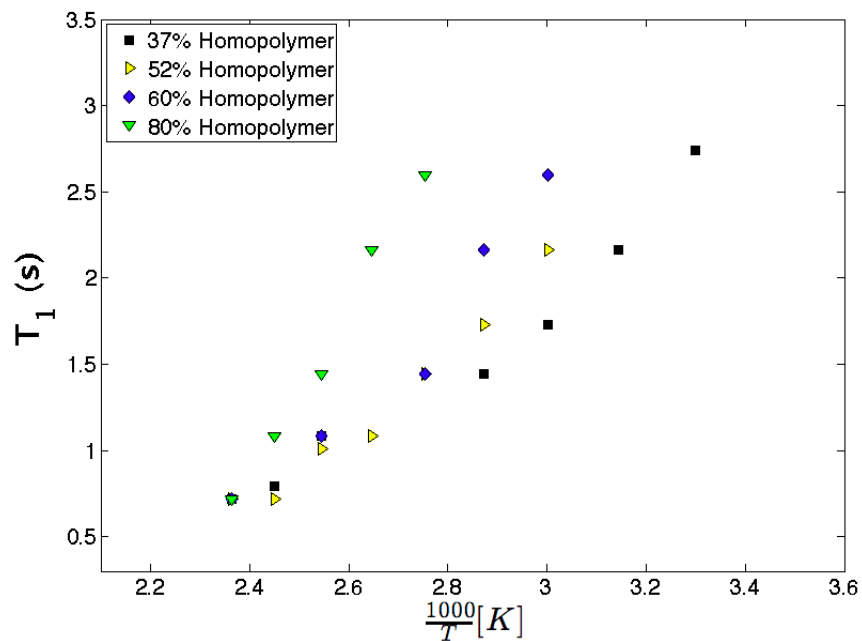


Figure 3.12: Average  $^1\text{H}$   $T_1$  times of P2VP/[Im][TSFI] vs. temperature

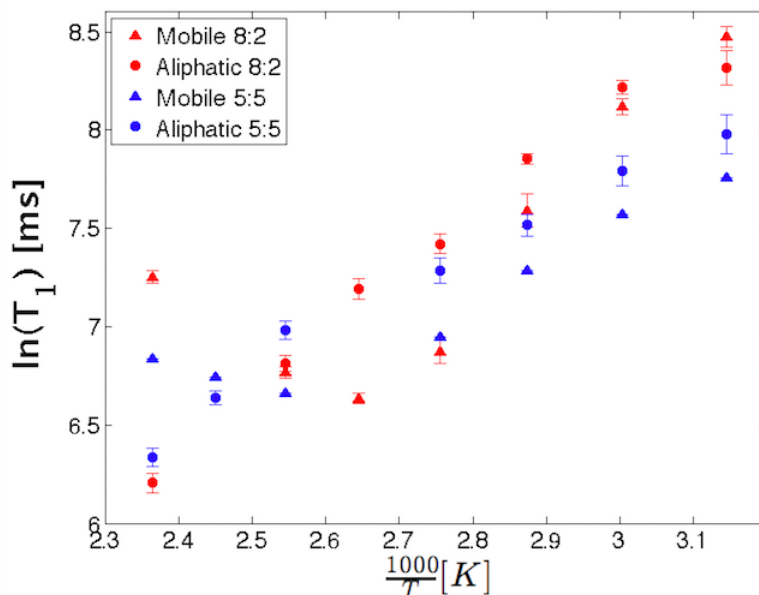
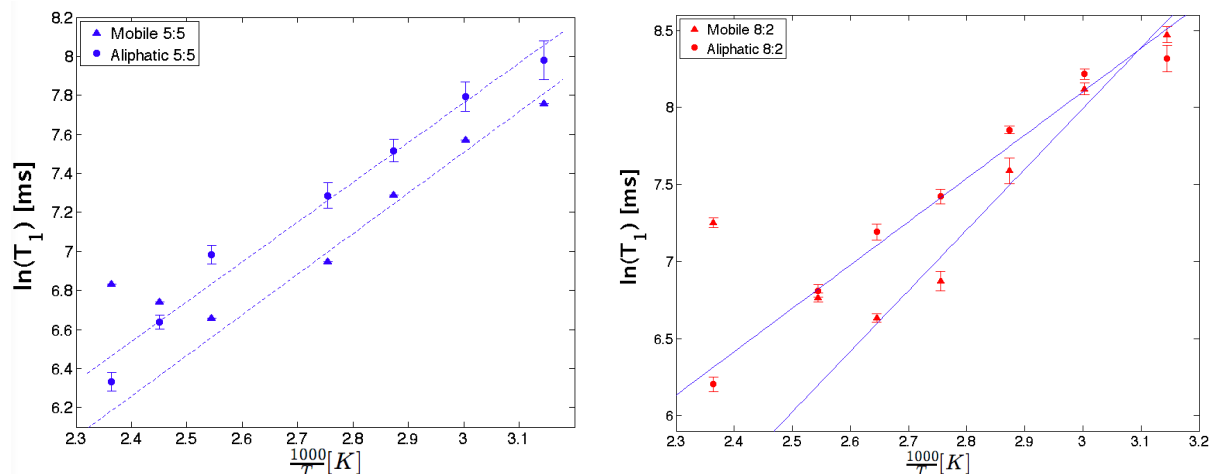


Figure 3.13: Site specific  $^1\text{H}$   $T_1$  times comparing 5:5 and 8:2 systems with similar ionic liquid loadings

timescale are expected to be much faster than segmental motion and more likely related to intramolecular motions such as bond vibrations and molecular rotations.

As mentioned previously, the proton  $T_1$  measurements for all the samples yielded generally homogenized relaxation times for all moieties. This means that the spin-lattice relaxation rate of the aliphatic backbone was similar to the aromatic polymer and also the protons of imidazole. However, protons in strong imidazole hydrogen bonds can exhibit very long  $T_1$ 's [17][27]. The most likely system to display long  $T_1$ 's due to hydrogen bonding is the non-symmetric ionic liquid, where neutral imidazoles are prevalent as hydrogen-bonding acceptor sites. Figure 3.13 displays the  $T_1$  data on a logarithmic scale for two specific spectroscopically discernible sites: the mobile proton of imidazole and the polymer backbone. The two samples being analyzed are the same as those in Figure 2.13 in which the ionic liquid concentrations are essentially the same but the ionic liquid composition is different. The 5:5 sample has more similar  $T_1$  times for the two proton types over the experimental temperature range. The asymmetric ionic liquid sample shows a greater difference in relaxation times between the two sites. The mobile protons for both samples actually seem to experience their minimum  $T_1$  value in the accessible temperature range, both around 100 °C. At low temperatures, the 8:2 sample shows a longer  $T_1$  even though the  $T_g$  of the samples are similar so mobility is not the ultimate factor. The same temperature analysis can be applied to  $T_1$  values as previously applied to  $T_2$ . Figure 3.14 shows the best linear fit to the relaxation times. The aliphatic data are fit over the entire temperature range whereas the mobile proton is fit only over the lower temperature regime to the right of the minimum point. Interestingly, the symmetric ionic liquid sample shows a



(a) Symmetric ionic liquid. The two proton types have nearly identical activation energies around 17 kJ/mol. (b) Asymmetric ionic liquid. The mobile protons have a higher activation energy around 33 kJ/mol while the aliphatic protons are about 22 kJ/mol.

Figure 3.14: Activation energies derived from spin-lattice relaxation times for two proton types

nearly identical activation energy for both protons. However, the asymmetric ionic liquid, with more hydrogen bonding partners, shows a much larger activation energy, even for the aliphatic moieties. Long  $T_1$ 's associated with strong hydrogen bonds implies that the motions that relax nuclei are not as efficient for these protons, meaning the timescales of the motions are shifted further from the timescales in relevance to the Larmour frequency. Interpreting the slopes as an energy barrier for a reaction (spin-state flip in this case), hydrogen-bonds seem to reduce the probability for these flips, resulting in longer  $T_1$ 's.

Spins exchanging between two environments with different  $T_1$ 's can have the two relaxation times averaged by the exchange [24]. These data were fit easily to a single exponential model which indicates that the populations of long  $T_1$  and short  $T_1$  populations are well mixed in the fast exchange regime. A biexponential model would suggest two distinct populations with the same chemical shift, contributing to two distinct  $T_1$ 's.

The fact that the 8:2 sample shows longer relaxation times is reasonable due to the myriad opportunities for hydrogen bonds between neutral imidazoles with longer  $T_1$ 's. Lower temperatures promote these bonds so the effect is amplified in this regime while lessened at higher temperatures. The hypothesis is that 8:2 systems somehow promote more "phase separation" between ionic liquid and polymer, such that spin-diffusion is not such a dominating force. There is more hydrogen bonding, stronger hydrogen bonding, and perhaps small pockets of neutral imidazole that are isolated from the polymer such that they can express longer  $T_1$ 's. Symmetric ionic liquids promote more uniform interaction between imidazole and the polymer such that  $T_1$ 's are homogenized.

### 3.5 Conclusions

The line narrowing phenomenon of the mobile, transferable proton in S2VP/[Im][TSFI] systems have been studied. The results showed that at lower temperatures, the line narrowing was described by an Arrhenius rate equation until segmental motion took over to yield a VTF model of activation. The nanostructured block copolymers did show this Arrhenius behavior somewhat above the glass transition temperature of the P2VP phase in which the mobile proton are imbibed. The suite of polymers displayed increasing larger activation energies as ionic liquid concentration was decreased. This is most likely a function of confinement, which reduces diffusion.

The same analysis was performed on the homopolymer analogues. Interestingly, the activation energy was not a strong function of concentration, and the temperatures wherein VTF behavior dominated were much cooler respective to  $T_g$ . The conclusion was that the confinement of the softer phase polymer in rigid lamella of polystyrene reduced the influence polymer segmental motions in certain temperature ranges. The homopolymers did not benefit from this luxury.

The data were then transformed into Eyring plots and extrapolated to  $1/T = 0$  to get a relative perspective on entropy. The diblock polymers showed that entropy of activation ( $\Delta\Delta S$  of proton hopping) increased as ionic liquid decreased. This is likely caused by shrinking lamellar domain sizes. Interesting, the homopolymers all had roughly the same entropy, giving evidence that confinement is the main culprit that affects entropy.

A non-symmetric 8:2 ionic liquid sample was compared. The data, when compared to the most analogous 5:5 sample, showed that the activation energy is significantly higher as well as the entropy of activation. A simple model of a more strongly hydrogen bonded network is proposed. Spin-lattice relaxation data were presented and discussed in terms of polymer mobility. The data seem to indicate that polymer motion as driven by temperature is the biggest factor in dictating  $T_1$ .

## Chapter 4

# Exchange and Diffusion in PFSA Membranes

### 4.1 Acknowledgement

The author gratefully acknowledges the contributions to this work from Kyle Clark, a material science researcher in the group of John Kerr at Lawrence Berkeley National Laboratory, and from Jay Yostanto, an undergraduate in Chemical and Biomolecular engineering at UC Berkeley.

### 4.2 Introduction

The standard membrane for polymer electrolyte fuel cells is Nafion, a commercially available perfluorinated sulfonic acid membrane. Its conductivity is high when fully hydrated. The reason for this is its morphological structure, wherein ionic channels, filled with strong sulfonic acid groups, weave and intertwine throughout a hydrophobic polymer. The phase separation gives the membrane mechanical strength, as the backbone chains are prone to crystallizing[28]. The ionic domains are hydrophilic and readily uptake water from the environment, solvating the acid groups. This ionic domain is conductive and, as more water is added to the membranes, the water channels swell, and the connectivity of the various water domains increases. However, because an aqueous phase shuttles protons, the membranes suffers a lack of selectivity for species that mix well with water. For this reason, in direct methanol fuel cells (DMFC), methanol crossover is a serious problem[29]. In Nafion, electroosmotic drag from ions will pull water and other small molecules along with them. For DMFCs, the crossover reduces the power density of the cell as also damages the membrane as it is susceptible to alcohols[30].

A common synthetic strategy to increase conduction and improve selectivity is to use filler materials that can block molecules other than protons as well as increase proton conduction at low hydration[3]. In this study, standard PFSA membranes, including some

Nafion-like material from the 3M corporation, were studied after modification with the additive 4(5)-(hydroxymethyl)imidazole. The amphoteric nature of imidazole makes it a good candidate for a proton conduction material. Of course, any additive must remain in the polymer, hence extensive synthetic routes are often taken to tether guest molecules to the polymer. In this study, the coulombic interaction with the polymer acid group is enough to tether imidazole in the membrane.

Measuring crossover of methanol can be done using an actual fuel cell and monitoring the reduction in power. For a more molecular understanding, we use pulsed field gradient (PFG) NMR to measure directly the self-diffusion of molecules. This has the advantage of focusing on the membrane material only, eliminating interfacial phenomenon such as electrode-polymer interfaces that might have unique methanol/water interactions. A good membrane will have high water diffusion rates and yet limit the diffusion of methanol. Measuring those two species simultaneously in the same membrane is an ideal situation and one potential advantage of using NMR.

This work was part of a team of collaborators, most of whom worked on fuel cells and membranes. The work presented here is focused on the NMR results with some insight on how it relates to the work by others.

### 4.3 Methods

Samples were prepared by Kyle Clark at LBNL. Hydroxymethyl imidazole (ImOH) was bought commercially and added to as-received Nafion by dissolving the desired amount of ImOH with the membrane in water overnight. TGA analysis was used to confirm the uptake of ImOH. Materials from 3M were also prepared in this way.

### 4.4 Results and Discussion

The proton environments inside PFSA membranes are of critical importance. One advantage of using NMR to study this material is that the backbone is completely per-fluorinated, meaning that  $^1\text{H}$  NMR is not convoluted by broad peaks from the partially crystallized backbone. In fact, the  $^1\text{H}$  NMR of Nafion contains a single sharp peak which comprises the lone proton from the acid group. Figure 4.6 shows the  $^1\text{H}$  MAS NMR spectrum of standard Nafion. A single peak connotes a single average chemical environment. The chemical shift between highly shifted acid protons and water protons demonstrates the fast mixing and chemical exchange to yield a shift that is the weighted average of these two extremes. Thus, the chemical shift moves as a function of hydration, expressing either more acid or water character. The presence of spinning sidebands insinuates that, even though the  $^1\text{H}$  peak is quite sharp, there are still anisotropies that are not completely averaged out by the internal motions. The spectrum of the modified membranes will become more complex as species with protons are incorporated into the membranes.



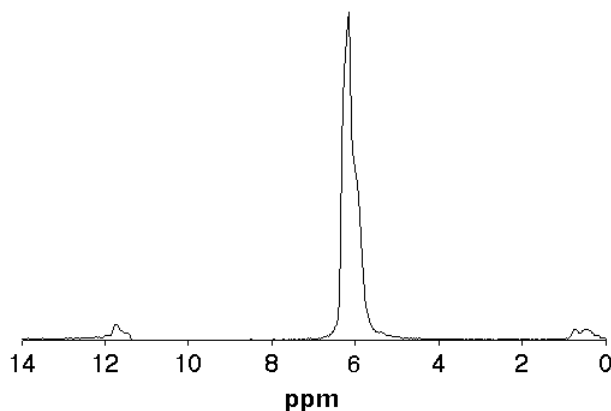


Figure 4.1:  $^1\text{H}$  MAS NMR spectrum of Nafion equilibrated at 50 °C and 25% RH. The MAS rate is 1.7 kHz which produces small spinning sidebands around 0 and 12 ppm.

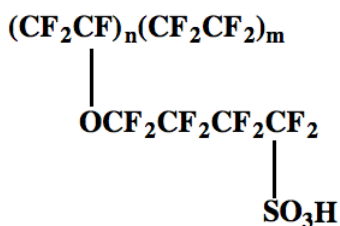


Figure 4.2: Chemical structure of 3M material

Distinguishing between exchanging water resonances and covalently bound protons on filler molecules will need to be carefully addressed.

#### 4.4.1 3M EW825

The structure of the 3M membrane is seen in Figure 4.2. The ionomer features a short, linear sidechain with no branch points, which differs from other PFSA ionomers such as Nafion. The advantage is higher crystallinity and modulus with a lower equivalent weight to achieve higher conductivity. Equivalent weight (EW) is defined as the weight, in grams, of dry polymer per mole of sulfonic acid groups. Higher EW means a lower concentration of acid group, reducing conductivity. However, too low an EW results in lack of structure and membrane integrity.

The membrane in this study is 825 EW material. Incorporated into the membrane are different concentrations of 4(5)-(hydroxymethyl)imidazole, whose structure is seen in Figure 4.3. The critical question is how the incorporation of the imidazole helps improve the properties of the membrane and insights into the molecular mechanisms by which these changes occur.

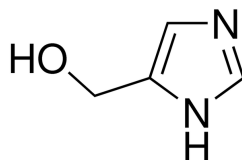


Figure 4.3: Chemical structure of 4(5)-(hydroxymethyl)imidazole

#### 4.4.1.1 Full ImOH Incorporation

Based on the EW, the number of acid groups in the material is readily calculated if you know the material mass. As an extreme, ImOH was added to a solution of the material in slight excess in order to introduce at least one ImOH unit for every acid group. Then this material was processed in the usual manner to obtain at 100% imidazole-incorporated membrane. How these filler molecules imbibe themselves within the membrane is the question. ImOH has a proton acceptor site on the ring nitrogen, and a strong acid will readily donate a proton to it. Will this reduce the affinity of the membrane to soak up water? To understand this,  $^1\text{H}$  NMR was employed.

Figure 4.4 shows the variable temperature  $^1\text{H}$  MAS NMR spectrum of this material. At high temperature, four peaks are seen, the most downfield peak having a larger linewidth. As temperature is lowered, the three upfield peaks broaden, and their chemical shift remains roughly the same. However, the broad downfield peaks shows unusual behavior. Lowering the temperature, the peak becomes broader until about 60 °C, then moves downfield, and actually becomes slightly sharper just below 60 °C. The peak continues to move downfield, maintaining a distinct lineshape even at extremely cold temperatures. Notice that the other peaks are highly affected by the temperature approaching -45 °C.

The three upfield peaks are easily confirmed as the two C-H peaks on the imidazole molecule, which are aromatic, and the  $\text{CH}_2$  peak of the HO-imidazole linking carbon. A 1:1:2 intensity ratio is easily seen. The downfield peak displays classic chemical exchange behavior, coalescing around 60 °C. This means that below the coalescence temperature, another peak is present. This other peak must be upfield, as the two partner peaks move toward each other and combine at coalescence to become one. In order to quantify this process, all the peaks must be deconvolved into their separate contributions.

Figure 4.5 shows the deconvolution of the peaks at every temperature. The red curve is the sum of fitting two exchanging peaks. The blue shows the sum of the three ImOH peaks that do not exchange. Adding the blue and red lines gives the total fit. There are two distinct red peaks below 60 °C. At 60 °C, coalescence has not fully occurred, as seen in the slight deformation of the peak. Above this temperature, the peaks take on the familiar Lorentzian lineshape. An interesting behavior was that at the very low -45 °C, the peaks remain relatively sharp, except the  $\text{CH}_2$  peak at 4 ppm which was very broad in the fit. This could imply that while motion in general is arrested, the imidazole ring maintains unique modes of motion, possibly a ring flip.

An important point about this fit is that the population contributions were fixed while

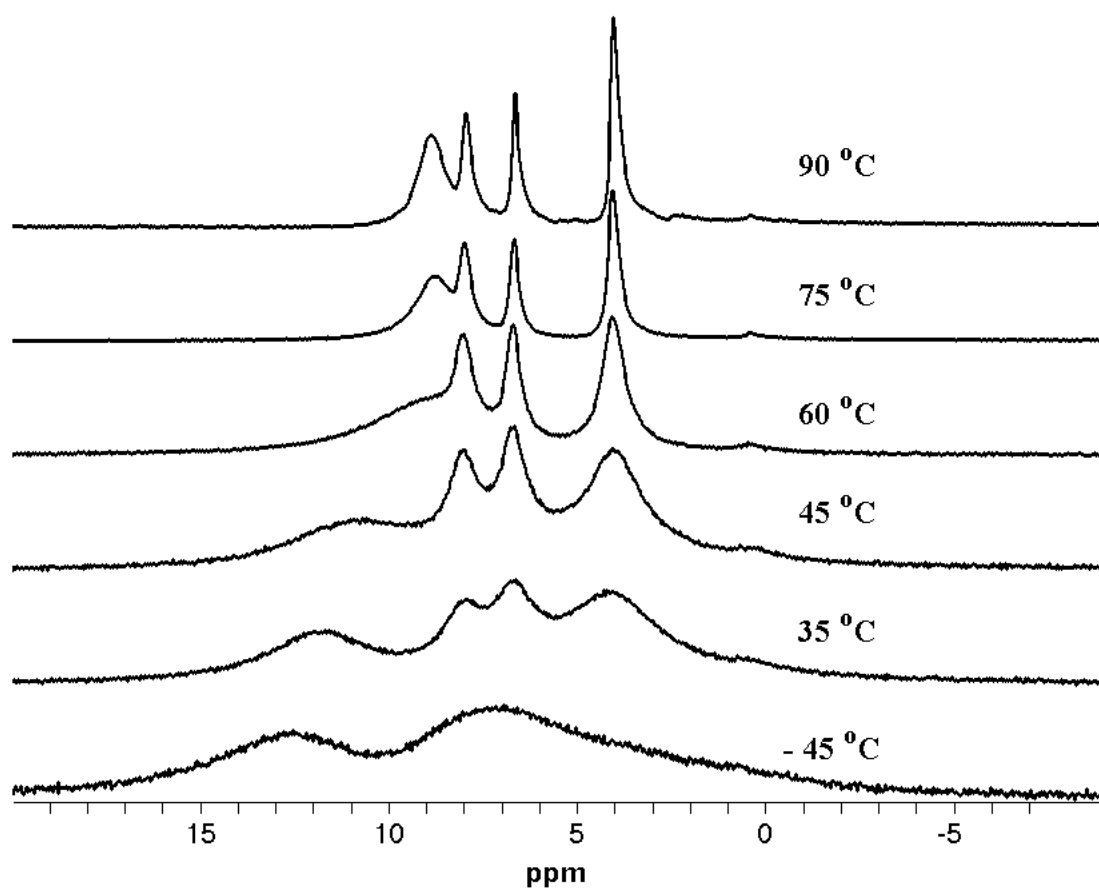


Figure 4.4: Variable temperature  $^1\text{H}$  MAS NMR of 3M 825 with 100% 4(5)-(hydroxymethyl)imidazole saturation. MAS rate is 15 kHz.

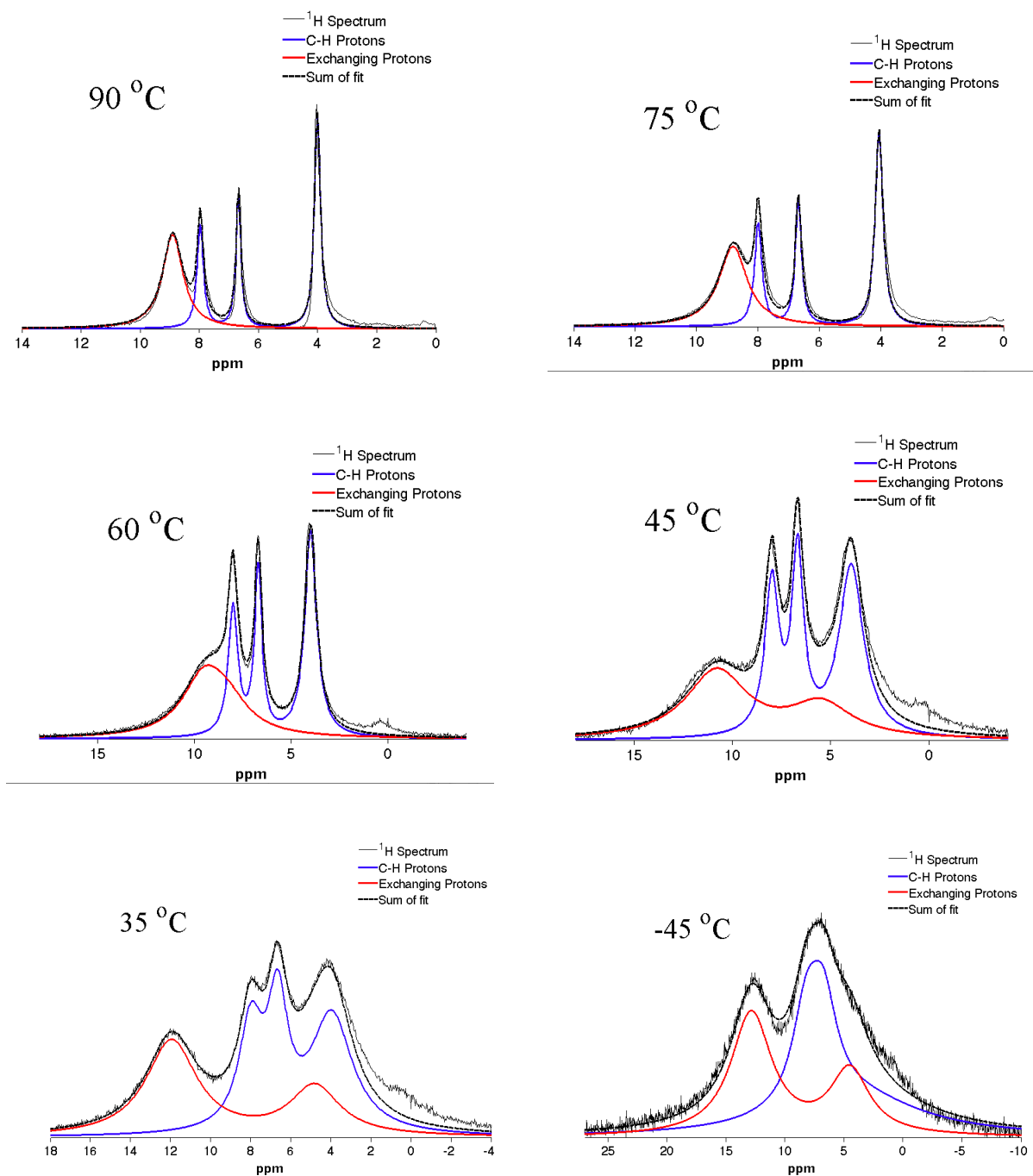


Figure 4.5: Peak deconvolution of  $^1\text{H}$  MAS NMR of 3M 825 with 100% 4(5)-(hydroxymethyl)imidazole saturation at each temperature. MAS rate is 15 kHz. The red line is the sum of the exchanging protons. The blue peak is the sum of the covalently bound C-H proton on imidazole. The dotted black line is the sum of the blue and red line. Note the expanded ppm scale for the -45 °C spectrum.

only lineshapes and chemical shifts were set as free variables. The populations were based on the 90 °C fit which very nicely showed that the broad downfield shift contributed a  $\frac{3}{7}$  fraction to the overall integration. The two aromatic imidazole peaks yielded  $\frac{1}{7}$  each and the CH<sub>2</sub> peak accounted for the last  $\frac{2}{7}$ . When adding ImOH to the ionomer, there are 6 protons added to the one native -SO<sub>3</sub>H proton for a total of 7. This implies that the three protons involved in the exchange process are the hydroxyl proton, the N-H proton and the -SO<sub>3</sub>H proton. Furthermore, when separated into two distinct peaks, the exchanging peaks existed in a 2:1 ratio.

The chemical shift difference between the two imidazole aromatic C-H peaks is about 1.3 ppm, which is characteristic of a protonated imidazole ring. Neutral imidazole would display a difference closer to or less than 1 ppm. In fact, liquid <sup>1</sup>H NMR spectrum of 4(5)-(hydroxymethyl)imidazole dissolved in 90% D<sub>2</sub>O showed the apical and basal peaks at 7.57 ppm and 6.96 ppm, respectively (data not shown). This is to be expected since such a strong acid is in the material. However, even with such one-sided proton transfer, exchange behavior is present. The exact nature of the exchange behavior is difficult to assess. The  $\frac{2}{7}$  by population downfield exchanging peak would seem to be the protonated N-H sites. Technically, these two sites are not equivalent, but the difference is subtle and unable to be detected in the solid state. The other exchanging peak ( $\frac{1}{7}$  by population) is consistent with hydroxyl proton chemical shifts, but this assignment is not certain because hydroxyl shifts are very sensitive to their solvent environment. One thing that should be noted is that the -45 °C static downfield chemical shift is only 12.8 ppm, which suggests this is not a hydrogen bond between imidazole groups, as they show much larger chemical shifts near 14 - 16 ppm. Most likely, due to the coulombic forces that would keep cationic imidazole near the anionic acid, this is an interaction between the acid oxygens and the imidazole protons. How the hydroxyl protons play a role is uncertain.

The coalescence phenomenon can be seen by plotting the chemical shifts of the downfield protons with temperature. This is seen in Figure 4.6. There is a dramatic inflection point in the shift near 60 °C when the rate of chemical process becomes equal to the difference in the NMR frequency between the two sites. The inverse linewidth also shows this behavior, as seen in Figure 4.7. The slight dip in the linewidth at the coalescence point is a real phenomenon wherein the linewidth becomes larger before narrowing as temperature increases. In addition, the lineshape is not a strong function of temperature below 60 °C. The activation energy for local proton mobility is 37 kJ/mol in the fast-exchange limit. This number is about 2.5 times higher than values typical for these materials without modification[3].

The spectra in Figure 4.5 account for all the protons without the inclusion of any foreign water. The main conductive pathways in these PFSA materials are the water domains that show a strong, positive correlation between hydration and conductivity. This might explain why the activation energy for the exchangeable proton is so high. To understand how modification affects water uptake, Figure 4.8 shows the dynamic vapor sorption (DVS) data for the water uptake of these modified membranes. The trend is clear that incorporation of ImOH reduces the natural water uptake from the environment

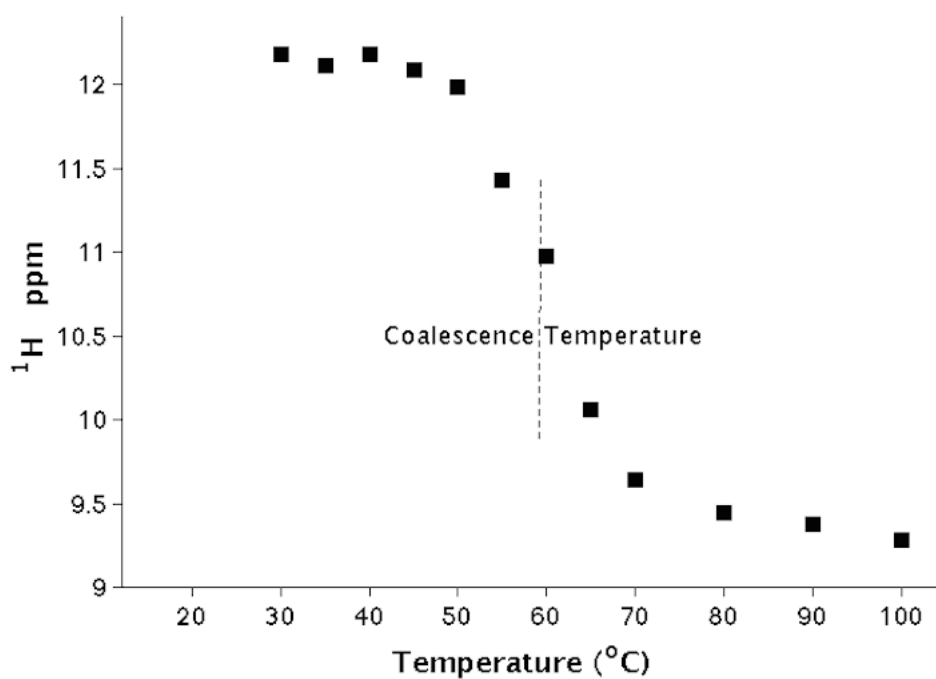


Figure 4.6:  $^1\text{H}$  chemical shift of downfield, exchangeable proton vs. temperature

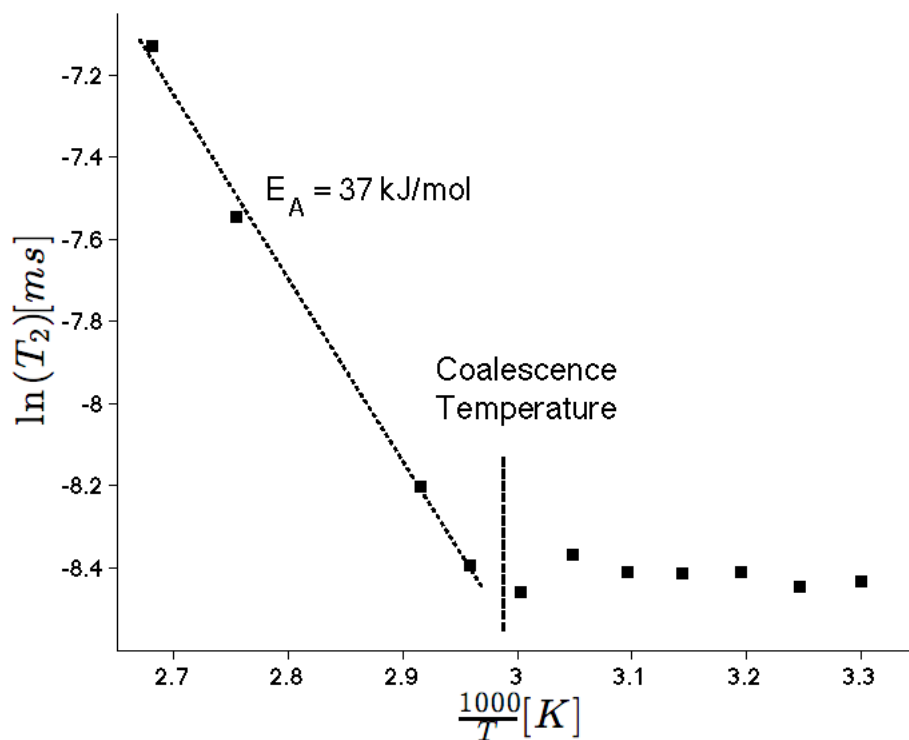


Figure 4.7: Temperature-dependent transverse relaxation time of exchanging proton

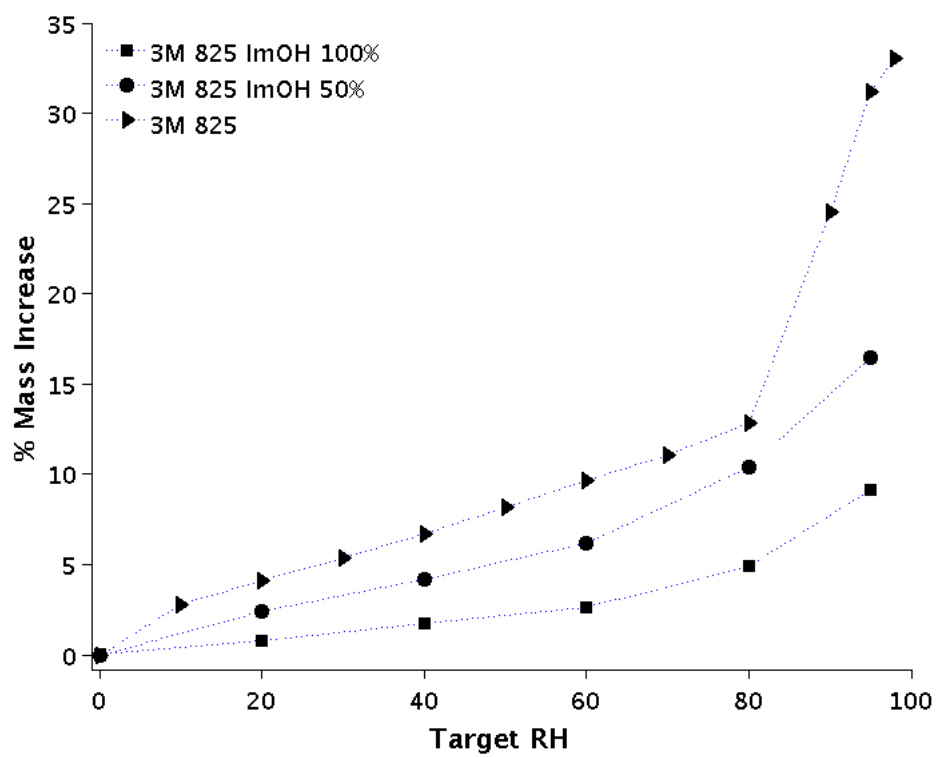


Figure 4.8: Dynamic vapor sorption of 3M 825 EW membranes with ImOH at 50 °C.  
*Data courtesy of Kyle Clark.*

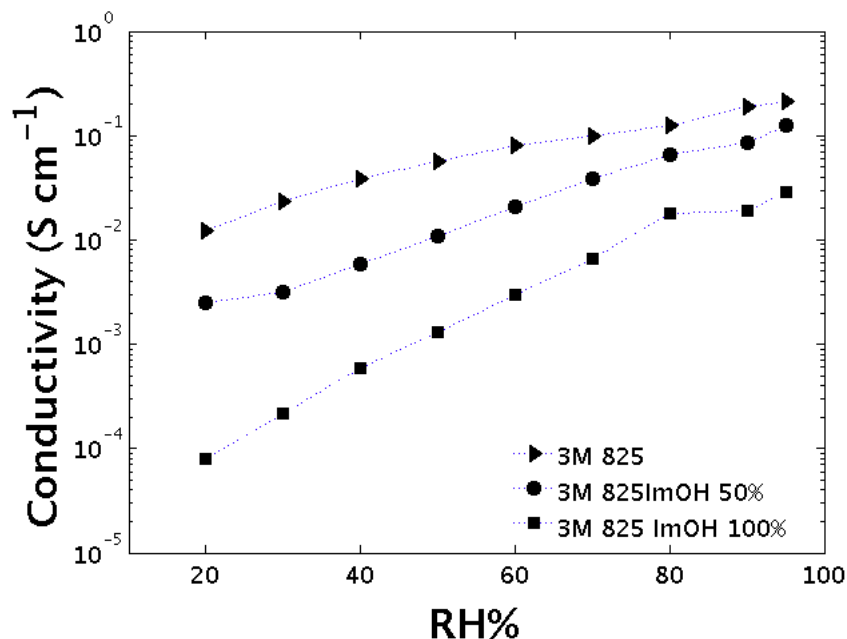


Figure 4.9: Conductivity vs. relative humidity of 3M 825 EW membranes with ImOH at 80 °C. *Data courtesy of Kyle Clark.*

compared to unmodified membranes. 50% ImOH simply means that only half of the full ImOH capacity (one ImOH per sulfonic acid group) is added to the dispersion when making the membrane. To see the effect on conductivity, which usually scales directly with hydration, Figure 4.9 shows how incorporation of ImOH has a negative effect on conductivity.

#### 4.4.1.2 Half ImOH Incorporation

The decrease in conductivity was most severe with the addition of a 1:1 equivalent of ImOH. However, adding only half produced results which were less severely skewed. <sup>1</sup>H NMR experiments were performed for this situation to assess the proton environments. Figure 4.10 shows the variable temperature <sup>1</sup>H MAS NMR experiments for the 50% ImOH sample. At first glance, these spectra are remarkably different from Figure 4.4. The central peak around 7.0 ppm dominates the spectrum. This peak has been assigned to proton in fast exchange between acid and free water. This is typical of standard membranes as seen in Figure 4.1. The peak at around 4.0 ppm is once again the CH<sub>2</sub> protons on the OH-imidazole linker carbon. The downfield shift around 12.0 ppm is no longer temperature dependent and appears as two peaks at higher temperature. This is most likely the two N-H protons on the imidazole which are nonequivalent due to the lack of symmetry of the imidazole. This is further confirmed by the fact that the peak at 12 ppm and 4 ppm have equal intensities. The other C-H imidazole peaks can be accounted



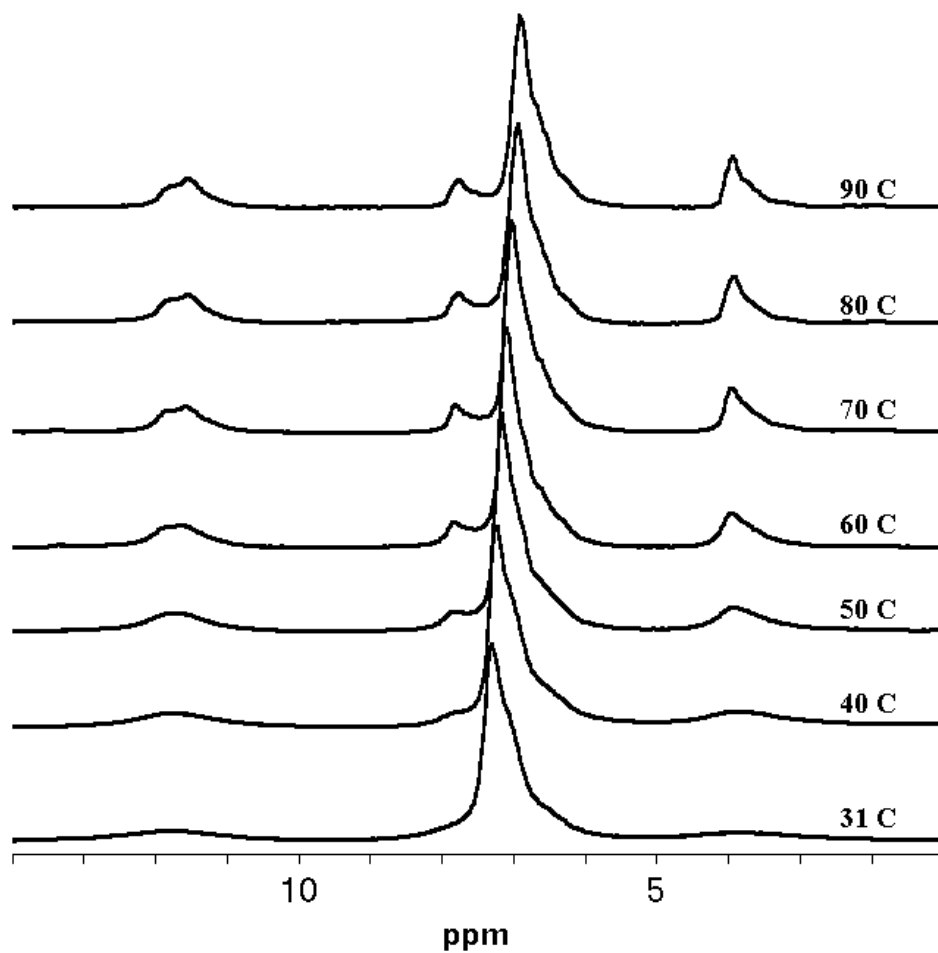


Figure 4.10: Variable temperature  $^1\text{H}$  MAS NMR of 3M 825 with 50% 4(5)-(hydroxymethyl)imidazole saturation. MAS rate is 15 kHz. The membrane was stored in laboratory conditions (i.e. ambient humidity).

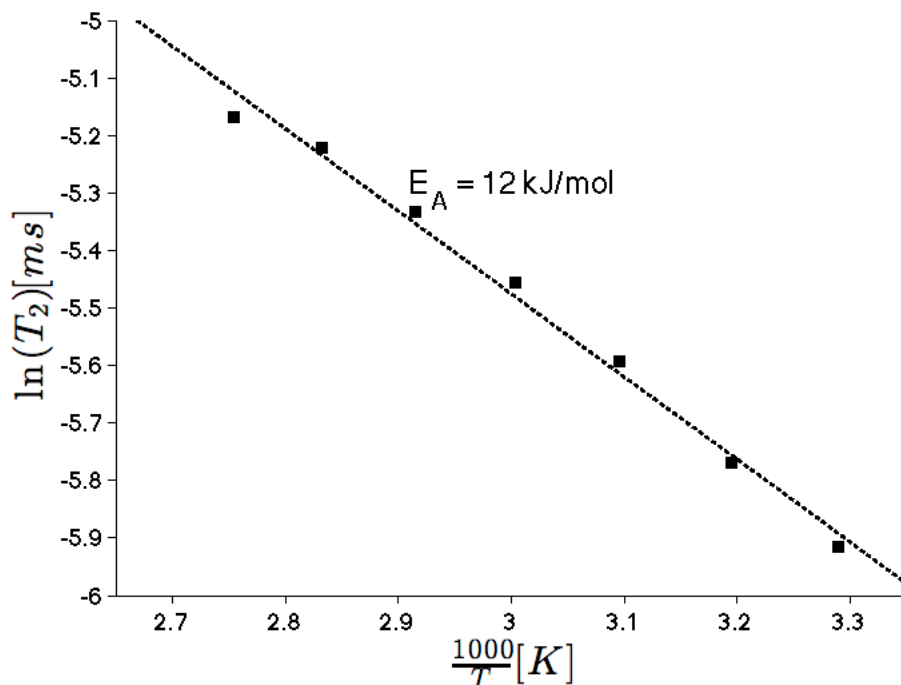


Figure 4.11: Temperature-dependent transverse relaxation time of fast exchanging protons

for in the aromatic region where the peak around 6.7 ppm appears as a shoulder of the water peak in these spectra.

The same linewidth analysis as in Figure 4.7 is not possible because the exchange behavior is not occurring between ImOH protons. However, the large proton signal from imbibed water does exhibit line narrowing characteristics. Figure 4.11 shows that the fast-exchange behavior exists over the whole experimental temperature range. In addition, the activation energy of 12 kJ/mol is typical of PFSA membranes. However, the conductivity is significantly reduced despite the high local proton mobility. One possible explanation is that the lower water uptake reduces the ionic channel size and connectivity throughout the membrane, affecting the macroscopic conductivity measurements.

#### 4.4.1.3 $^1\text{H}$ - $^{13}\text{C}$ CPMAS NMR

To confirm the protonation state of the imidazole ring,  $^{13}\text{C}$  NMR was used as the chemical shifts of the carbons in the ring are very sensitive to pH, as seen in biological histidine[31]. To understand the changes that occur when adding ImOH to the acid membrane, simple experiments were first performed on the precursor molecule ImOH. Figure 4.12 shows the  $^{13}\text{C}$  CP/MAS spectrum. As a test to confirm carbon-proton connectivities, the decoupler is turned off briefly during the acquisition of the spectrum in Figure 4.12b. Only the peak at 140 ppm survives, which means this peak originates from the only proton-less carbon ( $\gamma$ -carbon) in Figure 4.3. The lack of directly bound protons also

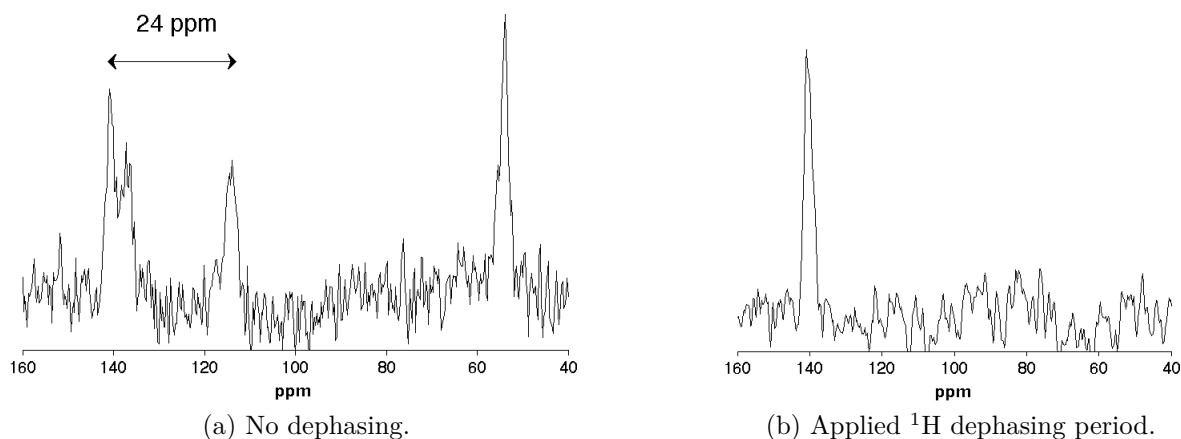


Figure 4.12:  $^{13}\text{C}$  CP/MAS spectrum of 4(5)-(hydroxymethyl)imidazole

explains the sharp nature of this peak. Figure 4.12a shows the normal spectrum with three carbons in the aromatic region and the  $\text{CH}_2$  upfield carbon.

Once ImOH has been imbibed in an acid membrane, its structure and protonation state are likely to change. Figure 4.13 shows  $^{13}\text{C}$  CP/MAS spectrum for ImOH in a membrane. Only two aromatic carbon resonances are seen. The upfield  $\text{CH}_2$  peak has not shifted. However, the two visible aromatic peaks have shifted closer together. This is characteristic of protonation of the ring. Under full protonation the  $\gamma$ -carbon with no proton lies almost midway between the other carbon chemical shifts. The peak at 135 ppm is consistent with the apex carbon of imidazole, and the peak at 118 is consistent with basal carbon. However, under no conditions was the  $\gamma$ -carbon able to be seen. Increasing the cross-polarization contact time did not reveal the  $\gamma$ -carbon; the other signals reduced heavily before the  $\gamma$ -carbon was seen due to proton relaxation in the rotating frame,  $T_{1\rho}$ . Using a proton dephasing acquisition scheme, as in Figure 4.12b, also did not yield the hidden carbon. In general, this scheme reduced the intensity of all the peaks equally. It seems likely that the natural motion of the molecule reduces the cross-polarization efficiency to that proton-less carbon while not totally attenuating the efficiency to polarize directly bound carbons. The same results occurred for the 50% ImOH membrane as seen in Figure 4.14. The peaks have the exact same chemical shift as before, but are slightly narrower. This implies more motion of ImOH in the 50% sample, which is consistent with more hydration.

One problem with the CP/MAS method is that it favors static molecules and possibly filters out mobile ones[32]. The previous  $^1\text{H}$  experiments have all revealed exchange in the fast limit of protons, but these carbon chemical shifts are consistent only with static, protonated imidazole rings. To investigate this, direct detection experiments were employed. Figure 4.15 shows the directly detected carbon spectrum of 3M EW825 with

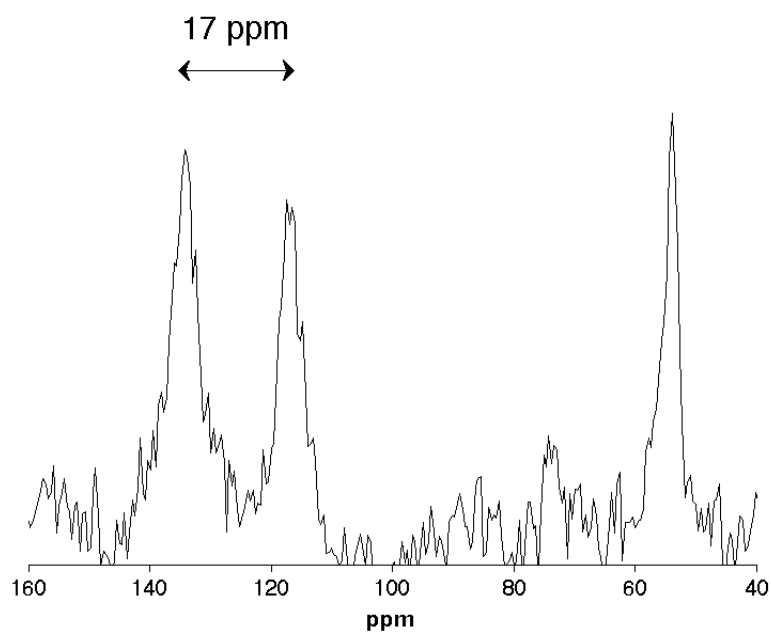


Figure 4.13:  $^{13}\text{C}$  CP/MAS spectrum of 3M EW825 with 100% ImOH addition. The contact time is 1 millisecond.

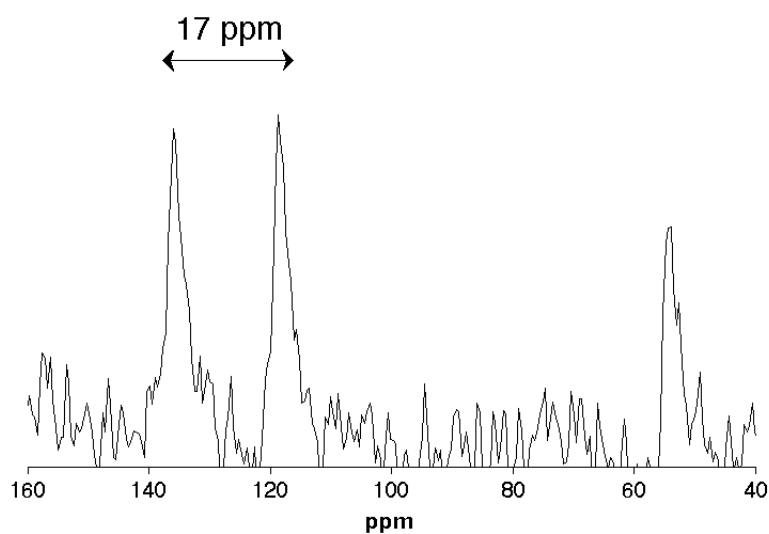


Figure 4.14:  $^{13}\text{C}$  CP/MAS spectrum of 3M EW825 with 50% ImOH addition. The contact time was 1 millisecond.

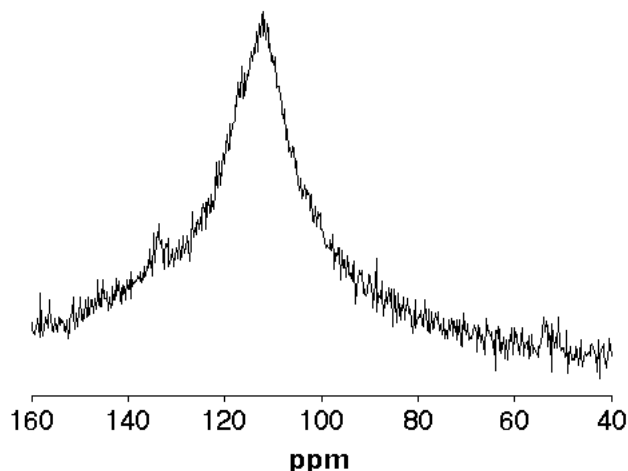


Figure 4.15:  $^{13}\text{C}$  direct detection spectrum of 3M EW825 with 100% ImOH addition

| Material         | Experiment       | $\gamma$ -carbon | Apex carbon | Basal carbon |
|------------------|------------------|------------------|-------------|--------------|
| ImOH powder      | CP/MAS           | 140              | 136         | 112          |
| 3M 825 100% ImOH | CP/MAS           | N/A              | 134         | 117          |
| 3M 825 100% ImOH | Direct Detection | N/A              | 132         | 112          |
| 3M 825 50% ImOH  | CP/MAS           | N/A              | 134         | 117          |
| 3M 825 50% ImOH  | Direct Detection | N/A              | 132         | 112          |

Table 4.1: List of carbon chemical shifts (ppm) for ImOH

100% ImOH addition. The advantage of the CP/MAS experiment is immediately clear in that it eliminates the carbon backbone of the polymer. However, the peak at around 135 ppm and 55 ppm are still visible. To help things even further, the free induction decay can be clipped such that only narrow resonances remain. This is a common spectral editing technique. The result of this is shown in Figure 4.16. The signal-to-noise ratio is low because editing the spectrum throws out data from all the peaks. Comparing this spectrum to Figure 4.13, the shifts of the aromatic carbons are slightly different. Table 4.1 list the chemical shifts of the imidazole ring for the various samples using different NMR techniques. It is clear that the two experiments are filtering two different types of imidazoles. The CP/MAS experiment relies on the  $^1\text{H}$ - $^{13}\text{C}$  dipolar coupling to transfer magnetization from protons to carbon. If the molecule moves too fast, this coupling can average to zero and cross-polarization yields very little signal. Therefore, the spectral features of the cross-polarization experiments are assigned to imidazoles with limited motion, not undergoing relatively fast isotropic motions. It is unusual that the  $\gamma$ -carbon is absent from the spectrum and could not be found under any reasonable experimental

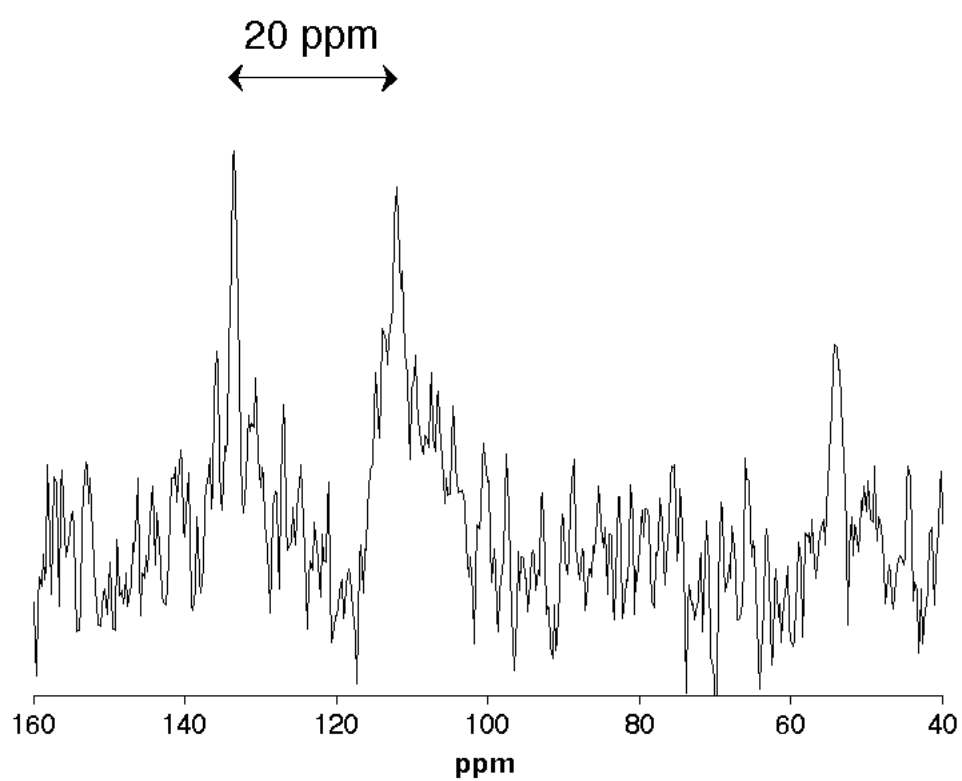


Figure 4.16: Spectrally edited  $^{13}\text{C}$  direct detection spectrum of 3M EW825 with 100% ImOH addition. The broad polymer peak has been eliminated.

conditions. The 17 ppm difference between the other two carbon is indicative of a static, cationic state of the imidazole. The conclusion is that the motional rate is in some regime where cross-polarization is possible for carbons with protons attached but difficult for carbons that are not protonated.

The directly detected experiment accounts for all carbons, except that those with longer spin-lattice relaxation times will be possibly filtered out. Since these materials are not isotopically enriched,  $T_1$  differences between sites are reasonable as spin-diffusion, which would homogenize  $T_1$ 's, requires spins to be highly abundant.

The fast moving imidazole  $^{13}\text{C}$  resonances will appear at their average frequency in the fast exchange limit. It is curious that the apex proton appears at a lower chemical shift for the direct detection experiments because the protonated state should be the largest upfield shift for that carbon, which was assumed to be 134 ppm from the CP/MAS experiment (static, protonated imidazole). A fast exchanging imidazole would be assumed to express shifts somewhere between neutral and protonated.

The larger point is that the system displays a dynamic picture which seems to point to some protonated imidazoles that are static on the NMR timescale. These are probably experiencing strong, coulombic effects which keep them from leaving the membrane during fuel cell operation. However, there is also a significant population showing exchange as evidenced in the  $^1\text{H}$  NMR. This exchange could be with water or even intramolecular exchange between hydroxyl and N-H protons.

## 4.5 $^{19}\text{F}$ NMR

To investigate how the addition of 4(5)-(hydroxymethyl)imidazole possibly affects the chemistry of the polymer,  $^{19}\text{F}$  NMR was performed on the dispersions of the polymer membranes. The point of interest was observing the shift for the fluorine adjacent to the sulfur to check for the possible formation of esters. Fluorine has a very sensitive chemical shift, and the formation of esters is known to have a discernible effect even though the sulfonate is where the chemistry is occurring. Figure 4.17 shows the spectra of a normal sample of 3M EW825 dispersed in methanol and a sample made by dissolving a 100% substituted membrane in methanol. The NMR was performed at 376 MHz using a 4 mm NMR tube.

The shift of interest is around -116 ppm. The figure shows that all of the shifts are unchanged. The conclusion to draw from this is that 4(5)-(hydroxymethyl)imidazole does not form covalent bonds with the sulfonate group, and the chemical state of the sulfonic acid is the same in both samples. Identical results were seen for 50% substituted samples.

## 4.6 Self-Diffusion

The ideal PEM membrane would have high selectivity towards protons and block other species. The mobility of various species in the material is the metric of interest when

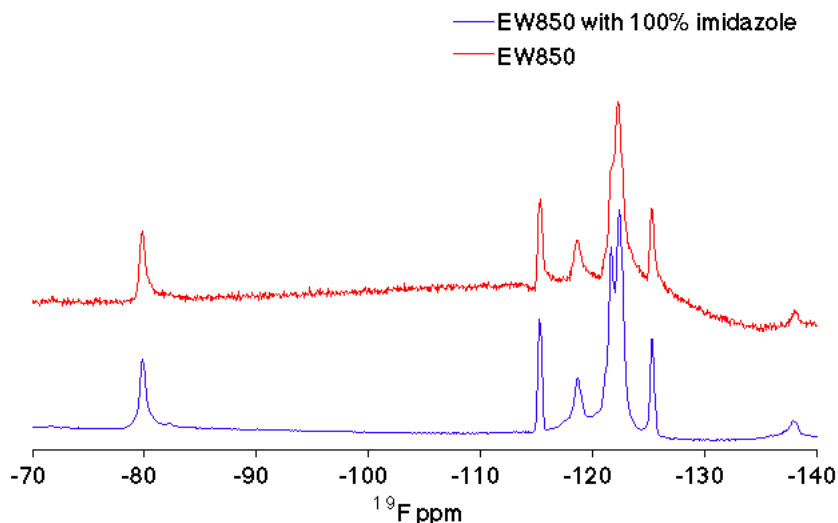


Figure 4.17:  $^{19}\text{F}$  NMR of dispersions of 3M EW850 in MeOH

assessing which species will pass through. Field gradient NMR diffusometry is a powerful NMR method to measure self-diffusion. This study used standard pulsed field gradient (PFG) NMR to discern the relative mobilities of methanol and water in commercial and modified membranes.

#### 4.6.1 Pulse Sequence

A standard spin echo pulse sequence is used with the addition of a uniform gradient which is generated across the sample. This pulse, which is generated by an external DC amplifier, encodes the spins of the sample with a phase which is a function of position. The spins then diffuse due to their natural motion, and then a second gradient pulse which reverses that encoded phase is applied. Spins which do not move will see no effect from the gradient pulses. However, spins which move about will not be efficiently refocused by the second gradient pulse because they have moved. To account for natural decoherence from relaxation during the pulse sequence, the intensities are normalized to an initial spin echo with no gradient applied [33].

Figure 4.18 shows the basic pulse sequence for measuring diffusion. Practically, the strength of the pulse gradient increases throughout the experiment while all other parameters remain constant. The data are then fit to the following equation first derived by Stejskal and Tanner [34]

$$\ln \frac{A(2\tau)}{A(0)} = -D\gamma^2\delta^2\left(\Delta - \frac{1}{3}\delta\right)g^2$$

where  $A$  is the intensity of the echo,  $D$  is the diffusion coefficient,  $\gamma$  is the magnetogyric ratio of the nuclei,  $\delta$  is duration of the gradient pulse,  $\Delta$  is the spacing between the two



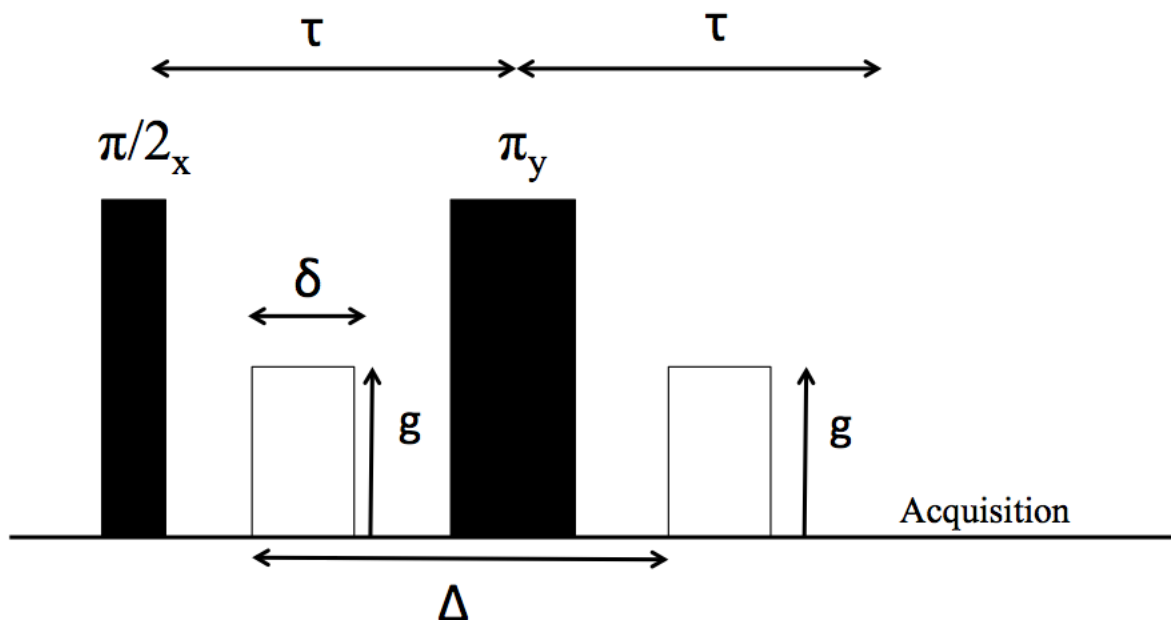


Figure 4.18: The Stejskal and Tanner pulsed-field gradient NMR sequence

gradient pulses, and  $g$  is the gradient strength. The gradient strength generated at the sample of a probe is dependent on the geometry of the coil and amperage running through it. Generally, this is not calculated but rather more easily determined using a calibration with a sample with known diffusion coefficient.

#### 4.6.2 Experimental

PFG NMR experiments were performed using a commercial Doty PFG probe. Variable temperature experiments were performed using an external Doty temperature controller that was calibrated by the chemical shift difference in a glycerol spectrum. Figure 4.19 shows the gradient calibration using water. Once the gradient is known, all other experiments can be evaluated to determine self-diffusion coefficients for water and methanol in the membrane.

The membranes for the PFG experiments were Nafion 212, similar to the 3M material. It has a slightly different polymer structure but still comprises a phase separated matrix of hydrophobic polymer and hydrophilic channels with sulfonic acid moieties. In solution, methanol and water are resolvable in NMR spectra. However, in membranes, the line-shapes broaden and begin to overlap. For this reason, methanol diffusion was measured using deuterated water in the solution.

The goal of the study was to determine how modifying membranes with imidazole improved selectivity over methanol transport. Commercial Nafion was prepared by boiling the membrane in distilled water for 1 hour and then the membranes were allowed to dry.

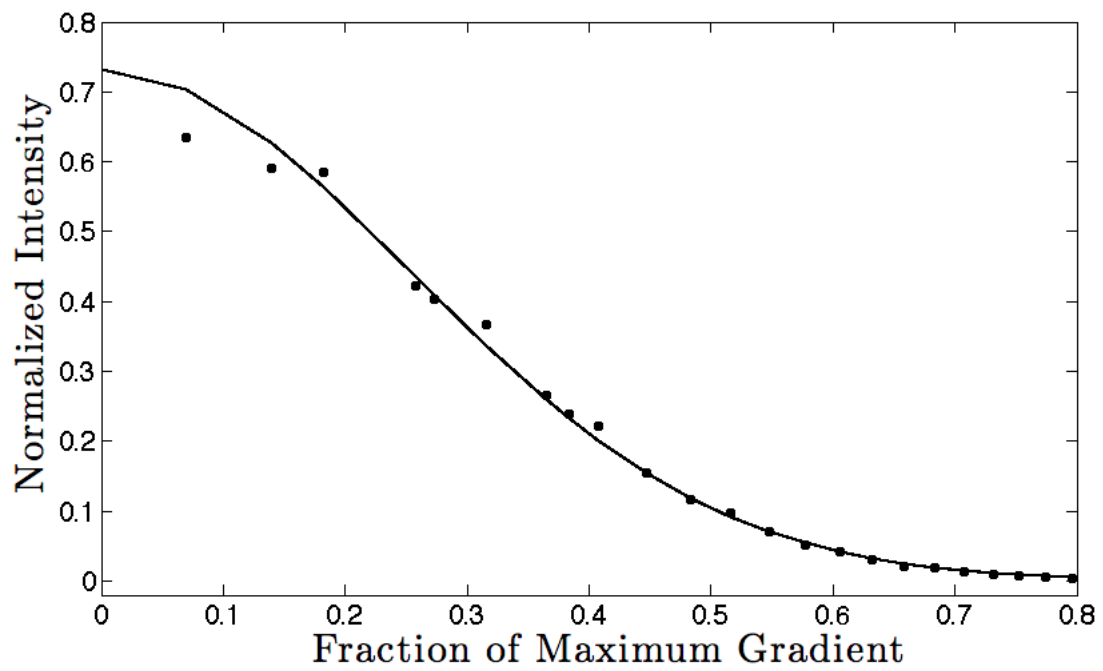


Figure 4.19: Field gradient strength calibration of water at 30°C. The intensities are normalized to the first echo and then fit to the Stejskal and Tanner equation. The gradient at full strength is 2.4 Tesla/meter.

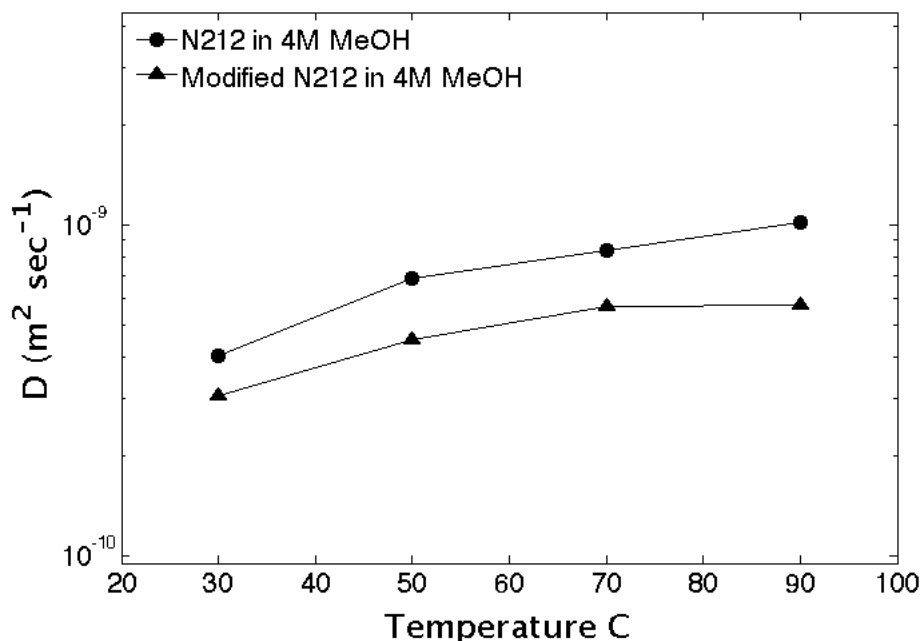


Figure 4.20: Comparison of proton diffusion in standard Nafion and modified Nafion. The majority of the signal is from water protons in the solution.

Next they were cut into 1x1 cm squares and put into 4M methanol solutions with either water or deuterated water. The same was done for a modified Nafion membrane with 50% imidazole substitution. A fully substituted membrane was not studied due to overall poor conductivity results, which was likely due to lack of water uptake in general. A single, broad echo was seen for all experiments. It was assumed that the water dominated the signal for the 4M methanol solution with normal water because the water concentration is about 50 molar.

After soaking in solution for 24 hours, the samples were quickly removed, wiped clean of excess solution on the surfaces and placed at the bottom of 5mm NMR tubes. Three teflon spacers, wrapped in Teflon tape, were put in the tube and pushed all the way down to reduce dead volume near the sample. The tube was put into the probe and magnet, and experiments were run at variable temperatures, waiting 10 minutes to equilibrate at new temperatures.

### 4.6.3 Results

Figure 4.20 shows the diffusion coefficients for protons in Nafion equilibrated in a 4M methanol solution. This is not the same as the diffusion coefficient of water because protons hop between water molecules and acid groups via a Grotthus mechanism as well as moving via a vehicle mechanism on water molecules. Modification with imidazole reduces the diffusion consistently at all temperatures but not significantly. This is promising as a

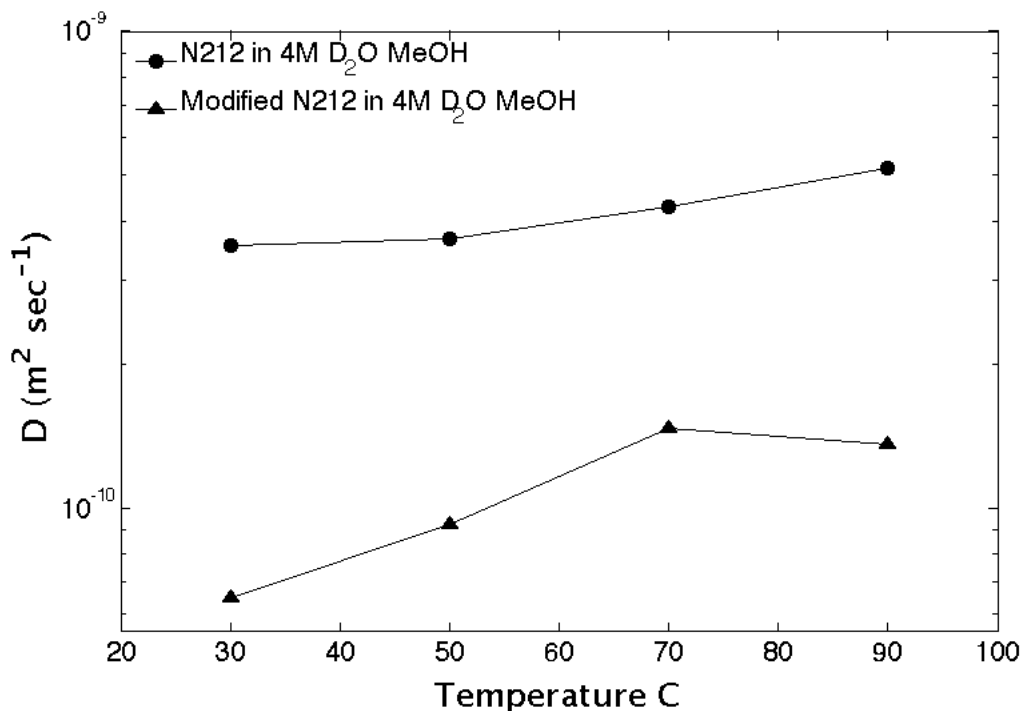


Figure 4.21: Comparison of MeOH diffusion in standard Nafion and modified Nafion

very large reduction in proton flux upon modification is not desirable even if selectivity is improved.

Figure 4.21 shows how modification affects methanol diffusion in the membranes. This diffusion coefficient is related only to methanol vehicular diffusion because when methanol is added to deuterium oxide, the hydroxyl proton will exchange out into solution over time. So the major component of the NMR signal is the CH<sub>3</sub> methyl group which cannot undergo Grotthus diffusion. The figure shows that modification has a more severe effect at reducing methanol diffusion. The figures also highlight the fact that regular Nafion shows similar diffusion of protons and methanol, which is why crossover is such a problem.

Figure 4.22 quantifies the performance of the membranes by showing the ratio of proton to methanol diffusion. Commercial Nafion only shows a small disparity between the two species. Overall the modification greatly improves selectivity while still maintaining decent diffusion rates. Obviously, even though methanol and water are similar in molecular size, methanol cannot use a Grotthus mechanism to get to the cathode. The thought is that imidazole obstructs the diffusive pathways of methanol while offering possible proton donor sites to protons of water. The effect is more prominent at lower temperatures where thermal motion is less and Grotthus-like behavior is needed to transport species through the membrane.

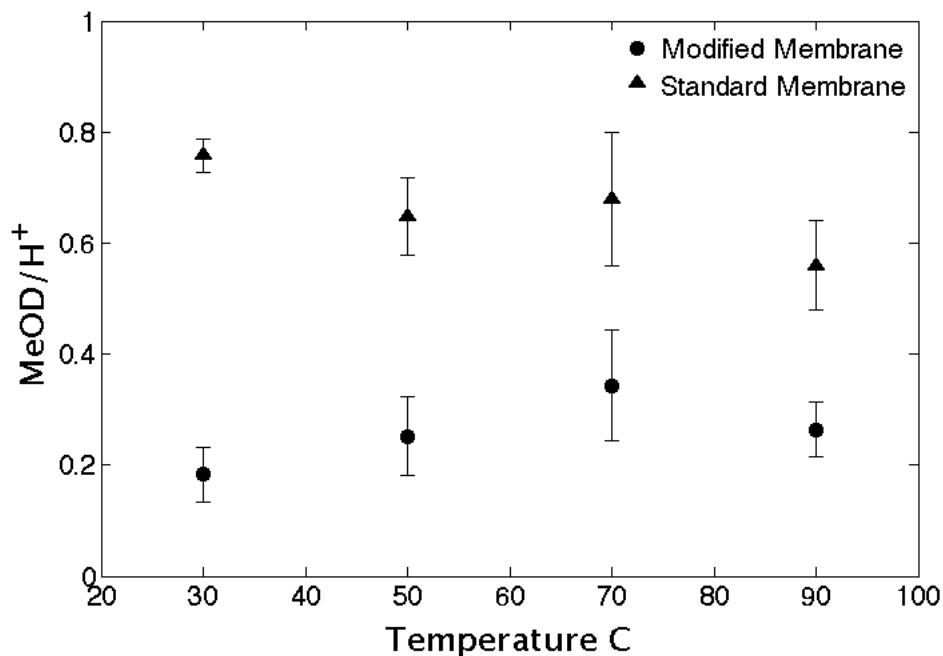


Figure 4.22: Ratio of proton to methanol diffusion vs. temperature

## 4.7 Conclusions

In this work, an array of solid-state NMR techniques were applied to understand the molecular detail of how imidazole-based additives improve membrane function. MAS experiments were performed to look at proton dynamics and hydration levels in the membranes. Abundant imidazole showed almost complete removal of water from the membrane at ambient conditions, while only partial addition allowed for natural water uptake from the environment. Cross-polarization experiments revealed that static imidazoles were fully protonated while direct detection experiments showed evidence of fast exchanging imidazoles. Finally, pulsed field gradient techniques were applied to show that imidazole effectively stifled methanol permeability while maintaining a respectable proton flux.

## 4.8 Supporting Information: Results of Spectrum Deconvolution

The tables in this section list the data needed to generate the fits in Figure 4.5. The population fractions are fixed as mentioned in this chapter. The lineshapes are Lorentzians.

Table 4.2: Summary of fitting parameters for peaks in 3M 825 EW with 100% ImOH substitution at 15 kHz MAS and -45 °C.

|        | Chemical Shift (ppm) | Linewidth (ppm) |
|--------|----------------------|-----------------|
| Peak 1 | 4.00                 | 6.86            |
| Peak 2 | 6.75                 | 1.40            |
| Peak 3 | 8.19                 | 1.43            |
| Peak 4 | 12.85                | 2.11            |
| Peak 5 | 4.50                 | 2.0             |

Table 4.3: Summary of fitting parameters for peaks in 3M 825 EW with 100% ImOH substitution at 15 kHz MAS and 35 °C.

|        | Chemical Shift (ppm) | Linewidth (ppm) |
|--------|----------------------|-----------------|
| Peak 1 | 3.95                 | 1.26            |
| Peak 2 | 6.65                 | .60             |
| Peak 3 | 7.99                 | .72             |
| Peak 4 | 11.95                | 1.55            |
| Peak 5 | 4.80                 | 1.50            |

Table 4.4: Summary of fitting parameters for peaks in 3M 825 EW with 100% ImOH substitution at 15 kHz MAS and 45 °C.

|        | Chemical Shift (ppm) | Linewidth (ppm) |
|--------|----------------------|-----------------|
| Peak 1 | 3.95                 | .75             |
| Peak 2 | 6.68                 | .36             |
| Peak 3 | 7.99                 | .42             |
| Peak 4 | 10.8                 | 1.90            |
| Peak 5 | 5.50                 | 1.90            |

Table 4.5: Summary of fitting parameters for peaks in 3M 825 EW with 100% ImOH substitution at 15 kHz MAS and 60 °C.

|        | Chemical Shift (ppm) | Linewidth (ppm) |
|--------|----------------------|-----------------|
| Peak 1 | 3.99                 | .37             |
| Peak 2 | 6.70                 | .23             |
| Peak 3 | 7.99                 | .29             |
| Peak 4 | 9.50                 | 1.36            |
| Peak 5 | 8.30                 | 1.36            |

Table 4.6: Summary of fitting parameters for peaks in 3M 825 EW with 100% ImOH substitution at 15 kHz MAS and 75 °C.

|        | Chemical Shift (ppm) | Linewidth (ppm) |
|--------|----------------------|-----------------|
| Peak 1 | 4.05                 | .15             |
| Peak 2 | 6.68                 | .12             |
| Peak 3 | 7.99                 | .15             |
| Peak 4 | 8.81                 | .56             |
| Peak 5 | 8.81                 | .56             |

Table 4.7: Summary of fitting parameters for peaks in 3M 825 EW with 100% ImOH substitution at 15 kHz MAS and 90 °C.

|        | Chemical Shift (ppm) | Linewidth (ppm) |
|--------|----------------------|-----------------|
| Peak 1 | 4.00                 | .12             |
| Peak 2 | 6.68                 | .10             |
| Peak 3 | 7.97                 | .12             |
| Peak 4 | 8.90                 | .42             |
| Peak 5 | 8.90                 | .42             |

## Chapter 5

# Interactions of PFSA Membranes and Organic Liquids

### 5.1 Acknowledgement

The author gratefully acknowledges the contributions to this work from Kyle Clark, a material science researcher in the group of John Kerr at Lawrence Berkeley National Laboratory, Lakshmi Krishnan, a researcher at GE Global Research for providing samples, and the entire team at GE Global Research.

### 5.2 Introduction

It is well known that proton conducting fuel cells have the advantage of high power and energy densities[35]. However, incorporating these devices into our current infrastructure remains very challenging. A large part of the problem is the lack of hydrogen storage and transport capabilities, especially safe and economical means for high pressure gaseous forms. One solution is to replace the proton source for PEM fuel cells with an organic molecule that acts as a virtual hydrogen carrier. These would produce protons and electrons at the anode without forming gaseous hydrogen. Once deprotonated, these liquids could be regenerated with protons and recycled.

Recent advances in reversible dehydrogenation/hydrogenation of carbocyclic and heterocyclic hydrocarbons have been promising in producing possibly regenerable organic fuel[36]. One aspect that requires greater understanding is how organics will affect traditional PEM membranes. The interaction of fuel with a polymer membrane could degrade mechanical properties or affect conductivity through morphological alterations. This study reports on the effects some model fuels have on the characteristics of Nafion 212.



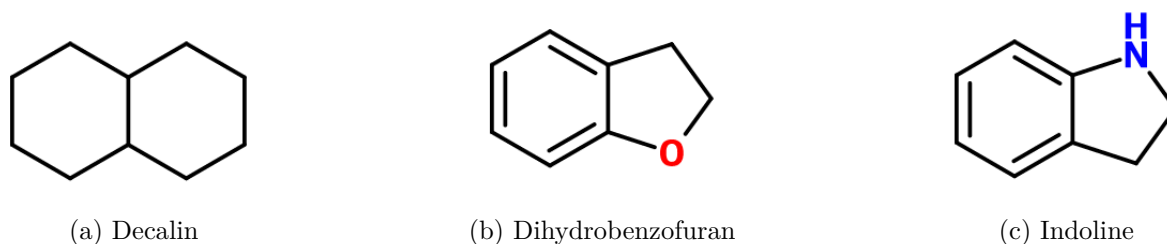


Figure 5.1: Model organic fuels tested for membrane interactions

### 5.3 Methods

SAXS data were collected at the ALS synchrotron at the Lawrence Berkeley National Laboratory. Samples were treated with the organic fuel for 24 hours before being removed and excess fuel wiped off. Samples were then mounted in a chamber and placed in front of the beam. Controlled humidity experiments were performed using a specially designed humidity chamber [37].

$^1\text{H}$  and  $^{19}\text{F}$  Magic Angle Spinning (MAS) NMR experiments were performed using the  $^1\text{H}$  channel of an H/X MAS probe (Eagle, Tecmag Inc., Houston, TX). Proton and Fluorine spectra were acquired using a Redstone spectrometer (Tecmag Inc.) with Larmor frequencies of 400 and 376 MHz, respectively. Untreated and fuel soaked samples were loaded into MAS rotors at laboratory conditions and spun at 12.5 kHz. This frequency was chosen to reduce spinning sideband overlaps.  $^{19}\text{F}$  spin-lattice relaxation in the rotating frame was measured using a standard pulse sequence with variable spin-locking frequencies and spin-lock times up to 20 ms and peak intensity decays were fit to an exponential decay model to obtain the reported  $T_{1\rho}$  parameter.

### 5.4 Results and Discussion

Standard Nafion membranes were soaked in model fuels for 24 hours before testing. Decalin (carbocyclic), dihydrobenzofuran (oxygen), and indoline (nitrogen heterocyclic) were tested. Figure 5.1 shows the structures of these three liquids.

#### 5.4.1 Bulk Membrane Measurements

Figure 5.2 shows the relative uptake of water as a function of relative humidity.  $\lambda$ , the number of water molecules per sulfonic acid group, is calculated from the equivalent weight of Nafion and the mass of water absorbed. The vapor sorption of Nafion is typical. However, when treated with decalin, the uptake increases by about 40%. Dihydrobenzofuran (DHBF) and indoline showed a vast decrease in water uptake. DHBF is polar and most likely interfering with the ionic phase of the material while indoline is a candidate

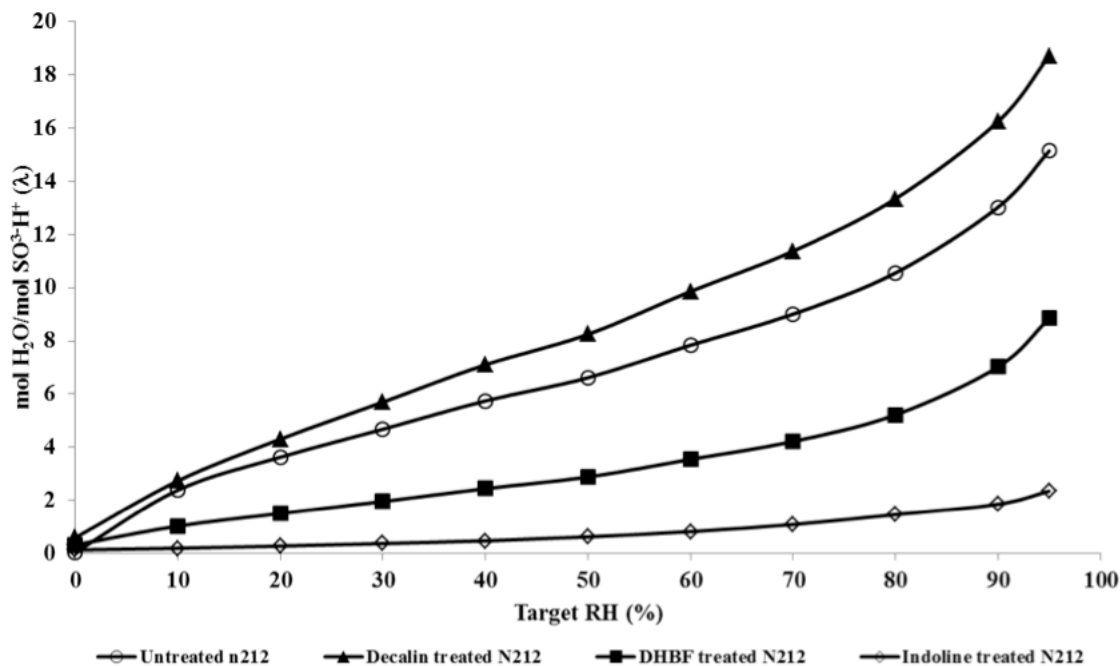


Figure 5.2: Vapor sorption isotherms for untreated and fuel treated N212 membranes at 50 °C vs. relative humidity. *Data courtesy Kyle Clark and Lakshmi Krishnan.*

to form acid-base complexes with the acid groups. This indoline result is similar to the 100% imidazole incorporation from the previous chapter that drastically reduced water uptake and conductivity.

Figure 5.3 shows the relation between relative humidity and proton conductivities. Regular Nafion shows the typical behavior in which the conductivity increases exponentially with humidity, showing that water uptake is very critical to Nafion conduction. Conversely, decalin treated N212 shows no dependence on the relative humidity for conduction. The conduction does not seem to bear the same relation to water activity. The DHBF membrane shows the same activity relation but at reduced conductivity. Indoline treated membranes showed almost no conductivity, giving further evidence for acid-base complexes as acid group are potentially blocked.

One possible explanation for the decalin data derives from the way the experiment was performed. The first measurement was at 70% RH, which was gradually decreased to 20% RH and then back all the way up to 95% RH. It seems possible that decalin treatment enhances water retention such that conductivity does not decrease as RH is lowered. Experiments were performed that started at low RH and went to high. These experiments showed a behavior similar to Nafion, but with a slight overall increase in conductivity over regular Nafion.

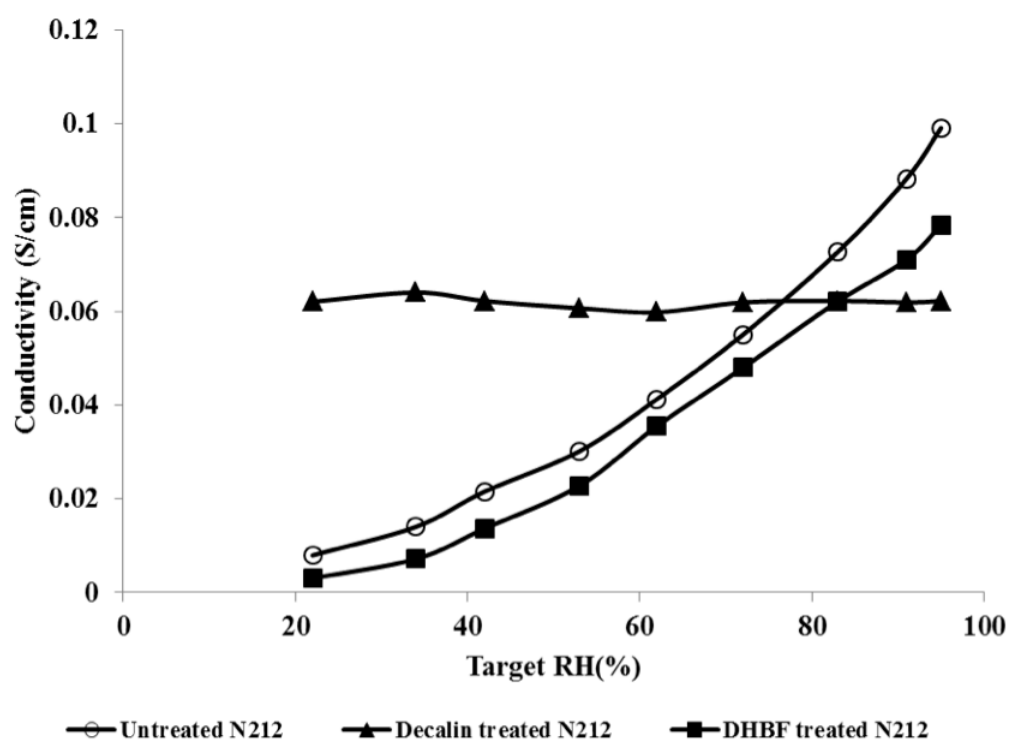


Figure 5.3: Proton conductivity vs. RH at 75 50 °C for untreated and treated membranes. Data courtesy Kyle Clark and Lakshmi Krishnan.

### 5.4.2 SAXS

To understand how decalin might be affecting the polymer morphology and hydration response, X-ray scattering experiments were used. Typical Nafion SAXS measurements reveal two maxima[38]. The peak around  $.05 \text{ \AA}^{-1}$   $q$  values represents lamellar crystalline domains while those around  $.15 \text{ \AA}^{-1}$   $q$  values derive from the ionic phase clusters imbibed with water. These ionic clusters phases are sensitive to RH as seen in Figure 5.4a. As RH increases, the ionic domain clusters become broader and move to smaller  $q$  value. This indicates that the definite spacing between the clusters is becoming less defined and the characteristic size is increasing, from roughly 3.2 nm to 4.6 nm in this case. In addition, the crystallite peak increases in intensity and shifts slightly to lower  $q$  value.

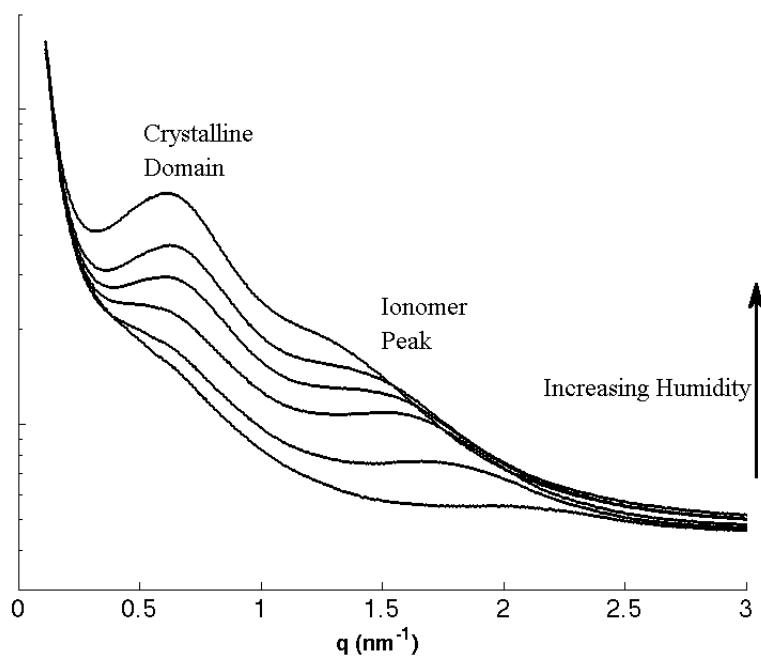
The decalin treated SAXS profiles are quite different. The crystallite peaks are significantly broadened, indicating less crystallinity. The ionomer peak maintains a roughly constant  $q$  value but does become much more defined as RH increases, implying that the ionic domains are not changing in size, but are becoming more regular and well-defined. Overall, decalin effects the morphology of Nafion and how it responds to hydration.

### 5.4.3 Solid-State NMR

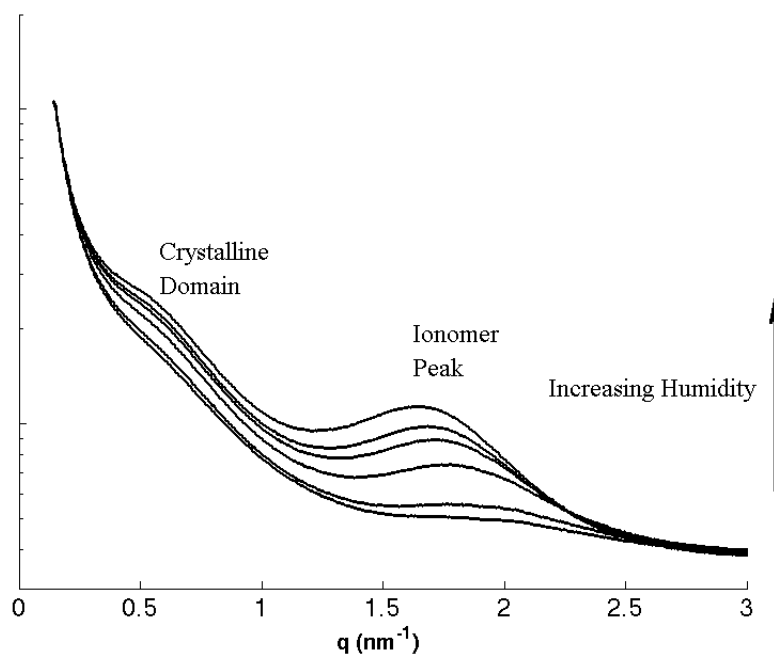
The presented SAXS data offer a static, morphological picture of the polymeric structure. To get an idea of how the dynamics are affected, NMR relaxation was measured. Spin-lattice relaxation in the rotating frame is well-suited for monitoring polymer motions in the kHz range. Figure 5.5 shows the basic pulse sequence. A  $\frac{\pi}{2}$  pulse is followed by a long spin-locking pulse that is 90 degrees phase shifted which acts to precess the magnetization along the spin locking field. Gradually, the magnetization will decay due to relaxation. Motional modes near the experimental spin-lock frequency will increase relaxation rates (i.e., smaller  $T_{1\rho}$  values). The spectroscopic resolution provided by MAS allows for the distinction of fluorine signals from i) main-chain  $\text{CF}_2$ , ii) side-chain  $\text{O-CF}_2$  and  $\text{CF}_3$  and iii) side-chain  $\text{S-CF}_2$  directly adjacent to the sulfonic acid group in the Nafion membrane. The chemical shifts of these species have already been determined[39]. Resolution garners distinct  $T_{1\rho}$  values for each of these sections of the polymer. Figure 5.6 shows the relative effect of decalin treatment on main-chain fluorines and side-chain (excluding fluorines directly next to the acid group).

Overall  $T_{1\rho}$  values are shorter for side-chain nuclei, which is attributed to side-chains having more motional freedom and thus more routes for relaxation processes[40]. In addition, decalin treatment markedly reduces the  $T_{1\rho}$  values over the entire spectral frequency range compared to the untreated Nafion. This reduction suggests that decalin treatment increases motional modes in both the backbone and side-chain moieties. This is direct evidence of interaction between the decalin and the hydrophobic portion of the polymer.

To assess dynamics near the hydrophobic/hydrophilic interface, Figure 5.7 shows relaxation of only the terminal  $\text{CF}_2$  group near the end of the side-chain.  $T_{1\rho}$  values are nearly identical despite decalin treatment. These fluorines are adjacent to the acid groups,



(a) Untreated Nafion



(b) Decalin treated Nafion

Figure 5.4: SAXS profiles of untreated and decalin treated membranes at 50 °C with increasing RH. The humidities are 25%, 35%, 50%, 75%, 85%, and 95%.

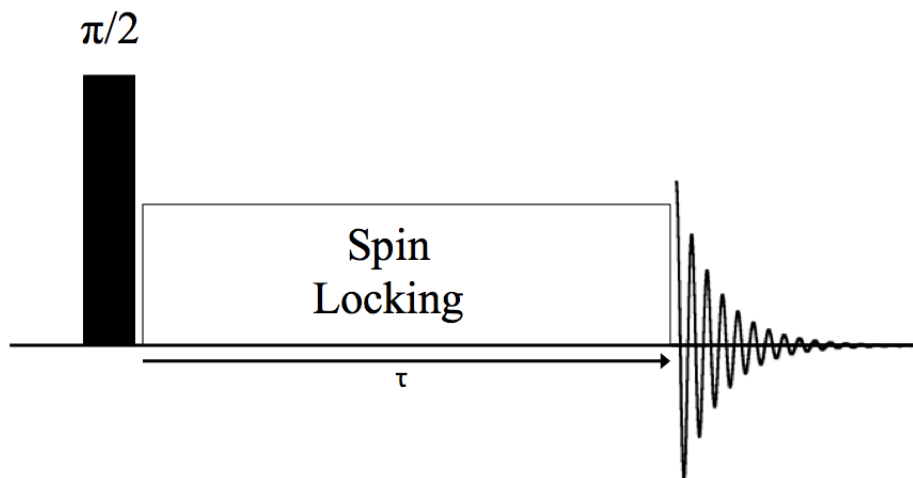


Figure 5.5: Pulse sequence for  $T_{1\rho}$  measurement

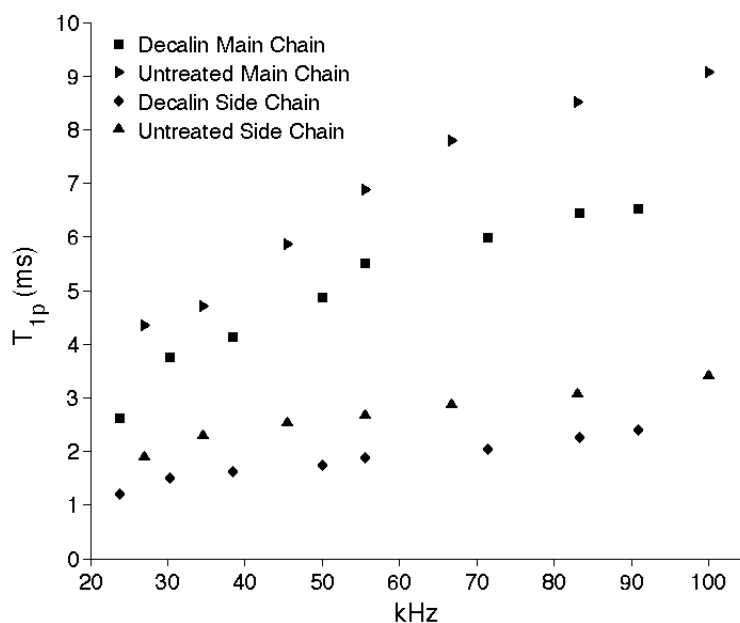


Figure 5.6:  $T_{1\rho}$  for main-chain and side-chain fluorine in untreated and decalin treated N212 membranes as a function of spinlock frequency

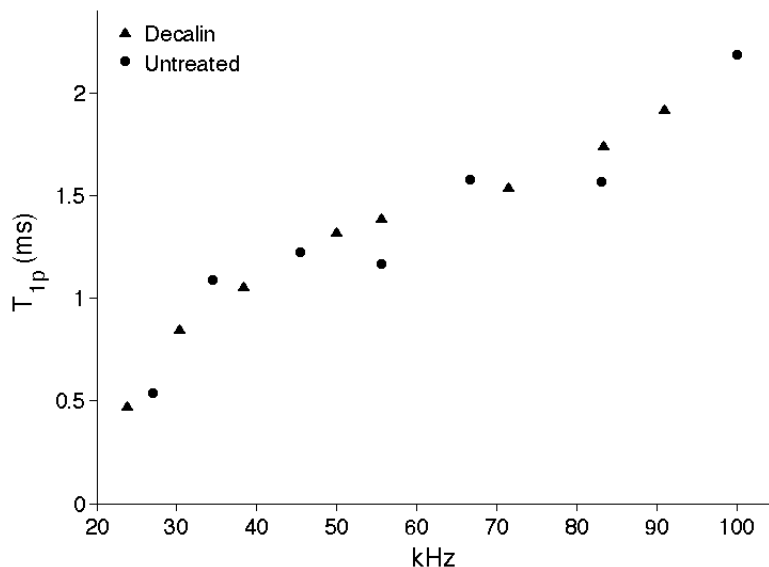


Figure 5.7:  $T_{1\rho}$  for terminal fluorine group in untreated and decalin treated N212 membranes as a function of spinlock frequency

which are solvated by water during hydration. This implies that decalin does not interfere with the interplay between water and the ionic groups. These NMR experiments support SAXS results, which show that decalin mitigates the presence of well-defined the crystallite domains, implying a less ordered, more dynamic backbone. SAXS data also showed that ionic clustering still occurred in decalin treated membranes, and NMR data show no effect on motion near the hydrophilic interface.

Figure 5.8 shows the  $^1\text{H}$  MAS spectrum of decalin treated membranes. The figure demonstrates the disparate spin-lattice relaxation times between the water in the hydrophilic channels (9 ppm) and the decalin (1.7 ppm). Water in Nafion typically shows very short relaxation times, especially when compared to bulk water [41]. In this sample water has a  $T_1$  of only 15 milliseconds while decalin's is 150 milliseconds. The important conclusion is that the two species are not spatially close as spin-diffusion is not apparent between the two populations. This is further evidence that decalin is very much confined to the hydrophobic polymer phase.

## 5.5 Conclusions

The effect of model organic fuels on Nafion was investigated. Decalin treated membranes increased water uptake and maintained relatively high proton conductivities. The other fuels produced poor results in these metrics. SAXS data showed that decalin interferes with the backbone crystallinity while allowing ionic domains to form in regular patterns. NMR data showed that the addition of decalin increased motion throughout

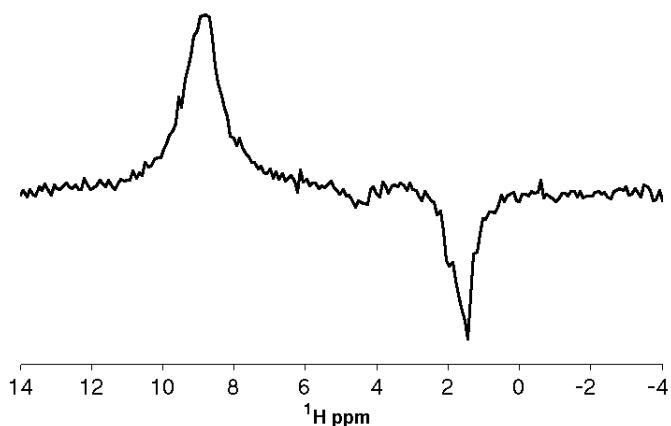


Figure 5.8:  $^1\text{H}$  MAS spectrum of decalin treated Nafion at 76 MHz. This spectrum is taken from an inversion recovery sequence taken with 30 ms delay after the  $\pi$  pulse.

the hydrophobic phase of the polymer, but did not affect motion near the ionic domains. A model can be constructed to explain these results. Standard Nafion consists of well-defined crystalline domains surrounded by interconnecting, amorphous ionic domains. This allows high conductivity in the hydrated state and the easy release or uptake of water when RH changes. When treated with decalin, the crystallites are diminished, and the water activity more easily pushes the polymer out of the when swelling during hydration. Because water domains experience less resistance from a rigid, crystallized polymer, the water domains seem to assume a particular size which is likely a function of solvation thermodynamics. The results is more regularly patterned ionic domain surrounded by an amorphous polymer phase. Figure 5.7 provides a general interpretation of these findings.



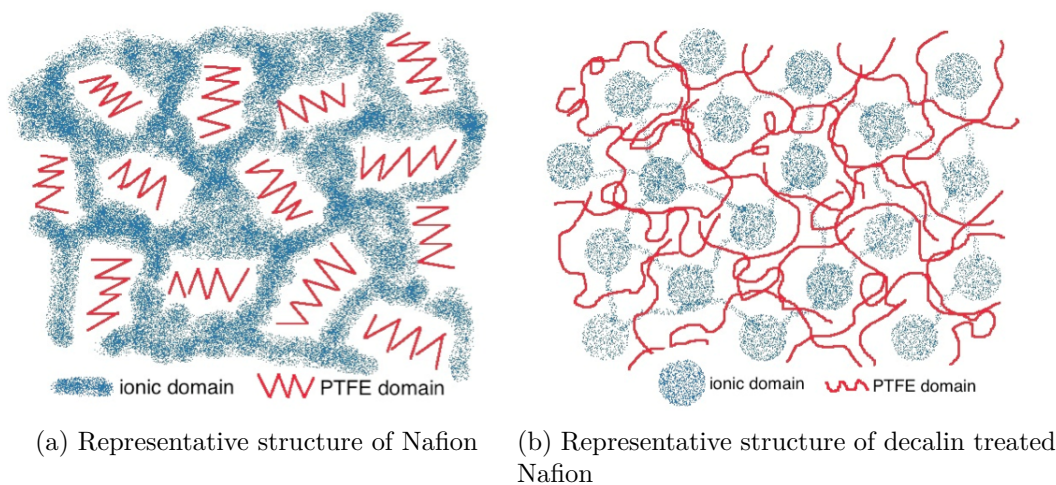


Figure 5.9: Interpretation of morphological changes to Nafion when treated with decalin.  
*Illustration courtesy of Gary Yeager*

# Bibliography

- [1] L Carrette, K A Friedrich, and U Stimming. Fuel cells—fundamentals and applications. *Fuel Cells*, 1(1):5–39, 2001.
- [2] K D Kreuer. On the development of proton conducting materials for technological applications. *Solid State Ionics*, 97(1-4):1–15, 1997.
- [3] G Ye, C A Hayden, and G R Goward. Proton Dynamics of Nafion and Nafion/SiO<sub>2</sub> Composites by Solid State NMR and Pulse Field Gradient NMR. *Macromolecules*, 40(5):1529–1537, March 2007.
- [4] S J Paddison, K D Kreuer, and J Maier. About the choice of the protogenic group in polymer electrolyte membranes: Ab initio modelling of sulfonic acid, phosphonic acid, and imidazole functionalized . . . . *Physical Chemistry Chemical . . . .*, 2006.
- [5] K D Kreuer, A Fuchs, M Ise, M Spaeth, and J Maier. Imidazole and pyrazole-based proton conducting polymers and liquids. *Electrochimica Acta*, 43(10-11):1281–1288, 1998.
- [6] Akihiro Noda, Md Abu Bin Hasan Susan, Kenji Kudo, et al. Bronsted Acid-Base Ionic Liquids as Proton-Conducting Nonaqueous Electrolytes. *The Journal of Physical Chemistry B*, 107(17):4024–4033, 2003.
- [7] F S Bates and G H Fredrickson. Block copolymers - Designer soft materials. *Physics Today*, 52(2):32–38, February 1999.
- [8] K Schmidt-Rohr and H W Spiess. *Multidimensional Solid-State NMR and Polymers*. Elsevier Science, 1994.
- [9] W Münch, K D Kreuer, W Silvestri, J Maier, and G Seifert. The diffusion mechanism of an excess proton in imidazole molecule chains: first results of an ab initio molecular dynamics study. *Solid State Ionics*, 145(1-4):437–443, 2001.
- [10] J M Virgili, M L Hoarfrost, and R A Segalman. Effect of an ionic liquid solvent on the phase behavior of block copolymers. *Macromolecules*, 43(12):5417–5423, 2010.

- [11] Justin M Virgili, Alexander Hexemer, John A Pople, Nitash P Balsara, and Rachel A Segalman. Phase Behavior of Polystyrene- block-poly(2-vinylpyridine) Copolymers in a Selective Ionic Liquid Solvent. *Macromolecules*, 42(13):4604–4613, July 2009.
- [12] M L Hoarfrost and R A Segalman. Conductivity Scaling Relationships for Nanostructured Block Copolymer/Ionic Liquid Membranes. *ACS Macro Letters*, 1(8):937–943, 2012.
- [13] M Schuster, W H Meyer, G Wegner, et al. Proton mobility in oligomer-bound proton solvents: imidazole immobilization via flexible spacers. *Solid State Ionics*, 145(1-4):85–92, 2001.
- [14] H W Spiess. Deuteron NMR — a new tool for studying chain mobility and orientation in polymers. In *Characterization of Polymers in the Solid State I: Part A: NMR and Other Spectroscopic Methods Part B: Mechanical Methods*, pages 23–58. Springer Berlin Heidelberg, Berlin, Heidelberg, January 1985.
- [15] H Yokoyama, T E Mates, and E J Kramer. Structure of asymmetric diblock copolymers in thin films. *Macromolecules*, 33(5):1888–1898, 2000.
- [16] D Kuckling and S Wohlrab. Synthesis and characterization of bireponsive graft copolymer gels. *Polymer*, 43(4):1533–1536, 2002.
- [17] Gillian R Goward, Martin F H Schuster, Daniel Sebastiani, Ingo Schnell, and Hans Wolfgang Spiess. High-Resolution Solid-State NMR Studies of Imidazole-Based Proton Conductors: Structure Motifs and Chemical Exchange from  $^1\text{H}$  NMR. *The Journal of Physical Chemistry B*, 106(36):9322–9334, 2002.
- [18] Salvador Maf, Jos A Manzanares, and Patricio Ramirez. Modeling of surface vs. bulk ionic conductivity in fixed charge membranes. *Physical Chemistry Chemical Physics*, 5(2):376–383, November 2002.
- [19] M L Hoarfrost, M S Tyagi, and R A Segalman. Effect of confinement on proton transport mechanisms in block copolymer/ionic liquid membranes. *Macromolecules*, 45(7):3112–3120, 2012.
- [20] J Li, K G Wilmsmeyer, and L A Madsen. Anisotropic diffusion and morphology in perfluorosulfonate ionomers investigated by NMR. *Macromolecules*, 42(1):255–262, 2008.
- [21] H A Every, F Zhou, M Forsyth, and D R MacFarlane. Lithium ion mobility in poly (vinyl alcohol) based polymer electrolytes as determined by  $^7\text{Li}$  NMR spectroscopy. *Electrochimica Acta*, 1998.

- [22] S R Benhabbour, R P Chapman, G Scharfenberger, W H Meyer, and G R Goward. Study of Imidazole-Based Proton-Conducting Composite Materials Using Solid-State NMR. *Chemistry of Materials*, 17(6):1605–1612, March 2005.
- [23] Ümit Akbey, Sergio Granados-Focil, E Bryan Coughlin, Robert Graf, and Hans Wolfgang Spiess.  $^1\text{H}$  solid-state NMR investigation of structure and dynamics of anhydrous proton conducting triazole-functionalized siloxane polymers. *The Journal of Physical Chemistry B*, 113(27):9151–9160, July 2009.
- [24] Alex D Bain. Chemical exchange in NMR. *Progress in Nuclear Magnetic Resonance Spectroscopy*, 43(3-4):63–103, 2003.
- [25] João F Mano. Cooperativity in the Crystalline  $\alpha$ -Relaxation of Polyethylene. *Macromolecules*, 34(26):8825–8828, 2001.
- [26] David van der Spoel, Paul J van Maaren, Per Larsson, and Nicusor Tîmneanu. Thermodynamics of hydrogen bonding in hydrophilic and hydrophobic media. *The Journal of Physical Chemistry B*, 110(9):4393–4398, March 2006.
- [27] T Ueda, H Masui, and N Nakamura. One- and two-dimensional  $^{15}\text{N}$  exchange CP/MAS NMR studies of the structure and electronic properties of the intermolecular N-H...N hydrogen bond in imidazole crystal. *Solid State Nuclear Magnetic Resonance*, 20(3-4):145–155, November 2001.
- [28] Kenneth A Mauritz and Robert B Moore. State of Understanding of Nafion. *Chemical Reviews*, 104(10):4535–4586, October 2004.
- [29] A Heinzl and V M Barragán. A review of the state-of-the-art of the methanol crossover in direct methanol fuel cells. *Journal of Power Sources*, 84(1):70–74, November 1999.
- [30] P S Kauranen and E Skou. Methanol permeability in perfluorosulfonate proton exchange membranes at elevated temperatures. *Journal of Applied Electrochemistry*, 26(9):909–917, September 1996.
- [31] M H Frey and S J Opella. The Effect of pH on solid-state  $^{13}\text{C}$  NMR spectra of histidine. *Journal of Magnetic Resonance (1969)*, 66(1):144–147, 1986.
- [32] Ingrid Fischbach, Hans Wolfgang Spiess, Kay Saalwächter, and Gillian R Goward. Solid State NMR Spectroscopic Investigations of Model Compounds for Imidazole-Based Proton Conductors. *The Journal of Physical Chemistry B*, 108(48):18500–18508, December 2004.
- [33] William S Price. Pulsed-field gradient nuclear magnetic resonance as a tool for studying translational diffusion: Part II. Experimental aspects. *Concepts in Magnetic Resonance*, 10(4):197–237, January 1998.

- [34] E O STEJSKAL and J E TANNER. Spin Diffusion Measurements: Spin Echoes in the Presence of a Time-Dependent Field Gradient. *The Journal of Chemical Physics*, 42(1):288, 1965.
- [35] Wolf Vielstich, Arnold Lamm, Hubert A Gasteiger, and Harumi Yokokawa, editors. *Handbook of Fuel Cells*. John Wiley & Sons, Ltd, Chichester, UK, December 2010.
- [36] C Moyses Araujo, Davide L Simone, Steven J Konezny, et al. Fuel selection for a regenerative organic fuel cell/flow battery: thermodynamic considerations. *Energy Environ. Sci.*, 5(11):9534–9542, October 2012.
- [37] Andrew Jackson, Keith M Beers, X Chelsea Chen, et al. Design of a humidity controlled sample stage for simultaneous conductivity and synchrotron X-ray scattering measurements. *Review of Scientific Instruments*, 84(7):075114, July 2013.
- [38] Mineo Fujimura, Takeji Hashimoto, and Hiromichi Kawai. Small-angle x-ray scattering study of perfluorinated ionomer membranes. 1. Origin of two scattering maxima. *Macromolecules*, 14(5):1309–1315, 1981.
- [39] Q Chen and K Schmidt-Rohr.  $^{19}\text{F}$  and  $^{13}\text{C}$  NMR Signal Assignment and Analysis in a Perfluorinated Ionomer (Nafion) by Two-Dimensional Solid-State NMR. *Macromolecules*, 37(16):5995–6003, August 2004.
- [40] Kirt A Page, William Jarrett, and Robert B Moore. Variable temperature  $^{19}\text{F}$  solid-state NMR study of the effect of electrostatic interactions on thermally-stimulated molecular motions in perfluorosulfonate ionomers. *Journal of Polymer Science Part B: Polymer Physics*, 45(16):2177–2186, 2007.
- [41] B MacMillan, A R Sharp, and R L Armstrong. An nmr investigation of the dynamical characteristics of water absorbed in Nafion. *Polymer*, 40(10):2471–2480, 1999.
- [42] Hiroyasu Furukawa, Kyle E Cordova, Michael O’Keeffe, and Omar M Yaghi. The Chemistry and Applications of Metal-Organic Frameworks. *Science*, 341(6149):974–974, August 2013.
- [43] Moisés L Pinto, Luís Mafra, José M Guil, João Pires, and João Rocha. Adsorption and Activation of  $\text{CO}_2$  by Amine-Modified Nanoporous Materials Studied by Solid-State NMR and  $^{13}\text{C}$  Adsorption. *Chemistry of Materials*, 23(6):1387–1395, March 2011.
- [44] M Alei, L O Morgan, W E Wageman, and T W Whaley. The pH dependence of nitrogen-15 NMR shifts and coupling constants in aqueous imidazole and 1-methylimidazole. Comments on estimation of tautomeric equilibrium constants for aqueous histidine. *Journal of the American Chemical Society*, 102(9):2881–2887, April 1980.

## Appendix A

# Carbon Dioxide Capture in Amine Functionalized Metal Organic Frameworks (MOFs)

This appendix describes the use of solid-state NMR to demonstrate the capture of carbon dioxide gas in MOFs in the presence of water. MOFs comprise metal clusters that are held together by organic linkers. MOFs show special promise because of the high modularity in their design[42]. The linkers can be functionalized through simple chemistry to produce pores with particular properties to suit the task.

In this study, the internal pores of MOFs were functionalized with various amine-based constituents, and NMR provided the spectroscopic evidence to confirm carbon dioxide uptake and determine its chemical form upon binding with the MOF framework. The work represents a collaborative effort between the Yaghi lab in the Chemistry Department and the Reimer lab.

### A.1 Methods

Samples of IRMOF-74-III were synthesized by Alejandro Fracaroli in the group of Professor Omar Yaghi. This particular MOF features magnesium oxide rods joined by terphenylene organic linkers. Four different functionalized samples were made. The linker functional groups were  $-\text{NH}_2$ ,  $-\text{CH}_2\text{NHBoc}$ ,  $-\text{CH}_2\text{NH}_2$ , and  $-\text{CH}_2\text{NHMe}$ , where Boc is tertbutyloxycarbonyl. These functionalities represent an unprotected primary amine ( $-\text{CH}_2\text{NH}_2$ ) and secondary amine ( $-\text{CH}_2\text{NHMe}$ ) along with the Boc groups which represent protected versions of these amines.

## A.2 Results and NMR Details

The four MOF varieties show significant CO<sub>2</sub> uptake based on isotherm measurements. The two samples with Boc protecting groups have a reduced uptake due to the sterically bulky protecting groups. Interestingly, the unprotected amine MOFs show very high uptake initially, but after evacuation for two hours at room temperature, the repeat experiment showed significantly reduced CO<sub>2</sub> uptake. This evidence points to strongly bound CO<sub>2</sub> in the unprotected amine MOFs. To understand how CO<sub>2</sub> binds in the framework, cross-polarization magic angle spinning (CP/MAS) <sup>13</sup>C NMR spectra were collected for each MOF after exposure to CO<sub>2</sub>. The four samples were exposed to 1 atm of <sup>13</sup>C-labeled CO<sub>2</sub> for 24 hours before the samples were loaded into NMR rotors.

CP/MAS was used to acquire <sup>13</sup>C NMR data at 75.47 MHz. Standard inversion recovery experiments were performed on the <sup>1</sup>H channel to determine the adequate recycle delay (1.6 seconds). A ramped-amplitude cross-polarization matching condition was used with the center of the increasing proton ramp saddled around the full breadth of the first matching sideband condition above the centerband. The centerband matching frequency was 48 kHz, the MAS rate was 10 kHz, and the CP contact time was 5 milliseconds. Continuous wave (CW) decoupling was applied during acquisition at a frequency of 35 kHz. The <sup>13</sup>C chemical shifts are given relative to the methylene carbon signal of adamantane assigned to 37.77 ppm as a secondary reference.

Figure A.1 shows the <sup>13</sup>C NMR spectra for the four MOF samples after CO<sub>2</sub> exposure. The two unprotected amine samples display a large resonance peak around 160 ppm with a shouldering peak at 164 ppm. This peak is ascribed to carbamic acid at 160 ppm and carbamate at 164 ppm[43]. The formation of carbamate species is expected in the reaction of CO<sub>2</sub> with the unprotected amines. This peak is evidence of a chemical binding of CO<sub>2</sub> to the amine. The peak is absent from the other two samples, showing that CO<sub>2</sub> does not bind to the -NH<sub>2</sub> and -CH<sub>2</sub>NHBoc functionalities. Because cross-polarization is used, free CO<sub>2</sub> in the MOF pore should not be seen due to increased motion and lack of strong coupling to <sup>1</sup>H; only chemisorbed carbon dioxide is detected. One last feature of Figure A.1 is the lineshape of the carbamic acid peak. The -CH<sub>2</sub>NHMe carbamate peak is broader than that of -CH<sub>2</sub>NH<sub>2</sub>. This most likely derives from the increased mobility of the smaller functional group.

To investigate the reversibility of CO<sub>2</sub> uptake, a second set of spectra were taken after opening the NMR rotors and placing them in a nitrogen stream at 120 °C for 1 hour. Figure A.2 shows the two CO<sub>2</sub> binding MOFs before and after heating. The magic angle was corrected for these spectra so resolution is greater. Figure A.2a shows the primary amine with a sharp carbamate peak before heating and almost complete removal of that peak upon heating. The sharp peak around 175 ppm has a sister peak at about 168 ppm (data not shown), which is native to the MOF linkers. This accounts for much of the signal in the 160-168 ppm region after heating. Thus the reversibility of the carbamate formation is quite clear. Subtracting out the native MOF peaks, the reduction is about 94%. Figure A.2b shows the secondary amine with a larger carbamate lineshape,

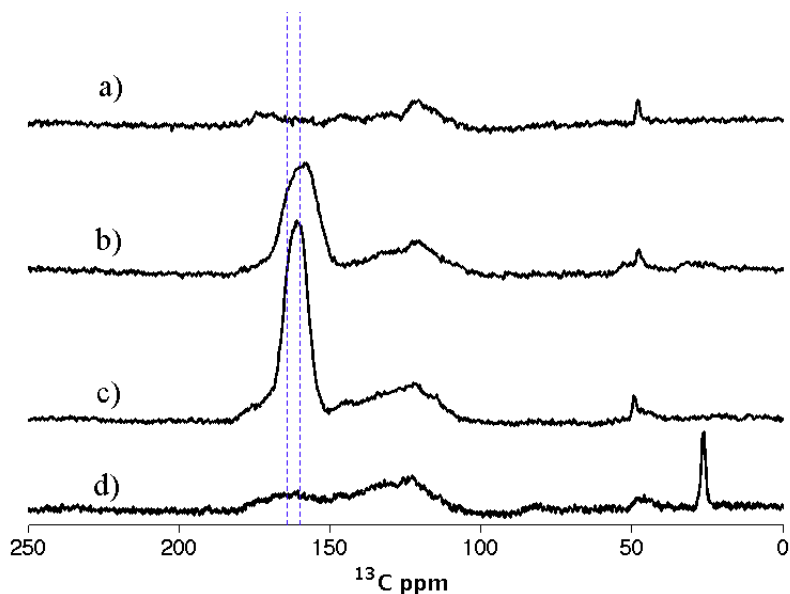


Figure A.1:  $^{13}\text{C}$  CP/MAS spectra of a) IRMOF-74-III- $\text{NH}_2$ , b)  $-\text{CH}_2\text{NHMe}$ , c)  $-\text{CH}_2\text{NH}_2$  and d)  $-\text{CH}_2\text{NHBoc}$  treated with  $^{13}\text{C}$ -labeled carbon dioxide and recorded at 25 °C. The vertical lines are at 160 and 164 ppm. The general broadness of the spectrum derives from an offset in the magic angle.

likely because of reduced motion. The spectrum after heating shows a large reduction of carbamate species. The reduction is not as severe as the primary amine and at about 85%.

The experiments confirm the reversibility of carbon dioxide binding to the amines and also show that the binding is stronger to the secondary amine as also demonstrated in break through time experiments in the Yaghi lab. Higher temperatures would be required to liberate the same fraction of carbamate from the secondary amine MOF.

This collaboration confirmed the reversibility of  $\text{CO}_2$  chemisorption in amine based functionalities in a MOF. The NMR data also showed that the dominate species is carbamic acid at 160 ppm, which is important in understanding the proton transfer dynamics and acidity of the carbamate species once formed.



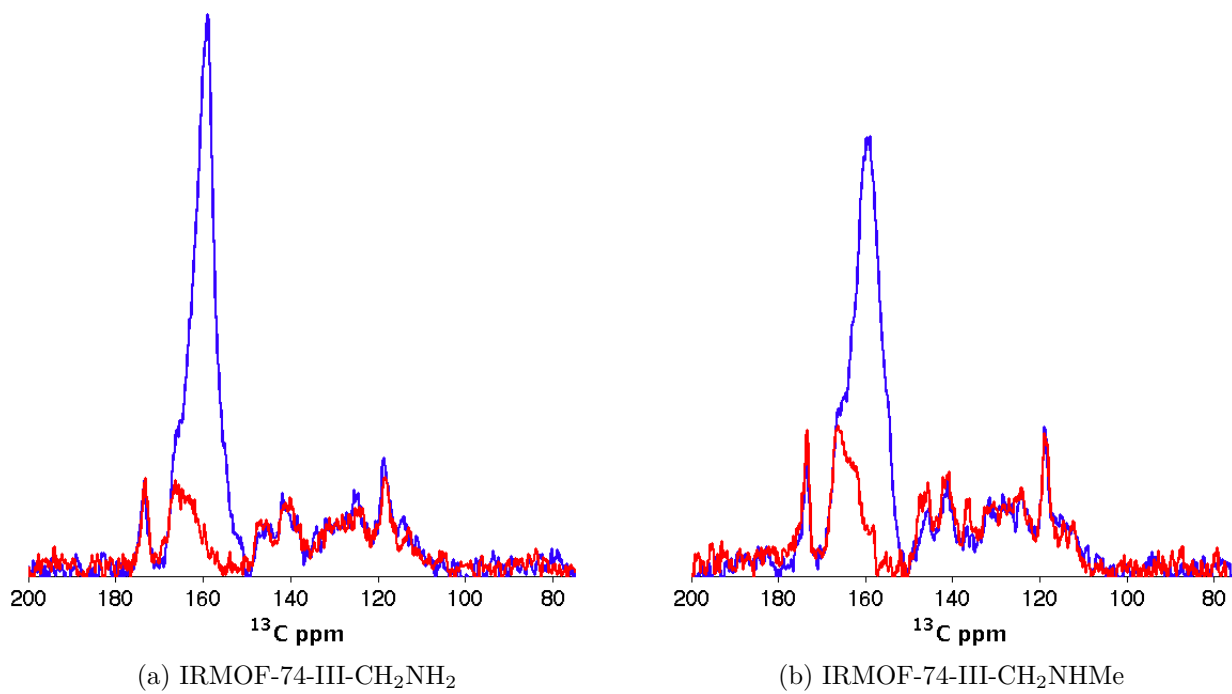


Figure A.2:  $^{13}\text{C}$  CP/MAS spectra after initial  $\text{CO}_2$  loading (blue) and after heating over flowing  $\text{N}_2$  (red)

## Appendix B

# $^{15}\text{N}$ NMR Studies of Imidazole-based Ionic Liquids

This appendix details the results of using  $^{15}\text{N}$  NMR to study molecular dynamics and chemical environments in [Im][TSFI] in both neat ionic liquid form and imbibed in polymer. This is the same system as detailed in Chapter 2. The idea is that  $^{15}\text{N}$  NMR offers better information on imidazole because it is a more sensitive handle for chemical environments due to the relatively large chemical shift range compared to  $^1\text{H}$ . Powder patterns of imidazole provide details on molecular motion, especially possible ring flip motions which are essential to Grotthus mechanism proton conduction.

### B.1 Methods

The same synthetic routes as outlined in Chapter 2 were performed for this work except the ionic liquid was made  $^{15}\text{N}$  enriched imidazole at both nitrogens. The very low natural abundance and small magnetogyric ratio of  $^{15}\text{N}$  necessitates enrichment.  $^{14}\text{N}$  is the more common nucleus for nitrogen, but its quadrupole moment renders it much less useful for these studies.  $^{15}\text{N}$  enriched imidazole was made by the author using the procedure outlined in the literature[44]. This imidazole was combined with HTSFI to make symmetric ionic liquid.

$^{15}\text{N}$  powder patterns were recorded on a 7.05 Tesla magnet, which corresponds to a 30.38 MHz NMR frequency. A cross-polarization scheme was used, followed by a spin echo so the full FID could be recorded at the top of the echo. The echo delay was 30  $\mu\text{s}$ . Continuous wave  $^1\text{H}$  decoupling was employed during the echo and acquisition.  $^{15}\text{N}$  VT MAS experiments were also performed. Corresponding  $^1\text{H}$  VT MAS spectrum were recorded at these temperatures. The shifts were referenced to the  $^{15}\text{N}$  chemical shift of -346.40 ppm with respect to nitromethane  $\text{CH}_3\text{NO}_2$ .

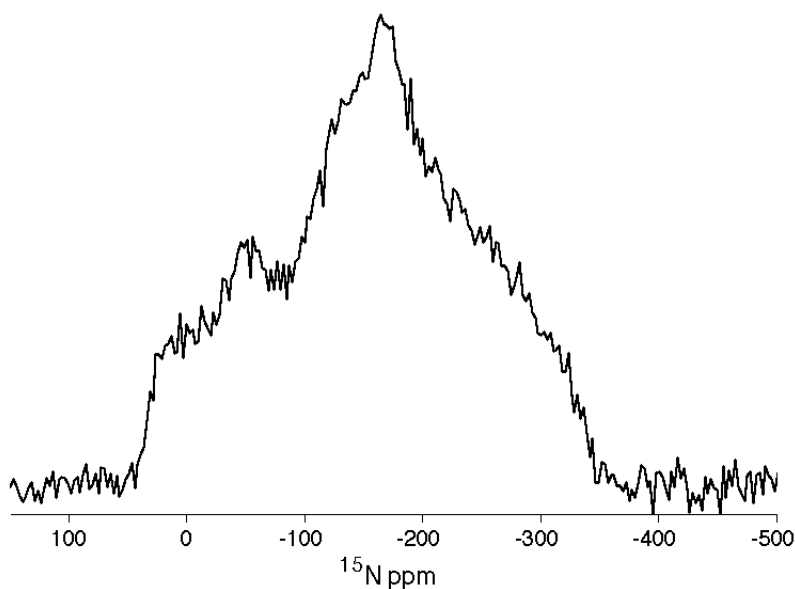


Figure B.1:  $^{15}\text{N}$  powder spectrum of crystallized imidazole at room temperature. 2084 scans were acquired using an 80 second recycle delay.

## B.2 Results and Discussion

### B.2.1 $^{15}\text{N}$ Powder Spectra

Figure B.1 shows the  $^{15}\text{N}$  powder pattern of crystalline imidazole. This spectrum consists of two different nitrogen centers with different chemical shielding anisotropy (CSA) tensors. The maximum and minimum chemical shifts present as well as the position of the most intense peak define the principal tensor components in the crystal frame. These values define a tensor that only has non-zero components only along the diagonal. Truly static molecules will display the widest spectrum possible. The presence of motion works to average the chemical shift distribution, and the spectrum will narrow. In liquids, there is complete averaging of the CSA, and only the isotropic chemical shift is observed at the weighted average chemical shift of the static powder pattern.

The unprotonated nitrogen appears on the left side of the spectrum in Figure B.1 with its middle principal component around -75 ppm. The protonated nitrogen has its middle principal component around -170 ppm. The total width of the spectrum is about 400 ppm. MAS will average the tensor and present only the isotropic chemical shifts at fast enough spinning rates. At this magnetic field, the breadth of the spectrum is about 12 kHz. Spinning above this speed will effectively average the chemical shift.

Figure B.2 shows the MAS spectrum of crystalline imidazole. The spinning effectively average the powder pattern and we see the two nitrogen peaks. The peak on the left is from unprotonated imidazole and the right is protonated. Even though the peak on the left

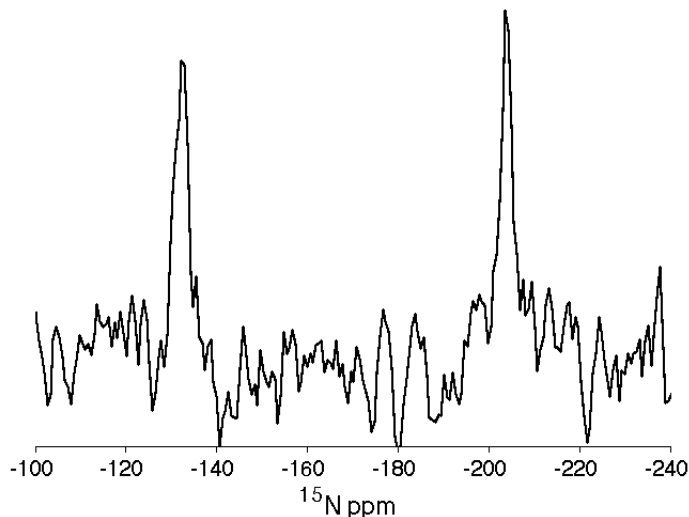
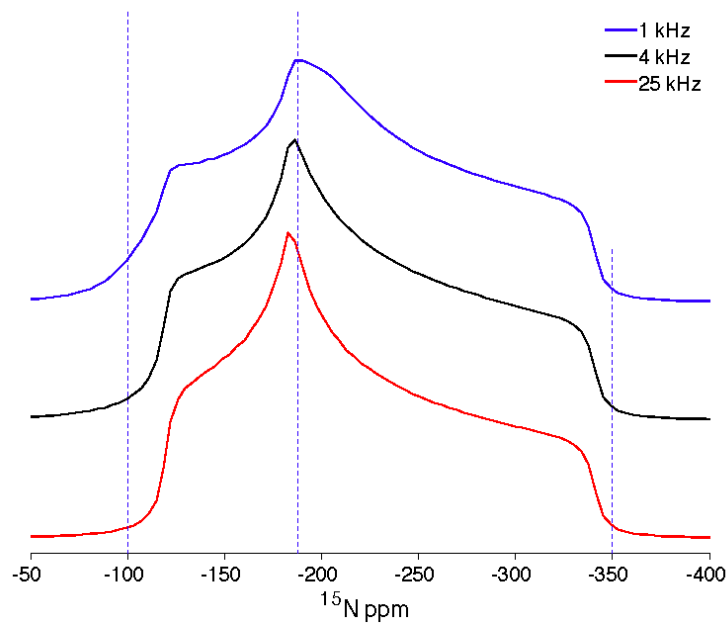


Figure B.2:  $^{15}\text{N}$  CP/MAS spectrum of imidazole crystals at room temperature at 12 kHz MAS. 16 scans were used with an 80 second recycle delay.

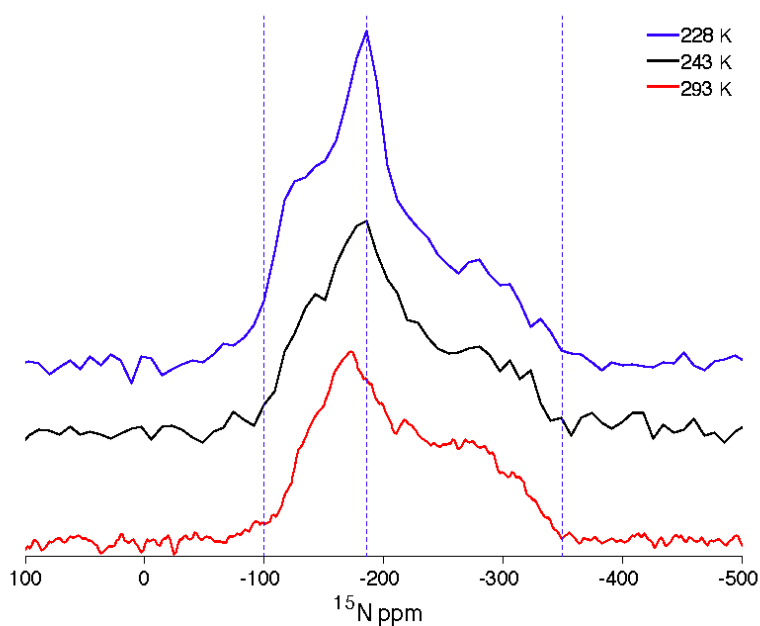
derives from an unprotonated imidazole nitrogen, the intensity is still quite comparable to the peak on the right. This is likely due to the fact that crystalline imidazole is hydrogen-bonded to each other, so protons are in close proximity to all nitrogens, but exchange is slow such that both peaks are present (i.e. in the slow exchange limit).

To see how the powder pattern changes when imidazole is mixed with equimolar HTSFI, Figure B.3b shows the powder pattern for 5:5 [Im][TSFI] at different temperatures. The dotted lines show roughly the three principal axis components. Upon heating, the value of these parameters changes. This indicates that the molecule is experiencing motion that is captured on the NMR timescale. Interestingly, the component around -350 ppm has the least variability, remaining constant in this temperature range. The middle component shows a drastic change, increasing from around -190 ppm to -175 ppm. The final principal component actually decreases slightly, moving upfield. If the motion were truly isotropic, all three values would converge toward the average powder value at a rate dependent on the current distance from that point. Since the component around -350 ppm is unchanging, there is some anisotropy to the motion, meaning some modes of motion are favored.

To investigate this, Figure B.3b shows simulated powder patterns. These were done using the software EXPRESS. Imidazolium was put into the model, and only a ring flip motion was allowed. The rate was adjusted to mimic temperature. The simulated data show that when a ring flip motion is occurring, only two of the three principal values of the CSA tensor are averaged. This hints that in the experimental temperature range, imidazolium ring flips are the dominate motional mode.



(a) Calculated  $^{15}\text{N}$  powder patterns for imidazolium with different flipping rates using EXPRESS allowing only ring flip motion



(b)  $^{15}\text{N}$  powder patterns for 5:5 ionic liquid vs. temperature

Figure B.3: Simulated powder patterns and  $^{15}\text{N}$  NMR data

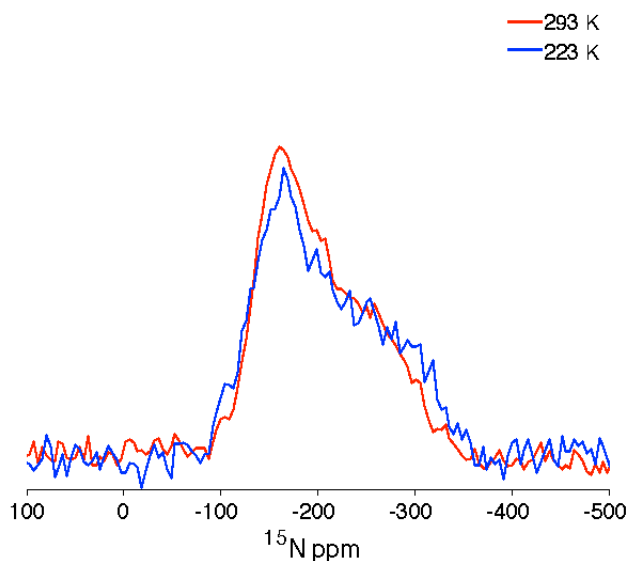


Figure B.4:  $^{15}\text{N}$  powder patterns for 5:5 ionic liquid in P2VP vs. temperature. The weight fraction of polymer is 38%.

The same analysis was performed when mixed with a polymer. Figure B.4 shows the powder patterns for  $^{15}\text{N}$  when mixed with just the homopolymer P2VP. This sample is the same as the one with 38% polymer, the most ionic liquid rich homopolymer sample. In the same temperature range as before, the powder pattern does not seem to be as affected. This indicates that mixing with the polymer either changes the motional modes or at least shifts the temperature response. The  $T_g$  of the polymer with this loading is around 33 °C (306 K); it's likely that significant narrowing would occur when reaching this temperature. In fact, a spectrum at 80 °C shows a single narrow peak (data not shown). One other thing to note is that there seems to be only imidazolium character. There is no evidence of neutral imidazoles. This indicates that the equilibrium favors protonated imidazoles and less transfer to the polymer. A 50/50 mixture of neutral and cationic imidazole would give a powder pattern that was an average of Figure B.1 and Figure B.3b. Figure B.5 shows the powder spectra for various concentrations of ionic liquid all at room temperature. The patterns are all very similar, with the three principal component values appearing to be roughly equal. The samples are all below their glass transition temperature. The data indicate that motion of the imidazole is very slow compared to the NMR timescale below the glass transition even though there is evidence of Arrhenius proton hopping behavior (Chapter 3). Also, despite the base on the polymer, most nitrogens are protonated, as there is no evidence for neutral imidazole in the powder patterns. Higher temperatures are likely needed to promote mixing and alter the equilibrium.

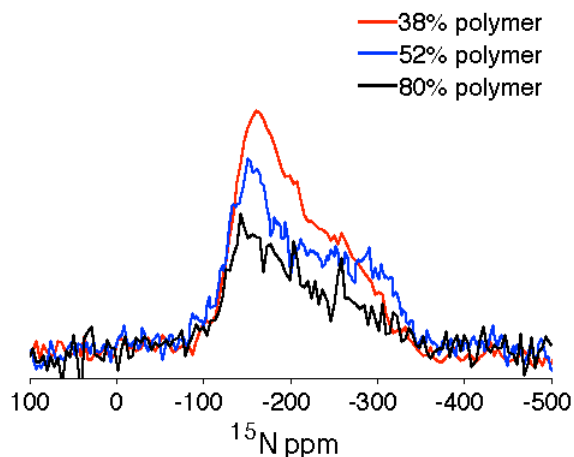
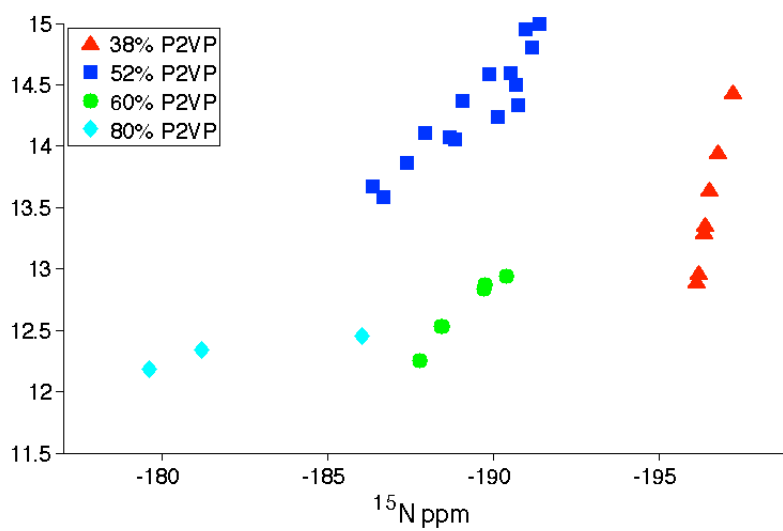


Figure B.5:  $^{15}\text{N}$  powder patterns for 5:5 ionic liquid in P2VP vs. concentration

### B.2.2 $^{15}\text{N}$ MAS NMR

To assess the protonation states of the imidazole, fast spinning MAS NMR was performed as described in Chapter 2. The  $^{15}\text{N}$  spectrum for all samples displayed a single peak, consistent with the hypothesis that imidazole is quickly exchanging protons, which would affect its resonant frequency. Figure B.6 shows the chemical shift data for ionic liquid in the homopolymer. Two general trends are apparent: the chemical shift of nitrogen is much more temperature sensitive with decreasing ionic liquid concentration and chemical shifts are much more upfield with increasing ionic liquid. The interpretation is that in samples with large amounts of ionic liquid, there is more hydrogen bonding with itself and less with the polymer. So electron density is not “given away” to other species (which would shift nitrogens downfield). Small ionic liquid concentrations means that more polymer is present and imidazoles interacting with other imidazoles is less likely. Proton transfer to the polymer would express more neutral imidazole character, and move the shift downfield. The 52% homopolymer sample expressed abnormally high proton shifts, but the slope seems to follow the trend anyway. These results seem consistent with idea of equilibrium between the polymer vinyl pyridine groups and imidazolium.





## Appendix C

# Single $T_2$ Spin Echo Fit: Example Mathematica Code

This appendix demonstrates how to import and fit  $T_2$  data from a spin echo experiment. The data used are from a polymer/ionic liquid sample at 150 °C.

```

(*Load data for both

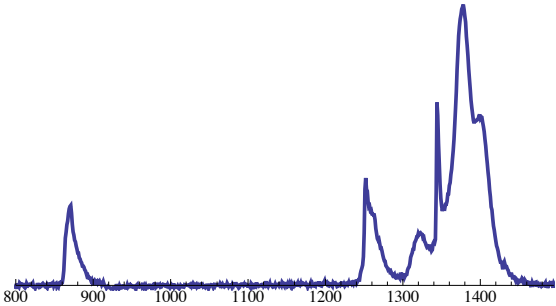
In[14]:= (*Set working directory*)
SetDirectory["/Users/reimer/Documents/Research/Data/Megan/61/T2"];

noofexp = 16; (*Number of variable time experiments performed. If none, put 1.*)
raw = #[[1]] + I #[[2]] & /@ Drop[Import["1H_T2_150C_20kHz.txt", "table"], 0];
part = Partition[raw, Length[raw] / noofexp];

(*other-time data*)

In[17]:= (*The following output should be the number of acquired points/experiment*)
Length[part[[1]]]
Out[17]= 4096

In[8]:= (*This plots the first few points of the FID. Change
the number in "part[[ ]]" to view different ones.*)
ListPlot[Re[part[[1]]], Joined -> True, PlotStyle -> Thick,
PlotRange -> {{800, 1495}, {-25, 2200}}]

Out[8]=


In[37]:= data = Table[Total[Take[Re[part[[i]]], {800, 900}]], {i, 1, noofexp}];
time = {1, 2, 4, 7, 10, 15, 20, 25, 30, 40, 60, 80, 100, 125, 150, 200};

(*time={1,2,4,7,10,15,20,25,30,40,60, 80, 100, 125, 150, 200}; *)

In[39]:= decay1 = Transpose[Join[{time}, {data}]]

Out[39]= {{1, 8861.73}, {2, 9349.89}, {4, 9085.39}, {7, 8322.63}, {10, 8203.14}, {15, 7712.96},
{20, 7355.84}, {25, 7112.38}, {30, 6609.67}, {40, 5725.24}, {60, 4461.8},
{80, 3477.08}, {100, 2419.36}, {125, 1800.94}, {150, 1113.12}, {200, 635.321}}

In[40]:= total = decay1;

(*total=Join[Drop[decay1,0],decay2]*)

```

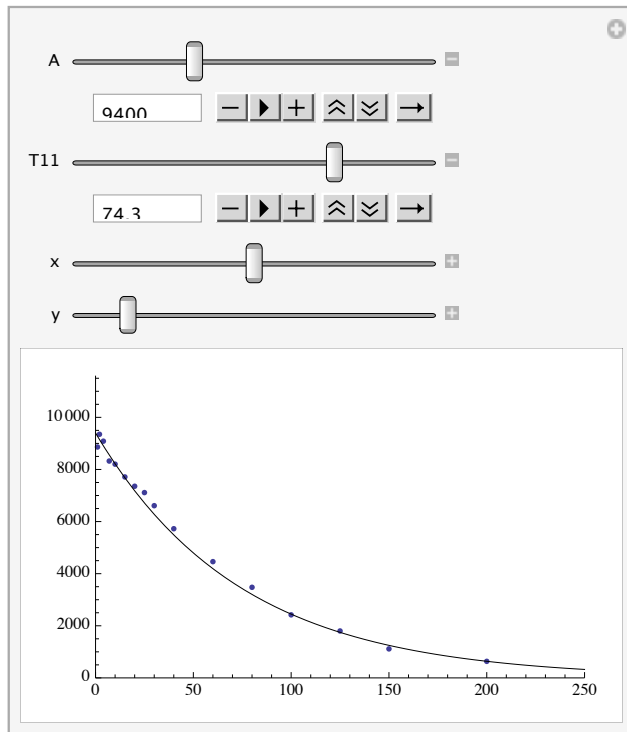
2 | T2\_150C.nb

In[42]=

```

Manipulate[Show[ListPlot[total, PlotRange -> {{0, x}, {0, y}}, Joined -> False],
  Plot[A * (1 (Exp[-t / T11]) (* (1-x1) (Exp[-t/T12]) *)), {t, 0, 250},
  PlotRange -> All, PlotStyle -> {{Thin, Black}}], {{A, 30 000}, .1, 30 000},
  (*{{x1,.284415},0,1},*){{T11, 30}, .01, 100}, (*{{T12,.0400554},.02,.05},*)
  {{x, 250}, .1, 500}, {{y, 3 * 10^4}, 0, 100 000}]

```



Out[42]=

In[44]= Needs["NonlinearRegression`"]

In[45]= (\*Enter your guesses after the variable as shown below. The fit parameters and their confidence intervals are shown as the output. You can input them back into \*)

```
NonlinearRegress[total, A * (1 (Exp[-t / T11]) (+(1-x1) (Exp[-t/T12]))*),
  {{A, 9750}, (*{x1,0.348`},*){T11, 74}}, (*{T12,0.04615`})t]
```

Out[45]= {BestFitParameters → {A → 9394.98, T11 → 78.3241},

| ParameterCITable → |  | Estimate | Asymptotic SE | CI                 |
|--------------------|--|----------|---------------|--------------------|
| A                  |  | 9394.98  | 94.4878       | {9192.33, 9597.64} |
| T11                |  | 78.3241  | 2.265         | {73.4662, 83.182}  |

EstimatedVariance → 42 865.6,

|               | Model             | DF | SumOfSq                   | MeanSq   |
|---------------|-------------------|----|---------------------------|----------|
| ANOVA Table → | Error             | 14 | 600 119.                  | 42 865.6 |
|               | Uncorrected Total | 16 | 6.6844 × 10 <sup>8</sup>  |          |
|               | Corrected Total   | 15 | 1.36601 × 10 <sup>8</sup> |          |

AsymptoticCorrelationMatrix →  $\begin{pmatrix} 1. & -0.604511 \\ -0.604511 & 1. \end{pmatrix}$ ,

| FitCurvatureTable → |                         | Curvature |
|---------------------|-------------------------|-----------|
|                     | Max Intrinsic           | 0.0265492 |
|                     | Max Parameter-Effects   | 0.0767988 |
|                     | 95. % Confidence Region | 0.517164  |

## Appendix D

# Single $T_1$ Inversion Recovery Fit: Example Mathematica Code

This appendix demonstrates how to import and fit  $T_1$  data from an inversion recovery experiment. The data used are from a polymer/ionic liquid sample at 135 °C.

```
In[46]:= (*Load data for both the short- and the long-time data.*)

In[47]:= (*Set working directory*)
SetDirectory["/Users/reimer/Documents/Research/Data/Megan/74/T1/1stSample/1st Run"];

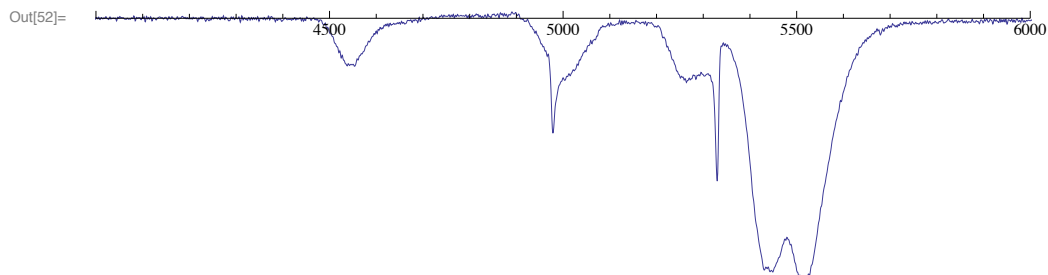
(*long-time data*)
noofexp = 12; (*Number of variable time experiments performed. If none, put 1.*)
raw = #[[1]] + I#[[2]] & /@ Drop[Import["1H_T1_135C_20kHz.txt", "table"], 0];
part = Partition[raw, Length[raw] / noofexp];
```

```
In[51]:= Length[part[[1]]]
```

```
Out[51]= 16384
```

```
In[52]:= (*This plots the first few points of the FID. Change
the number in "part[[ ]]" to view different ones.*)
```

```
ListPlot[Re[part[[1]]], Joined -> True, PlotRange -> {{4000, 6000}, {-900, 900}}]
```

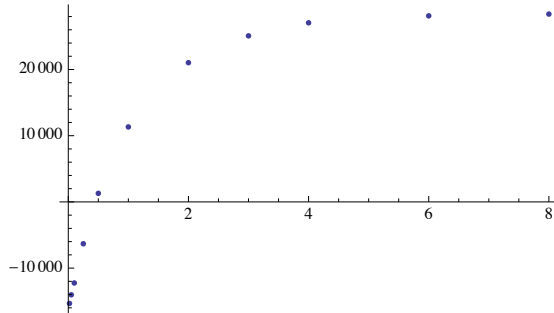


```
In[53]:= data = Table[Total[Take[Re[part[[i]]], {4400, 4700}]], {i, 1, 12}];
time = { .01, .02, .05, .1, .25, .5, 1, 2, 3, 4, 6, 8 };
(*time={.005, .02, .05, .1, .25, .5, 1, 2, 3, 4,6,8}*)
```

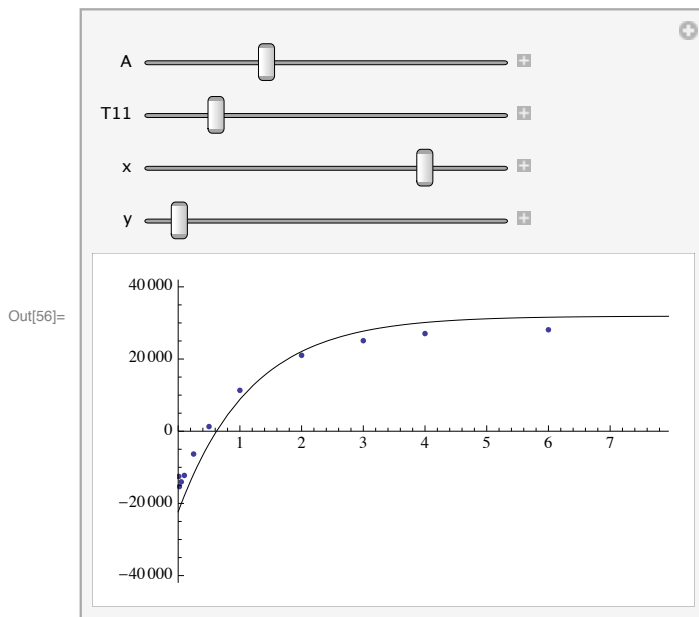
```
In[55]:= tldata = Transpose[Join[{time}, {data}]];
```

2 | T1\_135C.nb

```
(*This plots the T1 data. The two data sets should lie on top
of one another. If not your time tables are probably screwed up.*)
ListPlot[tldata]
```



```
Manipulate[Show[ListPlot[tldata, PlotRange -> {{0, x}, {-y, y}}, Joined -> False],
Plot[A * ((1 - 2 * .85 * (Exp[-t / T11])) ((1-x1) (Exp[-t/T12]) *)), {t, 0, 10},
PlotRange -> All, PlotStyle -> {{Thin, Black}}], {{A, 30000}, .1, 100000},
(*{{x1, .284415}, 0, 1}, *) {{T11, 2}, .01, 7}, (*{{T12, .0400554}, .02, .05}, *)
{{x, 8}, .1, 10}, {{y, 50 * 10^2}, -100000, 1000000}]
```



```
In[57]:= Needs["NonlinearRegression`"]
```

In[58]= (\*Enter your guesses after the variable as shown below. The fit parameters and their confidence intervals are shown as the output. You can input them back into \*)

```
NonlinearRegress[Drop[tldata, {}], A * ((1 - 2 * .85 * (Exp[-t / T11]))),
  {{A, 104000}, {T11, .71}}, t]
```

Out[58]= {BestFitParameters → {A → 25803.9, T11 → 0.849016},

|                      | Estimate | Asymptotic SE | CI                 |
|----------------------|----------|---------------|--------------------|
| ParameterCITable → A | 25803.9  | 890.956       | {23818.8, 27789.1} |
| T11                  | 0.849016 | 0.0723366     | {0.68784, 1.01019} |

EstimatedVariance →  $4.80064 \times 10^6$ ,

|                     | DF | SumOfSq               | MeanSq                |
|---------------------|----|-----------------------|-----------------------|
| Model               | 2  | $4.25986 \times 10^9$ | $2.12993 \times 10^9$ |
| ANOVA Table → Error | 10 | $4.80064 \times 10^7$ | $4.80064 \times 10^6$ |
| Uncorrected Total   | 12 | $4.30787 \times 10^9$ |                       |
| Corrected Total     | 11 | $3.75051 \times 10^9$ |                       |

AsymptoticCorrelationMatrix →  $\begin{pmatrix} 1. & 0.233915 \\ 0.233915 & 1. \end{pmatrix}$ ,

|                                   | Curvature |
|-----------------------------------|-----------|
| FitCurvatureTable → Max Intrinsic | 0.073073  |
| Max Parameter-Effects             | 0.125985  |
| 95. % Confidence Region           | 0.493695  |



## Appendix E

# PFGE Single Self Diffusion Coefficient Fitting: MATLAB code

The appendix features MATLAB code written to determine diffusion coefficients from pulsed field gradient NMR experiments. The code was largely written by Jay Yostanto.

## PFG Data

The following commands were written in MatLab to import and analyze data for the Pulse Field Gradient NMR experiment for the determination of self diffusion coefficients of solvent in Nafion type membranes. Spectra from tNMR were exported as text files and placed inside the appropriate MatLab folder with the corresponding 'MasterCodePGSE.m' file that can be quickly edited for data fitting and plot production.

```
%This script has the following functions:
%   Auto-rephasing to find phase with max integral for each scan
%   2D and 3D plots of scans
%   Integration Plots with fitted line to find diffusion coefficients
```

First, the code clears all pre-existing data and figures in the workspace to ensure a new working environment. Timing of the script begins with 'tic.'

```
clear all
close all
clc
tic
```

'Control Center' has been implemented to create a condensed space where editing input variables can be done quickly and efficiently. Explanations of variable names have been commented.

```
%-----
%Control Center: Change variables here
%CONDITIONS OF THROWOUT: points need to be between startfit and stopfit
%and number of points used needs to be greater than or equal to the
%difference between the last point used and stopfit
Name = 'PGSE 50C nafion';      %Name of file ***without .txt***
Left = 2;                      %left endpoint of fit
Right = 1023;                  %right endpoint of fit
startfit = 2;                  %first point to fit against
stopfit = 30;                  %last point to fit against
Points = 1024;                 %Number of points in each scan
Atten = 32;                    %Number of scans in experiment
absval = 'yes';                %Graph and fit to absolute values of all points
TwoDPlot = 'on';               %Toggle for 2D Plot
ThreeDPlot = 'on';             %Toggle for 3D Plot

%Outliers to be thrown out in fitting
throwout = [];
```

Exported data is read through the following commands when implemented after the Control Center is defined.

```
%-----
%This code helps read exported data
b = '.txt';
ab = strcat(Name,b);
str1 = sprintf(ab);
str2 = sprintf(Name);
%Assigns 3 columns of exported data to variables to below
[Real, Imag, Hz] = textread(str1,'%f %f %f', Points*Atten);
```

The data is partitioned into individual scans so that they may be analyzed as if they came straight out of tNMR.

```

%-----
%This Code Rephases the Data, maximizing the integral of the real

%Partitions Imaginary data
for i = 1:Atten;
    A(:,i) = Imag(1+(i-1)*Points:i*Points);
end

%Partitions Real data
for i = 1:Atten;
    C(:,i) = Real(1+(i-1)*Points:i*Points);
end

```

The data is then evaluated at every phase degree within a spacing tolerance and the scan at the phase degree with the largest value of integration is chosen to be saved as the scan to be used for plotting and fitting. The ‘re-phasing’ of the individual scans follows the equation:  $R' = R\cos\theta + i\sin\theta$  where  $R'$  is the rephased real value,  $R$  is the originally exported real value, and  $i$  is the originally exported imaginary value. It can be observed that when  $\theta$  is zero there is no change in the real value.

```

%Rephases all scans to spacing
phase = linspace(0,2*pi,250); %Sets spacing for rephasing
for i = 1:Atten;
    for k = 1:250;
        for j = 1:Points;
            B(j,i) = C(j,i)*cos(phase(k)) + A(j,i)*sin(phase(k));
        end
        value(k,i) = sum(B(:,i)); %Finds integrals of all rephased scans
    end
end

%Finds rephased scan with highest value integral
for i = 1:Atten;
    index(i) = find(value(:,i)==max(value(:,i)));
end

%Partitions the max integral rephased scan
for i = 1:Atten;
    for j = 1:Points;
        E(j,i) = C(j,i)*cos(phase(index(i)))+ A(j,i)*sin(phase(index(i)));
    end
end

```

Scans can be evaluated at the absolute value of their data if desired through the following commands. This option is changed in the Control Center.

```

%Code for whether graph of absolute or nonabsolute values is desired
if strcmp(absval,'yes') %Code for absolute values only
    for i = 1:Atten
        Real(1+(i-1)*Points:i*Points)=abs(E(1:Points,i));
    end
elseif strcmp(absval,'no') %Code for all values
    for i = 1:Atten
        Real(1+(i-1)*Points:i*Points)=E(1:Points,i);
    end
end
end

```

Noise is subtracted from individual scans by averaging the last 50 points of each scan (presumably all noise data) and subtracting that average from every point in the scan.

```

%Subtracts noise
Noise = sum(Real((Points*Atten-50):Points*Atten))/50;
Real = Real - Noise;

```

If selected in the Control Center, a 2D plot may be generated with all individual scans in a set of data superimposed in one plot. The y axis is defined by the data points (attenuation signal) while the x axis is the Hertz value of the corresponding data value. Code for plot labeling has been implemented.

```

%-----
%This code plots a 2D graph of all scans superimposed
if strcmp(TwoDPlot,'on') %Toggle for 2D plot
    figure(1);
    for j=1:Atten
        y = Real((j-1)*Points+1:(j*Points));
        x = Hz((j-1)*Points+1:(j*Points));
        plot(x,y);
        hold all;
    end

    %Plot labels and limitations
    % xlim([-0.12*10^4 0.2*10^4]);
    xlabel('Hertz','FontSize',13,'FontName','Baskerville');
    ylabel('Intensity','FontSize',13,'FontName','Baskerville');
    title(str2,'FontSize',20,'FontName','Baskerville');
end

```

If selected in the Control Center, a 3D plot may be generated with all individual scans in a set of data superimposed in one plot. The y axis is defined by the data points (attenuation signal), the x axis is the Hertz value of the corresponding data value. Code for plot labeling has been implemented, and the z axis is the corresponding order of individual scans taken over the experiment set.

```

%-----
% This code plots a 3D graph of all scans
if strcmp(ThreeDPlot,'on') %Toggle for 3D plot
    figure(2);
    for j=1:Atten
        y = Real((j-1)*Points+1:(j*Points));
        x = Hz((j-1)*Points+1:(j*Points));
        for i=1:Points
            z(i) = j;
        end
        plot3(z,x,y);
        hold on;
    end

    %Plot labels and limitations
    ylim([-0.2*10^4 0.2*10^4]);
    xlabel('Attenuation Number','FontSize', 13, 'FontName', 'Baskerville');
    ylabel('Hertz','FontSize', 13, 'FontName', 'Baskerville');
    zlabel('Intensity','FontSize',13, 'FontName', 'Baskerville');
    title(str2,'FontSize',20, 'FontName', 'Baskerville');
end

```

Plotting the attenuated signal with respect to scaled gradient strength reflected by the Stejskal-Tanner:  $\ln \frac{I(g)}{I(0)} = (\gamma g \delta)^2 D (\Delta - \frac{\delta}{3})$  yields the diffusion coefficient  $D$  of the species, where  $I(g)$  is the integration of a scan at that  $g$  value,  $I(0)$  is the integration of the first scan where no gradient is applied,  $\gamma$  is the gyromagnetic ratio ( $267.5 * 10^6$  for  $^1\text{H}$ ),  $g$  is the gradient strength scaled by a factor determined by calibration,  $\delta$  is the length of the gradient pulse, and  $\Delta$  is the time between gradient pulses.

Variables in the Control Center called ‘Left’ and ‘Right’ can set the “window” in which the integral of each individual scan is taken for data fitting. The integration of each scan is normalized to the first scan and then the log of each scan is taken to fit the Stejskal-Tanner equation for fitting.

```

%-----
%This code plots the semilog of normalized integration of each scan versus
%constants as described by the equation:
%           ln(I(g)/I(0)) = D*(\gamma*g*\delta)^2(\Delta-\delta/3)
%to find D, the diffusion coefficient.
clear A

%Partitions Real according to Left and Right for specific integration
for i=1:Atten
    A(:,i) = Real((i-1)*Points+1+Left:Points*(i-1)+1+Right);
end

%Code to find semilog of normalized integration of each scan
y_0 = sum(A(:,1)); %Normalize to the first scan
for i=1:Atten
    Data(i) = log(sum(A(:,i))/y_0);
end
Data = Data'; %Invert for matrix linear polyfit

```

Constants mentioned above that define the Stejskal-Tanner equation are included in the code. The values of  $g$  are set on the experimental hardware and the gradient factor is determined through a water calibration with a known  $D$  value from the literature.

```
%Constants
g = [0
2.1
4.2
5.47
7.74
8.75
10.2
11.5
12.24
12.85
13.41
14.0
14.49
15.49
16
16.43
16.9
17.32
18.16
18.5
18.97
19.5
19.74
20.49
21.21
21.5
21.90
22.58
22.9
23.23
23.87
24.494
];
g=g';
gamma = 267.513*10^6;
delta = 1*10^-3;
Delta = 9.125*10^-3;
gradient=g.*.079;
x = (gamma^2)*(gradient.^2)*(delta^2)*(Delta-delta/3);
```

Data points adjusted from the code above are plotted against the constants in the Stejskal-Tanner equation to produce a semi-log plot. A variable in the Control Center called 'Throwout' can be used to eliminate outliers in data. Data fit in later code is shown in a different color.

```

figure(3);
%Plot integration of all scans
plot(x,Data,'o')
hold all

%Eliminate outliers with throwout
[m,n] = size(throwout);
for i = 1:n
    Data(throwout(i))=[];
    x(throwout(i))=[]; %Adjust x axis
end

%Show all points fitted against
stopfit = stopfit - n; %Adjust points to eliminated outliers
plot(x(startfit:stopfit),Data(startfit:stopfit),'o')
hold all

```

Code was written to determine the slope  $D$  of the data set by a polyfit function constructed using matrices and linear algebra. Variables in the Control Center called 'startfit' and 'stopfit' were used to enable the user to fit against a shorter portion of the scans when desired.

```

%Code to fit a line against specific interval of points with throwouts
X(1:(stopfit-startfit+1),1) = 1;
X(:,2) = x(startfit:stopfit);
DataFit = Data(startfit:stopfit);
a = ((X'*X)^-1)*X'*DataFit;
y = a(2)*x+a(1);
plot(x,y,'x') %Plot fitted line to interval of start/stopfit - throwout

```

Finally, the integration plot is labeled and  $D$  is displayed on the graph with the following code. 'toc' is used to stop the timing of the code and will display the time taken to run the entire script.

```

%Plot labels and limitations; display functions
D = num2str(abs(a(2)));
display(D)
r = 'D = ';
BigD = [r D];
xlabel('x = (\gamma*g*\delta)^2(\Delta-\delta/3)', 'FontSize', ...
    13, 'FontName', 'Baskerville');
ylabel('y = ln(I(g)/I(0))', 'FontSize', 13, 'FontName', 'Baskerville');
title(str2, 'FontSize', 20, 'FontName', 'Baskerville');
legend('Data unused', 'Data fit', 'y = D*x');
annotation('textbox', [.30 .79 .1 .1], ...
    'String', BigD, 'FontSize', 13);

toc
%-----

```

## Appendix F

# $T_{1\rho}$ Relaxation Data Fitting: Mathematica Code

This appendix features Mathematica code used to fit spin-lattice relaxation in the rotating frame data. This example is regular Nafion 212 at room temperature.



```

(*Load data*)

In[17]:= (*Set working directory*)
SetDirectory[
  "/Users/reimer/Documents/Research/Data/Kerr/N212/Fluorine/N212/400/N212 Control/";

(*long-time data*)
noofexp = 14; (*Number of variable time experiments performed. If none, put 1.*)
raw = #[[1]] + I #[[2]] & /@ Drop[Import["State 8.txt", "table"], 0];
part = Partition[raw, Length[raw] / noofexp];

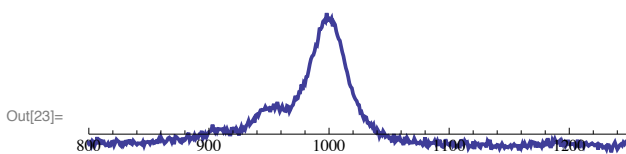
(*other-time data*)

In[21]:= (*The following output should be the number of acquired points/experiment*)
Length[part[[1]]]

Out[21]= 2048

In[23]:= (*This plots the first few points of the FID. Change
the number in "part[[ ]]" to view different ones.*)
ListPlot[Re[part[[1]]], Joined -> True, PlotStyle -> Thick,
PlotRange -> {{800, 1248}, {-8000, 10000}}]

```



```

In[24]:= data = Table[Total[Take[Re[part[[i]]], {990, 1020}]], {i, 1, noofexp}];
time = { .5, 1, 1.5, 2, 3, 4, 5, 6, 8, 10, 12.5, 15, 17.5, 20};

In[26]:= decay1 = Transpose[Join[{time}, {data}]]

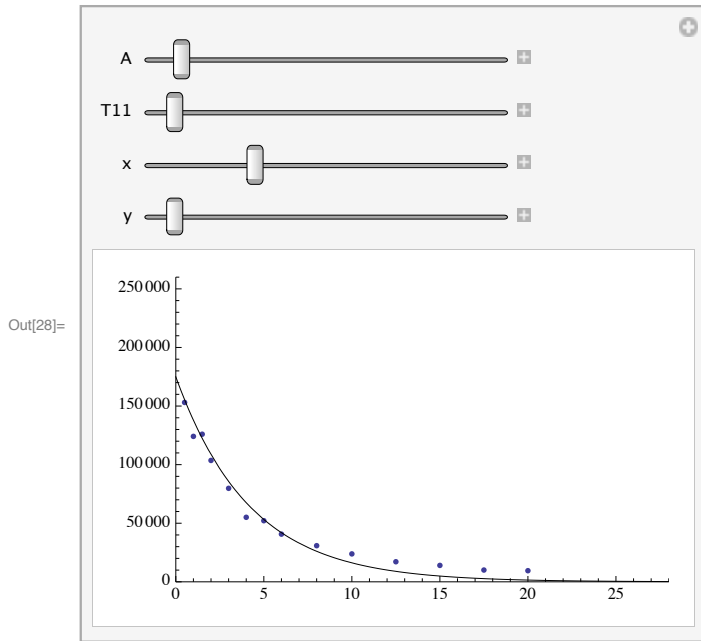
Out[26]= {{0.5, 153.077.}, {1, 124.123.}, {1.5, 125.975.}, {2, 103.585.},
{3, 79.784.}, {4, 55.065.3}, {5, 52.153.7}, {6, 40.689.1}, {8, 30.838.6},
{10, 23.831.2}, {12.5, 17.127.9}, {15, 14.013.2}, {17.5, 10.053.8}, {20, 9.493.71}}

In[27]:= total = decay1;

(*total=Join[Drop[decay1,0],decay2]*)

```

```
Manipulate[Show[ListPlot[total, PlotRange -> {{0, x}, {0, y}}, Joined -> False],
  Plot[A * (1 (Exp[-t / T11]) (*+(1-x1) (Exp[-t/T12])*)), {t, 0, 250},
  PlotRange -> All, PlotStyle -> {{Thin, Black}}], {{A, 500 000}, .1, 3 000 000},
  (*{{x1,.284415},0,1},* ){{T11, 30}, .01, 100}, (*{{T12,.0400554},.02,.05},* )
  {{x, 40}, .1, 100}, {{y, 3 * 10^6}, -100 000, 10 000 000}]
```



```
In[31]= Needs["NonlinearRegression`"]
```

```
In[32]= (*Enter your guesses after the variable as shown below. The fit parameters and their
confidence intervals are shown as the output. You can input them back into *)
NonlinearRegress[total, A * (1 (Exp[-t / T11]) (*+(1-x1) (Exp[-t/T12]))*),
{{A, 770050}, (*{x1,0.348`},*){T11, 17}}, (*{T12,0.04615`})*t]
```

```
Out[32]= {BestFitParameters → {A → 164 162., T11 → 4.45472},
ParameterCITable → 

|     | Estimate | Asymptotic SE | CI                   |
|-----|----------|---------------|----------------------|
| A   | 164 162. | 6159.23       | {150 742., 177 582.} |
| T11 | 4.45472  | 0.307418      | {3.78492, 5.12453}   |


EstimatedVariance →  $5.0788 \times 10^7$ ,
ANOVA Table → 

|                   | DF | SumOfSq                  | MeanSq                   |
|-------------------|----|--------------------------|--------------------------|
| Model             | 2  | $8.08025 \times 10^{10}$ | $4.04012 \times 10^{10}$ |
| Error             | 12 | $6.09457 \times 10^8$    | $5.0788 \times 10^7$     |
| Uncorrected Total | 14 | $8.1412 \times 10^{10}$  |                          |
| Corrected Total   | 13 | $3.10346 \times 10^{10}$ |                          |


AsymptoticCorrelationMatrix →  $\begin{pmatrix} 1. & -0.74397 \\ -0.74397 & 1. \end{pmatrix}$ ,
FitCurvatureTable → 

|                         | Curvature |
|-------------------------|-----------|
| Max Intrinsic           | 0.0821575 |
| Max Parameter-Effects   | 0.260897  |
| 95. % Confidence Region | 0.507327  |


```